PNAS
www.pnas.org

Supplementary Information for

Regulation of nuclear architecture, mechanics and nucleo-cytoplasmic shuttling of epigenetic factors by cell geometric constraints

Farid Alisafaei [1,2], Doorgesh Sharma Jokhun [3], G. V. Shivashankar [3,4], Vivek B. Shenoy [1,2,*]

[1] Department of Materials Science and Engineering, School of Engineering and Applied Science, University of Pennsylvania, Philadelphia, PA 19104

[2] Center for Engineering Mechanobiology, University of Pennsylvania, Philadelphia, PA, USA

[3] Mechanobiology Institute and Department of Biological Sciences, National University of Singapore 117411, Singapore

[4] FIRC Institute for Molecular Oncology (IFOM), Milan 20139, Italy

[*] To whom correspondence should be addressed. email: vshenoy@seas.upenn.edu

This PDF file includes:

Supplementary text

References for SI reference citations

Figures: Supplementary Figure 1 to Supplementary Figure 36

Tables: Supplementary Table 1 to Supplementary Table 2

Captions for movies S1 to S4

Other supplementary materials for this manuscript include the following:

Movies S1 to S4

www.pnas.org/cgi/doi/10.1073/pnas.1902035116

Supplementary Text

1. One-dimensional cell model

We here present a one-dimensional cell model that represents the key features of our three-dimensional model in Section 2.

1.1. Cytoskeleton

Similar to the three-dimensional cytoskeletal model, the one-dimensional cytoskeletal model (Figure S7A) is composed of three elements including (i) the myosin molecular motors (shown by the active contractile element in red), (ii) the microtubules (shown by the passive element in black), and (iii) the actin filaments (shown by the passive element in green).

Phosphorylated myosin molecular motors generate internal stresses which are denoted by ρ (cell contractility) in our one-dimensional model. As experimentally observed[1], microtubules are compressively loaded by the cell generated internal stress ρ, while the rest of this internal stress, σ, is transmitted to the extracellular matrix through the actin filament network. Microtubules in Figure S7A are represented by a passive element with an elastic modulus $E^{(\mathrm{MT})}$ connected in parallel to the active contractile element. As reported by various experimental studies[2,3], cells respond to the stiffness of their microenvironment by increasing their cytoskeletal stiffness. This increase in the cytoskeletal stiffness and subsequently cell stiffness has been observed to be correlated with recruitment and alignment of actin filaments along the direction of the tensile stress σ. To capture the cell stiffening, we add a passive element in series to the other two parallel elements to represent actin filaments in our model. The elastic modulus of this element, $E^{(\mathrm{A})}$, increases with tension (but not in compression) to capture the tension induced cell stiffening observed in various experiments

$$E^{(\mathrm{A})} = E^{(\mathrm{I})} + E^{(\mathrm{F})} = E^{(\mathrm{I})} + \ell(\varepsilon^{(\mathrm{Y})})^{m} \tag{S1.1}$$

where $E^{(\mathrm{I})}$ is the initial elastic modulus of the actin network (e.g., the elastic modulus of the actin network when the stiffness of the cell substrate is negligible $\rightarrow E^{(\mathrm{A})} = E^{(\mathrm{I})}$), and $E^{(\mathrm{F})}$ denotes the tension induced stiffening of the actin network. As shown in equation (S1.1), $E^{(\mathrm{F})}$ increases with

the tensile strain $\varepsilon^{(\mathrm{Y})}$ where ℓ and m are the stiffening parameters used in our cytoskeletal model. The cell contractility ρ in our one-dimensional cytoskeletal model is defined as[4]

$$\rho = \frac{E^{(\mathrm{MT})}\,\alpha - 1}{\beta - \alpha}\varepsilon^{(\mathrm{X})} + \frac{\beta}{\beta - \alpha}\rho_0 \tag{S1.2}$$

where α is the chemo-mechanical feedback parameter, β is the chemical stiffness parameter, $\varepsilon^{(\mathrm{X})}$ is the strain of the two parallel elements as shown in Figure S7A, and ρ_0 is the initial contractility of the cell. The effects of α and β on the cell response to the stiffness of its microenvironment is schematically shown in Figure S7B. As described in SI Section 1.2, a large value of α strengthens the stress-dependent feedback mechanism of the cell as the cell promotes myosin motor binding in response to the stiffness of its surrounding. Subsequently, this increase in the overall density of phosphorylated myosin molecular motors increases the cell contractility ρ, the cell generated active stress σ, the cytoskeletal stiffness E, and the cell contraction $|\varepsilon|$. Unlike α, a large value of β weakens the stress-dependent feedback mechanism of the cell as it makes myosin motor recruitment more difficult. Therefore, an increase in β causes the cell contractility, active stress, cytoskeletal stiffness, and cell contraction to decrease (see SI Section 1.2 and Figure S20 for more details).

Denoting the stress in the microtubule network as $E^{(\mathrm{MT})}\varepsilon^{(\mathrm{X})}$ and using σ to denote the stress transmitted to the extracellular matrix through the actin filament network, we have

$$\rho = -E^{(\mathrm{MT})}\varepsilon^{(\mathrm{X})} + \sigma \tag{S1.3}$$

Substituting equation (S1.2) into (S1.3), we can derive the tensile stress σ generated by the cell

$$\sigma = \frac{E^{(\mathrm{MT})}\,\beta - 1}{\beta - \alpha}\varepsilon^{(\mathrm{X})} + \frac{\beta}{\beta - \alpha}\rho_0 \tag{S1.4}$$

which is transmitted to the extracellular matrix through the actin filament network

$$\sigma = \int E^{(\mathrm{A})}\,\mathrm{d}\varepsilon^{(\mathrm{Y})} = \int \left(E^{(\mathrm{I})} + \ell\left(\varepsilon^{(\mathrm{Y})}\right)^{m}\right)\mathrm{d}\varepsilon^{(\mathrm{Y})} = E^{(\mathrm{I})}\varepsilon^{(\mathrm{Y})} + \frac{\ell}{m+1}\left(\varepsilon^{(\mathrm{Y})}\right)^{m+1} \tag{S1.5}$$

As the actin filament network is connected to the other two elements (the myosin motors and the microtubules) in series, the total elastic modulus of the cytoskeleton, E, in our one-dimensional model can be obtained as follows

$$\frac{1}{E} = \frac{1}{E^{(\mathrm{X})}} + \frac{1}{E^{(\mathrm{Y})}} \tag{S1.6}$$

where

$$E^{(\mathrm{X})} = \frac{E^{(\mathrm{MT})}\,\alpha - 1}{\beta - \alpha} + E^{(\mathrm{MT})} = \frac{E^{(\mathrm{MT})}\,\beta - 1}{\beta - \alpha} \quad , \quad E^{(\mathrm{Y})} = E^{(\mathrm{A})} \tag{S1.7}$$

As shown in Figure S20, the elastic modulus of the actin filament network, $E^{(\mathrm{A})}$, and subsequently the total elastic modulus of the cytoskeleton, E, increase with matrix elastic modulus.

1.2. Cell force generation, cell contractility, and cytoskeletal stiffness increase with matrix stiffness

To illustrate the ability of our chemo-mechanical cell model to capture the response of cells to the stiffness of their environment, we here present a simple one-dimensional example that represents the key features of the three-dimensional cell model in SI Section 2. In this example, a contractile cell is attached to two microposts as shown in Figure S20A. The microposts are represented in this example as linear elastic springs with an elastic modulus $\tilde{E}$. Note that unlike our three-dimensional matrix model (see SI Section 2), the microposts are assumed to be linear in this example for simplicity (i.e., the micropost elastic modulus $\tilde{E}$ is not a function of the micropost strain $\tilde{\varepsilon}$). The strain at each micropost, $\tilde{\varepsilon}$, induced by the cell generated stress σ

$$\sigma = \tilde{E}\tilde{\varepsilon} \tag{S1.8}$$

can be written as

$$2\tilde{\varepsilon} + \varepsilon = 2\tilde{\varepsilon} + \varepsilon^{(\mathrm{X})} + \varepsilon^{(\mathrm{Y})} = 0 \tag{S1.9}$$

which indicates that the total strain between the posts is zero. Solving equations (S1.4), (S1.5), (S1.8), and (S1.9) together, we can determine σ, $\varepsilon^{(\mathrm{X})}$, $\varepsilon^{(\mathrm{Y})}$, and $\tilde{\varepsilon}$ (4 equations, 4 unknowns). Then, the cell contractility ρ and the total elastic modulus of the cytoskeleton, E, can be obtained from (S1.3) and (S1.4), respectively.

We plot the cell generated active stress, cell contractility, cytoskeletal stiffness, and cell contractile strain as functions of the elastic modulus of the microposts in Figure S20 to illustrate the key predictions of the 1D model. All constants used in Figure S20 are given in Supplementary Table 1. As shown in Figure S20B, the cell generated stress σ increases with micropost stiffness. The cell actively responds to this increase in the tensile stress σ by increasing the density of phosphorylated myosin motors which leads to an increase in the cell contractility ρ with increasing micropost stiffness (Figure S20C). Furthermore, the cell responds to the increased tension by recruitment of actin filaments and subsequently increasing its own stiffness (Figure S20D).

The effects of the chemo-mechanical feedback parameter α and the chemical stiffness parameter β on the response of the cell to the stiffness of its surrounding are shown in Figure S20 (B-E) as we increase α and β by 50 percent. A large value of the chemo-mechanical feedback parameter α strengthens the stress-dependent feedback mechanism in our model as the cell promotes myosin phosphorylation in response to the stiffness of its matrix. This increase in the overall density of phosphorylated myosin motors subsequently increases the cell generated active stress σ, the cell contractility ρ, the cytoskeletal stiffness E, and the cell contractile strain $|\varepsilon|$. Unlike α, a large value of the chemical stiffness parameter β weakens the stress-dependent feedback mechanism of the cell as it makes motor recruitment more difficult. Therefore, an increase in β causes the active stress, cell contractility, cytoskeletal stiffness, and cell contractile strain to decrease.

1.3. nucleus:

The nucleus in our one-dimensional model is composed of chromatin and lamin which are connected in parallel as shown in Figure S17A. Therefore, the total stiffness of the nucleus is $\bar{E} + \hat{E}$ where $\bar{E}$ and $\hat{E}$ are the elastic moduli of chromatin and lamin, respectively. Uniaxial stretching of single isolated nuclei in Figure S35 shows that chromatin exhibits linear behavior even at large extensions. Therefore, the elastic modulus of chromatin, $\bar{E}$, is assumed to be strain independent. The nuclear envelope lamina network is a filamentous material[5] which shows strain stiffening in the uniaxial stretch tests[6] (Figure S35). Therefore, we assume that the elastic modulus of the lamin network increases with the tensile strain in the nucleus, $\hat{\varepsilon}$, as follows

$$\hat{E} = \hat{E}^{(\mathrm{I})} + \hat{E}^{(\mathrm{F})} = \hat{E}^{(\mathrm{I})} + \hat{\ell}(\hat{\varepsilon})^{\hat{m}} \tag{S1.10}$$

where $\hat{E}^{(\mathrm{I})}$ is the initial elastic modulus of the lamin network (e.g., the elastic modulus of the lamin network when the nucleus is not under tension $\rightarrow \hat{E} = \hat{E}^{(\mathrm{I})}$), and $\hat{E}^{(\mathrm{F})}$ denotes the tension induced stiffening of the lamin network. Equation (S1.10) shows that $\hat{E}^{(\mathrm{F})}$ increases with the tensile strain $\hat{\varepsilon}$ where $\hat{\ell}$ and $\hat{m}$ are the stiffening parameters. The tensile stress σ generated by the actomyosin system is transmitted to the nucleus

$$\sigma = \bar{\sigma} + \hat{\sigma} = \bar{E}\hat{\varepsilon} + \int \hat{E}\,\mathrm{d}\hat{\varepsilon} = \bar{E}\hat{\varepsilon} + \hat{E}^{(\mathrm{I})}\hat{\varepsilon} + \frac{\hat{\ell}}{\hat{m}+1}(\hat{\varepsilon})^{\hat{m}+1} \tag{S1.11}$$

where $\bar{\sigma}$ and $\hat{\sigma}$ are the stresses that are transmitted to chromatin and lamin, respectively. The unknowns σ, $\varepsilon^{(\mathrm{X})}$, $\varepsilon^{(\mathrm{Y})}$, $\tilde{\varepsilon}$, and $\hat{\varepsilon}$ can be determined from the set of equations (S1.4), (S1.5), (S1.8), (S1.9) and (S1.11).

1.4. Lamin A,C level increases with matrix stiffness

First, we study how lamin A,C changes with matrix stiffness. Figure S17A shows a contractile cell attached to two linear microposts. All constants used in Figure S17 are given in Supplementary Table 2. As shown in Figure S17(C-E) and discussed in the previous section, actomyosin contractility increases with micropost stiffness which in turn generates higher tension in the nuclear envelope lamina network. Subsequently, lamin A,C level increases[7] which leads to nuclear stiffening as shown in Figure S17F.

1.5. Cytoskeletal tension, cell contractility, cytoskeletal stiffness and lamin A,C level increase with depolymerization of microtubules:

As shown in Figures S17 (A and B), Microtubules in our active model experience compressive stresses due to the cell contractility ρ. Consistent with experimental observations[8], Figures S17 (C-E) show that actomyosin contractility increases with depolymerization of microtubules. This leads to higher tension in the nuclear envelope and stiffening of the lamin network as shown in Figure S17F.

1.6. Cytoskeletal tension, cell contractility, and cytoskeletal stiffness decrease with lamin A,C knockdown:

Figures S17 (C and D) show that tension in the cytoskeleton and cell contractility decrease with lamin A,C knockdown, respectively. This is consistent with recent experimental studies[9] which show that myosin-II contractility in mesenchymal stem cells decreases with partial knockdown of

lamin A,C. Concomitant with the decrease in cell contractility, cytoskeletal stiffness decreases with lamin A,C knockdown (Figure S17E). This is in agreement with experimental reports which show that lamin A,C deficient mouse embryonic fibroblasts lack apical stress fibers[10].

2. Three-dimensional cytoskeletal model

We here generalize our one-dimensional cytoskeletal model (presented in SI Section 1) to a three-dimensional constitutive model to be implemented into a three-dimensional finite element framework. As shown in Figure S7A, the cytoskeletal model is composed of three elements including (i) the myosin molecular motors, (ii) the microtubules, and (iii) the actin filaments.

2.1. Myosin molecular motors:

As schematically shown in Figure 7A in the main text, myosin II motors bind to actin filaments and exert contractile forces. The contractile force exerted by an individual myosin motor can be modeled as a force dipole (force couple) which is a pair of equal but oppositely directed forces $F_i(x_j)$ and $-F_i(x_j + \Delta x_j)$ that act on the actin filament network. Note that x_j and $x_j + \Delta x_j$ are coordinates of myosin head domains, $\left|F_i^{(k)}\right|$ is the magnitude of the force dipole (approximately 1 pN[11]), and $|\Delta x_j|$ is the length of myosin II filaments (approximately 200 nm[12]). The mechanical work generated by the force dipole is then calculated as follows

$$W_{\text{dipole}} = F_i u_i(x_j + \Delta x_j) - F_i u_i(x_j) \tag{S2.1}$$

where $u_i(x_j)$ and $u_i(x_j + \Delta x_j)$ are the cytoskeletal displacements at the myosin head domains x_j and $x_j + \Delta x_j$, respectively. The total work done by all phosphorylated myosin motors per volume V is

$$W = \left(\frac{1}{V}\right)\sum_{k=1}^{N}\left[F_i^{(k)} u_i\left(x_j^{(k)} + \Delta x_j^{(k)}\right) - F_i^{(k)} u_i\left(x_j^{(k)}\right)\right] \tag{S2.2}$$

where N is the number of bound motors. Using the following definition

$$\partial_j u_i = \frac{u_i\left(x_j^{(k)} + \Delta x_j^{(k)}\right) - u_i\left(x_j^{(k)}\right)}{\Delta x_j^{(k)}} \tag{S2.3}$$

equation (S2.2) can be rewritten as follows

$$W = \left(\frac{1}{V}\right)\sum_{k=1}^{N} F_i^{(k)}\,\Delta x_j^{(k)}\partial_j u_i \tag{S2.4}$$

Then, using the definition of strain

$$\varepsilon_{ij} = \frac{1}{2}\left(\partial_j u_i + \partial_i u_j\right) \tag{S2.5}$$

we can rewrite equation (S2.4) in the following form

$$W = \rho_{ij}\varepsilon_{ij} \tag{S2.6}$$

if we assume that the contractility tensor ρ_{ij}

$$\rho_{ij} = \left(\frac{1}{V}\right)\sum_{k=1}^{N} F_i^{(k)}\,\Delta x_j^{(k)} \tag{S2.7}$$

is symmetric, i.e.,

$$F_i^{(k)}\Delta x_j^{(k)} = F_j^{(k)}\Delta x_i^{(k)} \tag{S2.8}$$

Equation (S2.7) shows that the contractility tensor ρ_{ij} is related to the average density of the phosphorylated myosin motors per unit volume. We therefore use ρ_{ij} in our coarse-grained model to represent cell contractility in different directions and we define it in a way that enables us to capture the fact that cell contractility increases with tension. To this end, similar to our one-dimensional model in equation (S1.2), we define the cell contractility tensor ρ_{ij} in our three-dimensional model as follows[4]

$$\rho_{ij} = K^{(\rho)}\varepsilon_{kk}^{(\mathrm{X})}\delta_{ij} + 2\mu^{(\rho)}\left(\varepsilon_{ij}^{(\mathrm{X})} - \frac{1}{3}\varepsilon_{kk}^{(\mathrm{X})}\delta_{ij}\right) + \bar{\rho}_0\delta_{ij} \tag{S2.9}$$

where $K^{(\rho)}$ is the motor density effective modulus

$$K^{(\rho)} = \frac{3K^{(\mathrm{MT})}\alpha_{\mathrm{v}} - 1}{3(\beta_{\mathrm{v}} - \alpha_{\mathrm{v}})} \tag{S2.10}$$

$\mu^{(\rho)}$ is the polarization effective modulus

$$\mu^{(\rho)} = \frac{2\mu^{(\mathrm{MT})}\alpha_{\mathrm{d}} - 1}{2(\beta_{\mathrm{d}} - \alpha_{\mathrm{d}})} \tag{S2.11}$$

$\bar{\rho}_0$ is the effective contractility

$$\bar{\rho}_0 = \frac{\beta_{\mathrm{v}}\,\rho_0}{\beta_{\mathrm{v}} - \alpha_{\mathrm{v}}} \tag{S2.12}$$

and the strain tensor $\boldsymbol{\varepsilon}^{(\mathrm{X})}$ is the three-dimensional representation of $\varepsilon^{(\mathrm{X})}$ shown in Figure S7A. As shown in equations (S2.10-S.2.12), $K^{(\rho)}$, $\mu^{(\rho)}$, and $\bar{\rho}_0$ are respectively related to the bulk modulus of the cytoskeletal components that are in compression (e.g., microtubules) $K^{(\mathrm{MT})}$, the shear modulus of the cytoskeletal components that are in compression $\mu^{(\mathrm{MT})}$, and the motor density in the quiescent state (initial motor density) ρ_0. Note that the definition used for contractility in equation (S2.9) enables us to capture the fact that contractility increases with tension. As shown in equation (1) in the main text, we will describe in Supplementary Section 6 that the average of contractility $\frac{1}{3}\rho_{kk} = (\rho_{11} + \rho_{22} + \rho_{33})/3$ increases with the average of tension $\frac{1}{3}\sigma_{kk} = (\sigma_{11} + \sigma_{22} + \sigma_{33})/3$. Equations (S2.10-S.2.12) also introduce four chemo-mechanical parameters α_{v}, α_{d}, β_{v}, and β_{d}. A large value of the volumetric chemo-mechanical feedback parameter α_{v} leads to a greater overall density of phosphorylated myosin molecular motors and subsequently higher contractility. The deviatoric chemo-mechanical feedback parameter α_{d} represents the tendency of myosin molecular motors to induce polarized contractility (small values of α_{d} cause isotropic contractility). Unlike α_{v}, a large value of the volumetric chemical stiffness β_{v} makes myosin phosphorylation more difficult, which in turn leads to lower contractility (β_{v} is proportional to the rate of myosin unbinding). Also, the deviatoric chemical stiffness β_{d} reflects the disinclination of myosin molecular motors to orient along actin filaments (a large value of β_{d} causes myosin motors to orient randomly).

2.2. Microtubules:

Experimental studies show that the internally generated cell contractile forces can compressively load microtubules[1]. In our model, the cell contractility ρ_{ij} induces compressive stress $\mathsf{C}_{ijkl}^{(\mathrm{MT})}\varepsilon_{kl}^{(\mathrm{X})}$

on microtubules where the fourth order tensor $\mathbf{C}^{(\mathrm{MT})}$ is the stiffness of microtubules and is defined as follows in our model

$$\mathsf{C}_{ijkl}^{(\mathrm{MT})} = K^{(\mathrm{MT})}\delta_{ij}\delta_{kl} + \mu^{(\mathrm{MT})}\left(\delta_{ik}\delta_{jk} + \delta_{il}\delta_{jk} - \frac{2}{3}\delta_{ij}\delta_{kl}\right) \tag{S2.13}$$

Note that in the main text, $\mathbf{C}^{(\mathrm{MT})}$, $\boldsymbol{\varepsilon}^{(\mathrm{X})}$, and $K^{(\mathrm{MT})}$ are represented by $\mathbf{C}^{(\mathrm{C})}$, $\boldsymbol{\varepsilon}^{(\mathrm{C})}$, and $K^{(\mathrm{C})}$, respectively.

2.3. Actin filaments:

As described above, microtubules are compressively loaded by the cell generated internal stress ρ_{ij}, while the rest of this internal stress, σ_{ij}, is transmitted to the extracellular matrix through the actin filament network (see equation (3) in the main text)

$$\rho_{ij} = -\mathsf{C}_{ijkl}^{(\mathrm{MT})}\varepsilon_{kl}^{(\mathrm{X})} + \sigma_{ij} \tag{S2.14}$$

Therefore, the cell contractility ρ_{ij} in our model (i) induces compressive stress $\mathsf{C}_{ijkl}^{(\mathrm{MT})}\varepsilon_{kl}^{(\mathrm{X})}$ on microtubules, and (ii) generates the tensile stress in the actin filament network, σ_{ij}.

The cell contractility in our model is initially isotropic; ρ_{ij} is the same in all directions as the cell is seeded on its substrate. To show this initial isotropic contractility, we can rewrite equation (S2.9) in the following form

$$\rho_{ij} = \mathsf{C}_{ijkl}^{(\rho)}\varepsilon_{kl}^{(\mathrm{X})} + \bar{\rho}_0\delta_{ij} \tag{S2.15}$$

where

$$\mathsf{C}_{ijkl}^{(\rho)} = K^{(\rho)}\delta_{ij}\delta_{kl} + \mu^{(\rho)}\left(\delta_{ik}\delta_{jk} + \delta_{il}\delta_{jk} - \frac{2}{3}\delta_{ij}\delta_{kl}\right) \tag{S2.16}$$

Then, from equations (S2.14) and (S2.15), we can see that the contractility tensor ρ_{ij} is isotropic in the stress-free unpolarized state $\sigma_{ij} = 0$ (i.e. the diagonal components of $\boldsymbol{\rho}$ are equal and non-zero $\rho_{11} = \rho_{22} = \rho_{33}$, while its off-diagonal components are all zero $\rho_{12} = \rho_{21} = \rho_{13} = \rho_{31} = \rho_{23} = \rho_{32} = 0$). Therefore, the cell contractility is the same in all directions (isotropic contractility) as the cell is seeded on its substrate. Figure S5 depicts that the cell initial contractility in our model is independent of direction and spatial location as the principal contractility

components ρ_1 (primarily along the long axis of the cell: the z-direction) and ρ_2 (primarily along the short axis of the cell: the x-direction) are the same everywhere in the cytoplasm at the initial configuration (ρ_1, ρ_2, and ρ_3 with $\rho_1 > \rho_2 > \rho_3$ are the eigenvalues of the contractility tensor ρ_{ij}). However, for a polarized substrate geometry (e.g., rectangular geometry), this initial isotropic contractility of the cell generates an anisotropic stress field outside of the cell where the adhesion layer experiences higher tensile stresses at the two ends along the long axis of the cell. Subsequently, the cell contractility ρ_{ij} will be no longer isotropic in the presence of the external anisotropic (polarized) tensile stress field as the cell contractility changes in our model with local stresses in an orientation-dependent manner.

Note that the local tensile stresses arise in the focal adhesion complexes activates mechanotransductive feedback mechanisms. These mechanisms are controlled by stress-activated signaling pathways such as the Ca^{2+} and the Rho-Rock pathways[4]. As depicted in Figure S6, these stress-activated signaling pathways promote motor binding (increase the concentration of the phosphorylated myosin motors) which leads to an increase in the density of force dipoles and subsequently contractility along the direction of the tensile stresses. Figure S5 illustrates how mechanical stresses arise from a polarized substrate geometry change initially isotropic contractility (with no preferential alignment of phosphorylated myosin motors) to polarized contractility along the cell polarization direction.

In addition to the cell contractility ρ_{ij}, the stress in the actin filament network σ_{ij} and the cell stiffness C_{ij} also change in an orientation dependent manner in the presence of the external polarized tensile stress field. Figure S3 shows the polarization of the stress in the actin filament network σ_{ij} as both cell contractility and substrate resistance increase along the long axis of the cell. This polarization of σ_{ij} is accompanied by cell stiffening in an orientation dependent manner. As experimentally reported[2,3], cells actively respond to tension by increasing their own stiffness, which is correlated with recruitment and alignment of actin filaments along the direction of the tensile stress. Therefore, the stiffness of actin filament network $C_{ijkl}^{(A)}$ increases with tension (but not in compression) in our model to capture the tension induced cell stiffening

$$C_{ijkl}^{(A)} = C_{ijkl}^{(I)} + C_{ijkl}^{(F)} \tag{S2.17}$$

where $\mathbf{C}^{(\mathrm{I})}$ is the initial stiffness of the actin network (e.g., the stiffness of the actin network when the cell is initially seeded on the substrate or when the substrate stiffness is negligible → $\mathbf{C}^{(\mathrm{A})} = \mathbf{C}^{(\mathrm{I})}$), and $\mathbf{C}^{(\mathrm{F})}$ denotes the tension induced stiffening of the actin network. The stiffness of the actin network in our model is initially isotropic and is obtained as

$$\mathsf{C}_{ijkl}^{(\mathrm{I})} = K^{(\mathrm{I})}\delta_{ij}\delta_{kl} + \mu^{(\mathrm{I})}\left(\delta_{ik}\delta_{jk} + \delta_{il}\delta_{jk} - \frac{2}{3}\delta_{ij}\delta_{kl}\right) \tag{S2.18}$$

where $K^{(\mathrm{I})}$ and $\mu^{(\mathrm{I})}$ are the initial bulk and shear moduli of the actin network, respectively. The initial stiffness of the actin network, $\mathsf{C}_{ijkl}^{(\mathrm{I})}$, is isotropic (independent of direction), uniform (independent of spatial location), and constant (does not change with σ_{ij}). The tension induced stiffening of the actin network is captured by the second term in equation (S2.17) as $\mathbf{C}^{(\mathrm{F})}$ increases with $\boldsymbol{\sigma}$ in an orientation dependent manner. To define $\mathbf{C}^{(\mathrm{F})}$ in our model, we first decompose the stress in the actin filament network $\boldsymbol{\sigma}$ as follows

$$\sigma_{ij} = \sigma_{ij}^{(\mathrm{A})} = \sigma_{ij}^{(\mathrm{I})} + \sigma_{ij}^{(\mathrm{F})} \tag{S2.19}$$

where $\boldsymbol{\sigma}^{(\mathrm{I})}$ is linearly related to $\boldsymbol{\varepsilon}^{(\mathrm{Y})}$ using the initial stiffness of the actin network, $\mathbf{C}^{(\mathrm{I})}$,

$$\sigma_{ij}^{(\mathrm{I})} = \mathsf{C}_{ijkl}^{(\mathrm{I})}\,\varepsilon_{kl}^{(\mathrm{Y})} \tag{S2.20}$$

The strain tensor $\boldsymbol{\varepsilon}^{(\mathrm{Y})}$ in (S2.20) is the three-dimensional representation of $\varepsilon^{(\mathrm{Y})}$ shown in Figure S7A. $\boldsymbol{\varepsilon}^{(\mathrm{Y})}$ can be represented as a function of its principal strains (eigenvalues) $\varepsilon_1^{(\mathrm{Y})}$, $\varepsilon_2^{(\mathrm{Y})}$, and $\varepsilon_3^{(\mathrm{Y})}$ via the following spectral decomposition

$$\boldsymbol{\varepsilon}^{(\mathrm{Y})} = \sum_{i=1}^{3} \varepsilon_i^{(\mathrm{Y})}\,\boldsymbol{n}_i \otimes \boldsymbol{n}_i = \sum_{i=1}^{3} \varepsilon_i^{(\mathrm{Y})}\,\mathbf{E}_i \tag{S2.21}$$

where the orthogonal eigenvectors $\boldsymbol{n}_1$, $\boldsymbol{n}_2$, and $\boldsymbol{n}_3$ are the unit vectors in the directions of the principal strains $\varepsilon_1^{(\mathrm{Y})}$, $\varepsilon_2^{(\mathrm{Y})}$, and $\varepsilon_3^{(\mathrm{Y})}$, respectively. In equation (S2.21), $\otimes$ denotes the dyadic product of two arbitrary vectors $\boldsymbol{u}$ and $\boldsymbol{v}$ as $(\boldsymbol{u} \otimes \boldsymbol{v})_{ij} = u_i v_j$. Also, the symmetric tensors $\mathbf{E}_1 =$

$\boldsymbol{n}_1 \otimes \boldsymbol{n}_1$, $\mathbf{E}_2 = \boldsymbol{n}_2 \otimes \boldsymbol{n}_2$, and $\mathbf{E}_3 = \boldsymbol{n}_3 \otimes \boldsymbol{n}_3$ are the eigenprojections of $\boldsymbol{\varepsilon}^{(\mathrm{Y})}$. With the eigenvalues and eigenvectors of $\boldsymbol{\varepsilon}^{(\mathrm{Y})}$ at hand, we define $\sigma_{ij}^{(\mathrm{F})}$ in equation (S2.19) as follows

$$\boldsymbol{\sigma}^{(\mathrm{F})} = \sum_{i=1}^{3} \frac{\partial f(\varepsilon_i^{(\mathrm{Y})})}{\partial \varepsilon_i^{(\mathrm{Y})}} \boldsymbol{n}_i \otimes \boldsymbol{n}_i = \sum_{i=1}^{3} \sigma^{(\mathrm{F})}\left(\varepsilon_i^{(\mathrm{Y})}\right) \mathbf{E}_i = \sum_{i=1}^{3} \sigma_i^{(\mathrm{F})}\ \mathbf{E}_i \tag{S2.22}$$

where the derivative of the energy function $f(\varepsilon_i^{(\mathrm{Y})})$ is defined as

$$\sigma_i^{(\mathrm{F})} = \frac{\partial f\left(\varepsilon_i^{(\mathrm{Y})}\right)}{\partial \varepsilon_i^{(\mathrm{Y})}} = \tag{S2.23}$$

$$\begin{cases} 0 & \varepsilon_i^{(\mathrm{Y})} < \epsilon_1 \\ \ell\left[\dfrac{\left(\dfrac{\varepsilon_i^{(\mathrm{Y})} - \epsilon_1}{\epsilon_2 - \epsilon_1}\right)^n \left(\varepsilon_i^{(\mathrm{Y})} - \epsilon_1\right)^2}{(n+1)(n+2)}\right] & \epsilon_1 \le \varepsilon_i^{(\mathrm{Y})} < \epsilon_2 \\ \ell\left[\dfrac{\left(1 + \varepsilon_i^{(\mathrm{Y})} - \epsilon_2\right)^{m+2} - 1}{(m+1)(m+2)} + \dfrac{\epsilon_2 - \varepsilon_i^{(\mathrm{Y})}}{m+1} + \dfrac{(\varepsilon_i^{(\mathrm{Y})} - \epsilon_2)(\epsilon_2 - \epsilon_1)}{n+1} + \dfrac{(\epsilon_2 - \epsilon_1)^2}{(n+1)(n+2)}\right] & \varepsilon_i^{(\mathrm{Y})} \ge \epsilon_2 \end{cases}$$

to ensure that the first and second derivatives of the strain-stress curve in the principal direction "i" ($\sigma_i^{(\mathrm{F})}$ as a function of $\varepsilon_i^{(\mathrm{Y})}$) are continuous. As shown in equation (S2.23), $\partial f/\partial \varepsilon_i^{(\mathrm{Y})}$ and subsequently the principal stress $\sigma_i^{(\mathrm{F})}$ vanish for $\varepsilon_i^{(\mathrm{Y})}$ below $\epsilon_1 = \epsilon_{\mathrm{c}} - 0.5\epsilon_{\mathrm{t}}$ where ϵ_{c} and $\epsilon_{\mathrm{t}} = 0.25\epsilon_{\mathrm{c}}$ are the critical (tensile) principal strain and transition width, respectively. We use a smooth transition function (interpolation function) for $\epsilon_1 \le \varepsilon_i^{(\mathrm{Y})} < \epsilon_2$ to ensure the continuity and smoothness of $\partial f/\partial \varepsilon_i^{(\mathrm{Y})}$ at the transition points $\epsilon_1 = \epsilon_{\mathrm{c}} - 0.5\epsilon_{\mathrm{t}}$ and $\epsilon_2 = \epsilon_{\mathrm{c}} + 0.5\epsilon_{\mathrm{t}}$ where n is the transition constant. For $\varepsilon_i^{(\mathrm{Y})} \ge \epsilon_2$, equation (S2.23) shows that the principal stress $\sigma_i^{(\mathrm{F})}$ is a nonlinear function of the principal strain $\varepsilon_i^{(\mathrm{Y})}$ where ℓ and m are stiffening parameters. The stiffening parameter ℓ can be a function of nuclear envelope lamina stiffness as recent experimental studies[10] show depolymerization of apical actin stress fibers in the absence of lamin A,C in mouse embryonic fibroblasts. This can be captured in our model by assuming that ℓ

decreases with lamin A,C knockout (lamin stiffening parameter $\hat{\ell} \approx 0$ as described in Supplementary Section 3.1).

With $\boldsymbol{\sigma}^{(\mathrm{F})}$ at hand from equation (S2.22), using a piecewise linear approximation, we can now define $\mathbf{C}^{(\mathrm{F})}$ as follows

$$\mathrm{C}_{ijkl}^{(\mathrm{F})} = \frac{\mathrm{d}\sigma_{ij}^{(\mathrm{F})}}{\mathrm{d}\varepsilon_{kl}^{(\mathrm{Y})}} \qquad \text{or} \qquad \mathbf{C}^{(\mathrm{F})} = \frac{\mathrm{d}\boldsymbol{\sigma}^{(\mathrm{F})}}{\mathrm{d}\boldsymbol{\varepsilon}^{(\mathrm{Y})}} \tag{S2.24}$$

Note that equation (S2.23) gives the principal stress $\sigma_i^{(\mathrm{F})}$ as a function of the principal strain $\varepsilon_i^{(\mathrm{Y})}$ and not $\sigma_{ij}^{(\mathrm{F})}$ as a function of $\varepsilon_{ij}^{(\mathrm{Y})}$. Therefore, using the spectral decomposition of $\boldsymbol{\sigma}^{(\mathrm{F})}$ in equation (S2.22), we rewrite equation (S2.24) in the following form[13]

$$\mathbf{C}^{(\mathrm{F})} = \sum_{i=1}^{3} \left\{ \mathbf{E}_i \otimes \frac{\mathrm{d}\sigma_i^{(\mathrm{F})}}{\mathrm{d}\boldsymbol{\varepsilon}^{(\mathrm{Y})}} + \sigma_i^{(\mathrm{F})} \frac{\mathrm{d}\mathbf{E}_i}{\mathrm{d}\boldsymbol{\varepsilon}^{(\mathrm{Y})}} \right\} \tag{S2.25}$$

As the principal stress $\sigma_i^{(\mathrm{F})}$ is a function of the principal strain $\varepsilon_i^{(\mathrm{Y})}$ in equation (S2.23), we can rewrite equation (S2.17) by applying the chain rule to its first term

$$\mathbf{C}^{(\mathrm{F})} = \sum_{i=1}^{3} \left\{ \sum_{j=1}^{3} \frac{\partial \sigma_i^{(\mathrm{F})}}{\partial \varepsilon_j^{(\mathrm{Y})}} \mathbf{E}_i \otimes \frac{\mathrm{d}\varepsilon_j^{(\mathrm{Y})}}{\mathrm{d}\boldsymbol{\varepsilon}^{(\mathrm{Y})}} + \sigma_i^{(\mathrm{F})} \frac{\mathrm{d}\mathbf{E}_i}{\mathrm{d}\boldsymbol{\varepsilon}^{(\mathrm{Y})}} \right\} \tag{S2.26}$$

If $\varepsilon_{ij}^{(\mathrm{Y})}$ has three distinct eigenvalues ($\varepsilon_1^{(\mathrm{Y})} \neq \varepsilon_2^{(\mathrm{Y})} \neq \varepsilon_3^{(\mathrm{Y})}$), by taking the derivatives of $\varepsilon_j^{(\mathrm{Y})}$ and $\mathbf{E}_i$ with respect to $\boldsymbol{\varepsilon}^{(\mathrm{Y})}$ in (S2.26), we can derive $\mathbf{C}^{(\mathrm{F})}$ as follows

$$\begin{aligned} \mathbf{C}^{(\mathrm{F})} = \sum_{a=1}^{3} \frac{\sigma_a^{(\mathrm{F})}}{(\varepsilon_a^{(\mathrm{Y})} - \varepsilon_b^{(\mathrm{Y})})(\varepsilon_a^{(\mathrm{Y})} - \varepsilon_c^{(\mathrm{Y})})} \Bigg\{ & \frac{\mathrm{d}\left(\boldsymbol{\varepsilon}^{(\mathrm{Y})}\right)^2}{\mathrm{d}\boldsymbol{\varepsilon}^{(\mathrm{Y})}} - \left(\varepsilon_b^{(\mathrm{Y})} + \varepsilon_c^{(\mathrm{Y})}\right)\mathbf{I}_{\mathrm{S}} \\ & - \left[\left(\varepsilon_a^{(\mathrm{Y})} - \varepsilon_b^{(\mathrm{Y})}\right) + \left(\varepsilon_a^{(\mathrm{Y})} - \varepsilon_c^{(\mathrm{Y})}\right)\right] \mathbf{E}_a \otimes \mathbf{E}_a \\ & - \left(\varepsilon_b^{(\mathrm{Y})} - \varepsilon_c^{(\mathrm{Y})}\right)(\mathbf{E}_b \otimes \mathbf{E}_b - \mathbf{E}_c \otimes \mathbf{E}_c) \Bigg\} + \sum_{i=1}^{3} \sum_{j=1}^{3} \frac{\partial \sigma_i^{(\mathrm{F})}}{\partial \varepsilon_j^{(\mathrm{Y})}} \mathbf{E}_i \otimes \mathbf{E}_j \end{aligned} \tag{S2.27}$$

where the fourth order tensor $\mathrm{d}\left(\boldsymbol{\varepsilon}^{(\mathrm{Y})}\right)^2 / \mathrm{d}\boldsymbol{\varepsilon}^{(\mathrm{Y})}$ is the derivative of the square of the second order tensor $\boldsymbol{\varepsilon}^{(\mathrm{Y})}$ and is obtained as follows

$$\left(\frac{\mathrm{d}\left(\boldsymbol{\varepsilon}^{(\mathrm{Y})}\right)^2}{\mathrm{d}\boldsymbol{\varepsilon}^{(\mathrm{Y})}}\right)_{ijkl} = \frac{1}{2}\left(\delta_{ik}\varepsilon_{lj}^{(\mathrm{Y})} + \delta_{il}\varepsilon_{kj}^{(\mathrm{Y})} + \delta_{jl}\varepsilon_{ik}^{(\mathrm{Y})} + \delta_{kj}\varepsilon_{il}^{(\mathrm{Y})}\right) \tag{S2.28}$$

and $\mathbf{I}_{\mathrm{S}}$ is the fourth order symmetric identity tensor

$$(\mathbf{I}_{\mathrm{S}})_{ijkl} = \frac{1}{2}(\mathbf{I} + \mathbf{I}_{\mathrm{T}}) = \frac{1}{2}\left(\delta_{ik}\delta_{jl} + \delta_{il}\delta_{jk}\right) \tag{S2.29}$$

If there are two identical eigenvalues ($\varepsilon_1^{(\mathrm{Y})} \neq \varepsilon_2^{(\mathrm{Y})} = \varepsilon_3^{(\mathrm{Y})}$), then $\mathbf{C}^{(\mathrm{F})}$ is obtained from the following equation

$$\mathbf{C}^{(\mathrm{F})} = s_1\frac{\mathrm{d}\left(\boldsymbol{\varepsilon}^{(\mathrm{Y})}\right)^2}{\mathrm{d}\boldsymbol{\varepsilon}^{(\mathrm{Y})}} - s_2\mathbf{I}_{\mathrm{S}} - s_3\boldsymbol{\varepsilon}^{(\mathrm{Y})}\otimes\boldsymbol{\varepsilon}^{(\mathrm{Y})} + s_4\boldsymbol{\varepsilon}^{(\mathrm{Y})}\otimes\mathbf{I} + s_5\mathbf{I}\otimes\boldsymbol{\varepsilon}^{(\mathrm{Y})} - s_6\mathbf{I}\otimes\mathbf{I} \tag{S2.30}$$

where $\mathbf{I}$ is the second order identity tensor

$$\mathrm{I}_{ij} = \delta_{ij} \tag{S2.31}$$

and the constants s_1, s_2, s_3, s_4, s_5, and s_6 are given as follows

$$s_1 = \frac{\sigma_a^{(\mathrm{F})} - \sigma_c^{(\mathrm{F})}}{\left(\varepsilon_a^{(\mathrm{Y})} - \varepsilon_c^{(\mathrm{Y})}\right)^2} + \frac{1}{\varepsilon_a^{(\mathrm{Y})} - \varepsilon_c^{(\mathrm{Y})}}\left(\frac{\partial\sigma_c^{(\mathrm{F})}}{\partial\varepsilon_b^{(\mathrm{Y})}} - \frac{\partial\sigma_c^{(\mathrm{F})}}{\partial\varepsilon_c^{(\mathrm{Y})}}\right) \tag{S2.32a}$$

$$s_2 = 2\varepsilon_c^{(\mathrm{Y})}\frac{\sigma_a^{(\mathrm{F})} - \sigma_c^{(\mathrm{F})}}{\left(\varepsilon_a^{(\mathrm{Y})} - \varepsilon_c^{(\mathrm{Y})}\right)^2} + \frac{\varepsilon_a^{(\mathrm{Y})} + \varepsilon_c^{(\mathrm{Y})}}{\varepsilon_a^{(\mathrm{Y})} - \varepsilon_c^{(\mathrm{Y})}}\left(\frac{\partial\sigma_c^{(\mathrm{F})}}{\partial\varepsilon_b^{(\mathrm{Y})}} - \frac{\partial\sigma_c^{(\mathrm{F})}}{\partial\varepsilon_c^{(\mathrm{Y})}}\right) \tag{S2.32b}$$

$$s_3 = 2\frac{\sigma_a^{(\mathrm{F})} - \sigma_c^{(\mathrm{F})}}{\left(\varepsilon_a^{(\mathrm{Y})} - \varepsilon_c^{(\mathrm{Y})}\right)^3} + \frac{1}{\left(\varepsilon_a^{(\mathrm{Y})} - \varepsilon_c^{(\mathrm{Y})}\right)^2}\left(\frac{\partial\sigma_a^{(\mathrm{F})}}{\partial\varepsilon_c^{(\mathrm{Y})}} + \frac{\partial\sigma_c^{(\mathrm{F})}}{\partial\varepsilon_a^{(\mathrm{Y})}} - \frac{\partial\sigma_a^{(\mathrm{F})}}{\partial\varepsilon_a^{(\mathrm{Y})}} - \frac{\partial\sigma_c^{(\mathrm{F})}}{\partial\varepsilon_c^{(\mathrm{Y})}}\right) \tag{S2.32c}$$

$$\begin{aligned} s_4 = {} & 2\varepsilon_c^{(\mathrm{Y})}\frac{\sigma_a^{(\mathrm{F})} - \sigma_c^{(\mathrm{F})}}{\left(\varepsilon_a^{(\mathrm{Y})} - \varepsilon_c^{(\mathrm{Y})}\right)^3} + \frac{1}{\varepsilon_a^{(\mathrm{Y})} - \varepsilon_c^{(\mathrm{Y})}}\left(\frac{\partial\sigma_a^{(\mathrm{F})}}{\partial\varepsilon_c^{(\mathrm{Y})}} - \frac{\partial\sigma_c^{(\mathrm{F})}}{\partial\varepsilon_b^{(\mathrm{Y})}}\right) \\ & + \frac{\varepsilon_c^{(\mathrm{Y})}}{\left(\varepsilon_a^{(\mathrm{Y})} - \varepsilon_c^{(\mathrm{Y})}\right)^2}\left(\frac{\partial\sigma_a^{(\mathrm{F})}}{\partial\varepsilon_c^{(\mathrm{Y})}} + \frac{\partial\sigma_c^{(\mathrm{F})}}{\partial\varepsilon_a^{(\mathrm{Y})}} - \frac{\partial\sigma_a^{(\mathrm{F})}}{\partial\varepsilon_a^{(\mathrm{Y})}} - \frac{\partial\sigma_c^{(\mathrm{F})}}{\partial\varepsilon_c^{(\mathrm{Y})}}\right) \end{aligned} \tag{S2.32d}$$

$$s_5 = 2\varepsilon_c^{(\mathrm{Y})}\frac{\sigma_a^{(\mathrm{F})}-\sigma_c^{(\mathrm{F})}}{\left(\varepsilon_a^{(\mathrm{Y})}-\varepsilon_c^{(\mathrm{Y})}\right)^3}+\frac{1}{\varepsilon_a^{(\mathrm{Y})}-\varepsilon_c^{(\mathrm{Y})}}\left(\frac{\partial\sigma_c^{(\mathrm{F})}}{\partial\varepsilon_a^{(\mathrm{Y})}}-\frac{\partial\sigma_c^{(\mathrm{F})}}{\partial\varepsilon_b^{(\mathrm{Y})}}\right)$$
$$+\frac{\varepsilon_c^{(\mathrm{Y})}}{\left(\varepsilon_a^{(\mathrm{Y})}-\varepsilon_c^{(\mathrm{Y})}\right)^2}\left(\frac{\partial\sigma_a^{(\mathrm{F})}}{\partial\varepsilon_c^{(\mathrm{Y})}}+\frac{\partial\sigma_c^{(\mathrm{F})}}{\partial\varepsilon_a^{(\mathrm{Y})}}-\frac{\partial\sigma_a^{(\mathrm{F})}}{\partial\varepsilon_a^{(\mathrm{Y})}}-\frac{\partial\sigma_c^{(\mathrm{F})}}{\partial\varepsilon_c^{(\mathrm{Y})}}\right) \quad \text{(S2.32e)}$$

$$s_6 = 2\varepsilon_c^{(\mathrm{Y})}\frac{\sigma_a^{(\mathrm{F})}-\sigma_c^{(\mathrm{F})}}{\left(\varepsilon_a^{(\mathrm{Y})}-\varepsilon_c^{(\mathrm{Y})}\right)^3}+\frac{\varepsilon_a^{(\mathrm{Y})}\varepsilon_c^{(\mathrm{Y})}}{\left(\varepsilon_a^{(\mathrm{Y})}-\varepsilon_c^{(\mathrm{Y})}\right)^2}\left(\frac{\partial\sigma_a^{(\mathrm{F})}}{\partial\varepsilon_c^{(\mathrm{Y})}}+\frac{\partial\sigma_c^{(\mathrm{F})}}{\partial\varepsilon_a^{(\mathrm{Y})}}\right)-\frac{\left(\varepsilon_c^{(\mathrm{Y})}\right)^2}{\left(\varepsilon_a^{(\mathrm{Y})}-\varepsilon_c^{(\mathrm{Y})}\right)^2}\left(\frac{\partial\sigma_a^{(\mathrm{F})}}{\partial\varepsilon_a^{(\mathrm{Y})}}+\frac{\partial\sigma_c^{(\mathrm{F})}}{\partial\varepsilon_c^{(\mathrm{Y})}}\right)$$
$$-\frac{\varepsilon_a^{(\mathrm{Y})}+\varepsilon_c^{(\mathrm{Y})}}{\varepsilon_a^{(\mathrm{Y})}-\varepsilon_c^{(\mathrm{Y})}}\frac{\partial\sigma_c^{(\mathrm{F})}}{\partial\varepsilon_b^{(\mathrm{Y})}} \quad \text{(S2.32f)}$$

where (a, b, c) are here cyclic permutations of (1,2,3).

Finally, if there are three identical eigenvalues ($\varepsilon_1^{(\mathrm{Y})} = \varepsilon_2^{(\mathrm{Y})} = \varepsilon_3^{(\mathrm{Y})}$), then $\mathbf{C}^{(\mathrm{F})}$ is given by

$$\mathbf{C}^{(\mathrm{F})} = \left(\frac{\partial\sigma_1^{(\mathrm{F})}}{\partial\varepsilon_1^{(\mathrm{Y})}}-\frac{\partial\sigma_1^{(\mathrm{F})}}{\partial\varepsilon_2^{(\mathrm{Y})}}\right)\mathbf{I}_{\mathrm{S}}+\frac{\partial\sigma_1^{(\mathrm{F})}}{\partial\varepsilon_2^{(\mathrm{Y})}}\mathbf{I}\otimes\mathbf{I} \quad \text{(S2.33)}$$

The term $\partial\sigma_i^{(\mathrm{F})}/\,\partial\varepsilon_j^{(\mathrm{Y})}$ in all above equations (equations (S2.27), (S2.32), and (S2.33)) can be derived from equation (S2.23) by taking its derivative as follows

$$\frac{\partial\sigma_i^{(\mathrm{F})}}{\partial\varepsilon_i^{(\mathrm{Y})}} = \frac{\partial}{\partial\varepsilon_i^{(\mathrm{Y})}}\left(\frac{\partial f}{\partial\varepsilon_i^{(\mathrm{Y})}}\right) = \begin{cases} 0 & \varepsilon_i^{(\mathrm{Y})} < \epsilon_1 \\ \ell\left[\dfrac{\left(\dfrac{\varepsilon_i^{(\mathrm{Y})}-\epsilon_1}{\epsilon_2-\epsilon_1}\right)^n\left(\varepsilon_i^{(\mathrm{Y})}-\epsilon_1\right)}{n+1}\right] & \epsilon_1 \le \varepsilon_i^{(\mathrm{Y})} < \epsilon_2 \\ \ell\left[\dfrac{\left(1+\varepsilon_i^{(\mathrm{Y})}-\epsilon_2\right)^{m+1}-1}{m+1}+\dfrac{\epsilon_2-\epsilon_1}{n+1}\right] & \varepsilon_i^{(\mathrm{Y})} \ge \epsilon_2 \end{cases}$$
(S2.34)

Note that in our formulation, $\sigma_i^{(\mathrm{F})}$ is a function of $\varepsilon_i^{(\mathrm{Y})}$ only and thus there is no dependence of $\sigma_i^{(\mathrm{F})}$ on $\varepsilon_j^{(\mathrm{Y})}$ for $i \neq j$.

With $\mathbf{C}^{(\mathrm{F})}$ at hand, the stiffness of actin filament network $\mathbf{C}^{(\mathrm{A})}$ can be obtained from equation (S2.17). As shown above, $\mathbf{C}^{(\mathrm{F})}$ is a function of $\boldsymbol{\varepsilon}^{(\mathrm{Y})}$. Therefore, the stiffness of actin filament network $\mathbf{C}^{(\mathrm{A})} = \mathbf{C}^{(\mathrm{I})} + \mathbf{C}^{(\mathrm{F})}$ increases with tensile stress $\boldsymbol{\sigma}^{(\mathrm{F})}$ in an orientation dependent manner.

2.4. Cytoskeletal total stiffness:

The cytoskeleton in our model is composed of (i) the myosin molecular motors, (ii) the microtubules, and (iii) the actin filaments. As shown in Figure S7A, the actin filament network is connected to the other two elements (the myosin motors and the microtubules) in series. Thus, similar to our one-dimensional model in (S1.6), the total stiffness of the cell, $\mathbf{C}$, in our three-dimensional model can be obtained as follows

$$\mathbf{C} = \left(\left(\mathbf{C}^{(\mathrm{X})}\right)^{-1} + \left(\mathbf{C}^{(\mathrm{Y})}\right)^{-1}\right)^{-1} \tag{S2.35a}$$

where

$$\mathbf{C}^{(\mathrm{X})} = \mathbf{C}^{(\rho)} + \mathbf{C}^{(\mathrm{MT})} \tag{S2.35b}$$

and

$$\mathbf{C}^{(\mathrm{Y})} = \mathbf{C}^{(\mathrm{A})} = \mathbf{C}^{(\mathrm{I})} + \mathbf{C}^{(\mathrm{F})} \tag{S2.35c}$$

In equation (S2.35), the second order tensors $\mathbf{C}^{(\rho)}$, $\mathbf{C}^{(\mathrm{MT})}$, and $\mathbf{C}^{(\mathrm{A})}$ are the 6×6 matrix representations of the fourth order tensors $\mathbf{C}^{(\rho)}$ (equation S2.16), $\mathbf{C}^{(\mathrm{MT})}$ (equation S2.13), and $\mathbf{C}^{(\mathrm{A})}$ (equation S2.17), respectively. The reader is referred to SI Section 5 where a fourth order tensor (e.g., C_{ijkl}) degrades to a 6×6 square matrix (e.g., C_{ij}).

As the stiffness of actin filament network $\mathbf{C}^{(\mathrm{A})}$ is a function of $\boldsymbol{\varepsilon}^{(\mathrm{Y})}$, the total stiffness of the cytoskeleton $\mathbf{C}$ increases with the cell contractility $\boldsymbol{\rho}$ and the tensile stress $\boldsymbol{\sigma}$ in an orientation dependent manner as shown in our simulations in Figure S8.

2.5. The system of nonlinear equations:

As described above, the total cytoskeletal stress field σ_{ij} in our constitutive model can be determined from (S2.14) or (S2.19). Also, the total cytoskeletal stiffness C_{ij} is given by equation (S2.35). However, both tensors σ_{ij} and C_{ij} are functions of unknown tensors $\varepsilon_{ij}^{(\mathrm{X})}$ and $\varepsilon_{ij}^{(\mathrm{Y})}$.

Therefore, we first need to determine our unknowns $\varepsilon_{ij}^{(X)}$ and $\varepsilon_{ij}^{(Y)}$ using an iterative procedure. To this end, we first define the 12×1 vector $\boldsymbol{u}$

$$\boldsymbol{u} = \{u_1 \quad u_2 \quad \dots \quad u_{12}\}^{\mathrm{T}} \tag{S2.36a}$$

which contains our unknown variables

$$\boldsymbol{u} = \left\{\varepsilon_{11}^{(X)} \quad \varepsilon_{22}^{(X)} \quad \varepsilon_{33}^{(X)} \quad \varepsilon_{12}^{(X)} \quad \varepsilon_{13}^{(X)} \quad \varepsilon_{23}^{(X)} \quad \varepsilon_{11}^{(Y)} \quad \varepsilon_{22}^{(Y)} \quad \varepsilon_{33}^{(Y)} \quad \varepsilon_{12}^{(Y)} \quad \varepsilon_{13}^{(Y)} \quad \varepsilon_{23}^{(Y)}\right\}^{\mathrm{T}} \tag{S2.36b}$$

To determine these 12 unknowns, we need 12 equations to define our system of equations. As the stress generated by the actomyosin contractility is directly transmitted to the actin filament network, 6 of these 12 equations are obtained from the following condition

$$\boldsymbol{\sigma} = \boldsymbol{\sigma}^{(X)} = \boldsymbol{\sigma}^{(Y)} \tag{S2.37}$$

where $\boldsymbol{\sigma}^{(X)}$ is the stress generated by the actomyosin contractility which is given by equations (S2.14) and (S2.15) as follows

$$\sigma_{ij}^{(X)} = \sigma_{ij} = \left(\mathsf{C}_{ijkl}^{(\rho)} + \mathsf{C}_{ijkl}^{(MT)}\right)\varepsilon_{kl}^{(X)} + \bar{\rho}_0\delta_{ij} \tag{S2.38}$$

and $\boldsymbol{\sigma}^{(Y)}$ is the stress transmitted to the actin filament network which is determined from equation (S2.19)

$$\sigma_{ij}^{(Y)} = \sigma_{ij} = \sigma_{ij}^{(A)} = \sigma_{ij}^{(I)} + \sigma_{ij}^{(F)} \tag{S2.39}$$

The other 6 equations can be obtained from the following condition

$$\boldsymbol{\varepsilon} = \boldsymbol{\varepsilon}^{(X)} + \boldsymbol{\varepsilon}^{(Y)} \tag{S2.40}$$

where the second order tensor $\boldsymbol{\varepsilon}$ is the total strain of the cell. As both stress and strain tensors $\sigma_{ij}^{(X)}$, $\sigma_{ij}^{(Y)}$, $\varepsilon_{ij}^{(X)}$, and $\varepsilon_{ij}^{(Y)}$ are symmetric, we can define the 12×1 vector $\boldsymbol{f}$

$$\boldsymbol{f} = \{f_1 \quad f_2 \quad \dots \quad f_{12}\}^{\mathrm{T}} \tag{S2.41a}$$

which contains our 12 equations

$$f_1 = \sigma_{11}^{(X)} - \sigma_{11}^{(Y)} \tag{S2.41b}$$

$$f_2 = \sigma_{22}^{(X)} - \sigma_{22}^{(Y)} \tag{S2.41c}$$

$$f_3 = \sigma_{33}^{(X)} - \sigma_{33}^{(Y)} \tag{S2.41d}$$

$$f_4 = \sigma_{12}^{(X)} - \sigma_{12}^{(Y)} \tag{S2.41e}$$

$$f_5 = \sigma_{13}^{(X)} - \sigma_{13}^{(Y)} \tag{S2.41f}$$

$$f_6 = \sigma_{23}^{(X)} - \sigma_{23}^{(Y)} \tag{S2.41g}$$

$$f_7 = \varepsilon_{11} - \varepsilon_{11}^{(X)} - \varepsilon_{11}^{(Y)} \tag{S2.41h}$$

$$f_8 = \varepsilon_{22} - \varepsilon_{22}^{(X)} - \varepsilon_{22}^{(Y)} \tag{S2.41i}$$

$$f_9 = \varepsilon_{33} - \varepsilon_{33}^{(X)} - \varepsilon_{33}^{(Y)} \tag{S2.41j}$$

$$f_{10} = \varepsilon_{12} - \varepsilon_{12}^{(X)} - \varepsilon_{12}^{(Y)} \tag{S2.41k}$$

$$f_{11} = \varepsilon_{13} - \varepsilon_{13}^{(X)} - \varepsilon_{13}^{(Y)} \tag{S2.41l}$$

$$f_{12} = \varepsilon_{23} - \varepsilon_{23}^{(X)} - \varepsilon_{23}^{(Y)} \tag{S2.41m}$$

Using equations (S2.36) and (S2.41) for u_i and f_i, the 12×12 Jacobian matrix **J** is determined as follows

$$\mathbf{J} = \begin{bmatrix} \partial f_1/\partial u_1 & \partial f_1/\partial u_2 & \dots & \partial f_1/\partial u_{12} \\ \partial f_2/\partial u_1 & \partial f_2/\partial u_2 & \dots & \partial f_2/\partial u_{12} \\ \vdots & \vdots & & \vdots \\ . & . & & . \\ \partial f_{12}/\partial u_1 & \partial f_{12}/\partial u_2 & \dots & \partial f_{12}/\partial u_{12} \end{bmatrix} = \begin{bmatrix} \mathbf{C}^{(X)} & -\mathbf{C}^{(Y)} \\ -\mathbf{I} & -\mathbf{I} \end{bmatrix} \tag{S2.42}$$

Finally, the Newton-Raphson method is implemented to determine the unknown vector $\boldsymbol{u}$

$$\boldsymbol{u}_{n+1} = \boldsymbol{u}_n - \mathbf{J}^{-1}\boldsymbol{f}(\boldsymbol{u}_n) \tag{S2.43}$$

where $\boldsymbol{u}_n$ and $\boldsymbol{u}_{n+1}$ are the solutions for n and $n+1$ iterations, respectively. We use the following initial guess $\boldsymbol{u}_0$ and convergence criterion for the solution of the system of nonlinear equations

$$\boldsymbol{u}_0 = \{0 \quad 0 \quad \dots \quad 0\}_{1\times 12}^{\mathrm{T}} \tag{S2.44}$$

$$|\boldsymbol{f}| = \sqrt{(f_1)^2 + (f_2)^2 + \cdots + (f_{12})^2} < \epsilon_{\mathrm{Tol}} \tag{S2.45}$$

where ϵ_{Tol} is the convergence threshold. Using $\epsilon_{\mathrm{Tol}} = 10^{-8}$ in our simulations, we stop the iterative process (S2.43) when the magnitude of the vector $\boldsymbol{f}$ is less than ϵ_{Tol} as shown in equation (S2.45). With $\varepsilon_{ij}^{(\mathrm{X})}$ and $\varepsilon_{ij}^{(\mathrm{Y})}$ obtained from (S2.43), we can now calculate the total cytoskeletal stress field σ_{ij} from (S2.38) or (S2.39) and the total cytoskeletal stiffness C_{ij} from (S2.35) to complete our constitutive equations.

2.6. Actomyosin contractility increases with anisotropy in tension:

Combining equation (S2.14) with (S2.15), the average of contractility, $\frac{1}{3}\rho_{kk} = (\rho_{11} + \rho_{22} + \rho_{33})/3$, can be written as follows

$$\frac{\rho_{kk}}{3} = \left(\frac{3K^{(\mathrm{MT})}\alpha_{\mathrm{v}} - 1}{3K^{(\mathrm{MT})}\beta_{\mathrm{v}} - 1}\right)\frac{\sigma_{kk}}{3} + \left(\frac{3K^{(\mathrm{MT})}\beta_{\mathrm{v}}}{3K^{(\mathrm{MT})}\beta_{\mathrm{v}} - 1}\right)\rho_{0,} \tag{S2.46}$$

which shows that $\frac{1}{3}\rho_{kk}$ increases with the average of stress, $\frac{1}{3}\sigma_{kk} = (\sigma_{11} + \sigma_{22} + \sigma_{33})/3$. This is consistent with our experiments in Figure S25 where we observe higher levels of phosphorylated myosin light chain (p-MLC) with increasing substrate area (increasing $\frac{1}{3}\sigma_{kk}$). Our experiments in Figure S22 also show higher levels of p-MLC in rectangular cells (anisotropic tension) compared to the square cells (isotropic tension) with the same substrate area. This indicates that myosin phosphorylation increases with anisotropy in the components of the stress tensor σ_{ij}. To capture the increase in actomyosin contractility in response to anisotropy in tension, we modify equation (S2.46) as follows

$$\frac{\rho_{kk}}{3} = \left(\frac{3K^{(\mathrm{MT})}\alpha_{\mathrm{v}} - 1}{3K^{(\mathrm{MT})}\beta_{\mathrm{v}} - 1}\right)\frac{\sigma_{kk}}{3} + \alpha_{\mathrm{a}}\sigma_{\mathrm{a}} + \left(\frac{3K^{(\mathrm{MT})}\beta_{\mathrm{v}}}{3K^{(\mathrm{MT})}\beta_{\mathrm{v}} - 1}\right)\rho_0 \tag{S2.47}$$

where $\sigma_{\mathrm{a}} = \tanh\left(\frac{1}{2}\left(\frac{\sigma_1}{\sigma_2} - 1\right)\right)\sigma_1$ represents the anisotropy in tension (stress polarization) while $\sigma_1 > \sigma_2 > \sigma_3$ are the principal stress values of the stress tensor σ_{ij} with $\sigma_1 > \sigma_2 > 0$. In equation (S2.47), α_{a} is the anisotropic chemo-mechanical feedback parameter which regulates the increase in myosin phosphorylation with anisotropic tension. To implement equation (S2.47) in our finite

element framework, we use a piecewise linear approximation and we simply replace ρ_0 in equation (S2.12) with $\rho_0 + \left(\frac{3K^{(\mathrm{MT})}\beta_{\mathrm{v}}-1}{3K^{(\mathrm{MT})}\beta_{\mathrm{v}}}\right)\alpha_{\mathrm{a}}\sigma_{\mathrm{a}}$ in each step of simulation.

3. Computational model for nuclear mechanics

The nuclear envelope lamina network and chromatin are known to be key mechanical components of the nucleus. The nucleus is here modeled as an elastic thin layer (representing the nuclear envelope) filled with a solid material which represents chromatin and other subnuclear components (Figure S35A).

3.1. Nuclear envelope:

The nuclear envelope is one of the major components of the nucleus which encloses the genetic materials and provides the nucleus with structural integrity. The nuclear envelope is composed of (i) the inner and outer membranes which are both lipid bilayers (each of these membranes consists of two layers of lipid molecules). The space between the inner and outer membranes is called the perinuclear space. Nuclear pores pass through both the inner and outer membranes and connect them together. (ii) The nuclear lamina is a complex peripheral mesh-like network underneath of the inner nuclear membrane and is composed of lamins and nuclear membrane-associated proteins. The nuclear lamins are type V intermediate filaments and provide structural support to the nucleus. Lamins are divided into A and B types where lamins A and C are two major A-type lamins while lamins B1 and B2 are two major B-type lamins. We and other researchers have shown that lamin A,C deficiency in mouse embryonic stem cells[14] and mouse embryonic fibroblasts[15] causes nuclear softening.

As reported in recent experimental studies[6], single isolated nuclei exhibit significant strain stiffening at large extensions when they are uniaxially stretched using micropipette manipulation technique (Figure S35B). The strain stiffening of the isolated nuclei at large extensions was observed to be associated with lamin A,C as lamin A,C knockdown did not significantly change nuclear stiffness at small extensions while depletion of lamin A,C decreased nuclear stiffness at large extensions leading to a linear force-displacement response (without strain stiffening). In another nucleus micromanipulation experimental study, however, single isolated nuclei showed no strain stiffening even at large extensions[16]. Lamin B1 network was also observed to stiffen in tension[17]. The strain stiffening of the lamin network (including both A-type and B-type) is perhaps consistent with its fibrous nature as observed in the lamina of the mammalian cell nuclei[5].

We model the nuclear envelope as a filamentous network material (lamin network) which stiffens with tension. Regardless of the fact that whether lamin network shows strain stiffening or not[6,16],

this model enables us to capture actomyosin contractility mediated increases in lamin A,C levels as recent growing evidence suggest that actomyosin contractility regulates lamin A,C levels and subsequently stiffening of the nuclear envelope lamina network. As shown in Figure S19, using the following proposed model for the nuclear envelope, we can capture the feedback between matrix stiffness, contractility, cytoskeletal stiffness, and nuclear lamina stiffness.

To this end, the stress $\hat{\sigma}_{ij}$ transmitted from the cytoskeleton to the nuclear envelope is first decomposed as follows*

$$\hat{\sigma}_{ij} = \hat{\sigma}_{ij}^{(\mathrm{I})} + \hat{\sigma}_{ij}^{(\mathrm{F})} \tag{S3.1}$$

where $\hat{\boldsymbol{\sigma}}^{(\mathrm{I})}$ is linearly related to the strain of nuclear envelope $\hat{\boldsymbol{\varepsilon}}$ using the initial stiffness of the nuclear envelope, $\hat{\mathbf{C}}^{(\mathrm{I})}$,

$$\hat{\sigma}_{ij}^{(\mathrm{I})} = \hat{\mathrm{C}}_{ijkl}^{(\mathrm{I})}\, \hat{\varepsilon}_{kl} \tag{S3.2}$$

while $\hat{\boldsymbol{\sigma}}^{(\mathrm{F})}$ is a nonlinear function of the strain tensor $\hat{\boldsymbol{\varepsilon}}$ in an orientation dependent manner

$$\hat{\boldsymbol{\sigma}}^{(\mathrm{F})} = \sum_{i=1}^{3} \frac{\partial \hat{f}(\hat{\varepsilon}_i)}{\partial \hat{\varepsilon}_i} \hat{\boldsymbol{n}}_i \otimes \hat{\boldsymbol{n}}_i = \sum_{i=1}^{3} \hat{\sigma}^{(\mathrm{F})}(\hat{\varepsilon}_i)\, \hat{\mathbf{E}}_i = \sum_{i=1}^{3} \hat{\sigma}_i^{(\mathrm{F})}\, \hat{\mathbf{E}}_i \tag{S3.3}$$

where the orthogonal eigenvectors $\hat{\boldsymbol{n}}_1$, $\hat{\boldsymbol{n}}_2$, and $\hat{\boldsymbol{n}}_3$ are respectively the unit vectors in the directions of the principal strains $\hat{\varepsilon}_1$, $\hat{\varepsilon}_2$, and $\hat{\varepsilon}_3$ and the symmetric tensors $\hat{\mathbf{E}}_1 = \hat{\boldsymbol{n}}_1 \otimes \hat{\boldsymbol{n}}_1$, $\hat{\mathbf{E}}_2 = \hat{\boldsymbol{n}}_2 \otimes \hat{\boldsymbol{n}}_2$, and $\hat{\mathbf{E}}_3 = \hat{\boldsymbol{n}}_3 \otimes \hat{\boldsymbol{n}}_3$ are the eigenprojections of $\hat{\boldsymbol{\varepsilon}}$. In equation (S3.3), $\otimes$ represents the dyadic product of two arbitrary vectors $\boldsymbol{u}$ and $\boldsymbol{v}$ as $(\boldsymbol{u} \otimes \boldsymbol{v})_{ij} = u_i v_j$. As shown in (S3.3), $\hat{\boldsymbol{\sigma}}^{(\mathrm{F})}$ is defined as a function of its principal stresses ($\hat{\sigma}_1^{(\mathrm{F})}$, $\hat{\sigma}_2^{(\mathrm{F})}$, $\hat{\sigma}_3^{(\mathrm{F})}$) and eigenprojections ($\hat{\mathbf{E}}_1$, $\hat{\mathbf{E}}_2$, $\hat{\mathbf{E}}_3$). The eigenprojections can be determined from the following spectral decomposition of the strain tensor $\hat{\boldsymbol{\varepsilon}}$

$$\hat{\boldsymbol{\varepsilon}} = \sum_{i=1}^{3} \hat{\varepsilon}_i\, \hat{\boldsymbol{n}}_i \otimes \hat{\boldsymbol{n}}_i = \sum_{i=1}^{3} \hat{\varepsilon}_i\, \hat{\mathbf{E}}_i \tag{S3.4}$$

To define the principal stresses, we here use equation (S2.15)

* All tensors, vectors, and scalars used in the nuclear envelope model are denoted by "^".

$$\hat{\sigma}_i^{(\mathrm{F})} = \frac{\partial \hat{f}(\hat{\varepsilon}_i)}{\partial \hat{\varepsilon}_i} = \tag{S3.5}$$

$$\begin{cases} 0 & \hat{\varepsilon}_i < \hat{\epsilon}_1 \\ \hat{\ell}\left[\dfrac{\left(\dfrac{\hat{\varepsilon}_i - \hat{\epsilon}_1}{\hat{\epsilon}_2 - \hat{\epsilon}_1}\right)^{\hat{n}} (\hat{\varepsilon}_i - \hat{\epsilon}_1)^2}{(\hat{n}+1)(\hat{n}+2)}\right] & \hat{\epsilon}_1 \le \hat{\varepsilon}_i < \hat{\epsilon}_2 \\ \hat{\ell}\left[\dfrac{(1+\hat{\varepsilon}_i - \hat{\epsilon}_2)^{\hat{m}+2} - 1}{(\hat{m}+1)(\hat{m}+2)} + \dfrac{\hat{\epsilon}_2 - \hat{\varepsilon}_i}{\hat{m}+1} + \dfrac{(\hat{\varepsilon}_i - \hat{\epsilon}_2)(\hat{\epsilon}_2 - \hat{\epsilon}_1)}{\hat{n}+1} + \dfrac{(\hat{\epsilon}_2 - \hat{\epsilon}_1)^2}{(\hat{n}+1)(\hat{n}+2)}\right] & \hat{\varepsilon}_i \ge \hat{\epsilon}_2 \end{cases}$$

where the principal stresses ($\hat{\sigma}_1^{(\mathrm{F})}$, $\hat{\sigma}_2^{(\mathrm{F})}$, $\hat{\sigma}_3^{(\mathrm{F})}$) are defined as functions of the principal strains ($\hat{\varepsilon}_1$, $\hat{\varepsilon}_2$, $\hat{\varepsilon}_3$) obtained from equations (S3.4). Similar to equation (S2.15), $\hat{\epsilon}_1 = \hat{\epsilon}_{\mathrm{c}} - 0.5\hat{\epsilon}_{\mathrm{t}}$ and $\hat{\epsilon}_2 = \hat{\epsilon}_{\mathrm{c}} + 0.5\hat{\epsilon}_{\mathrm{t}}$ are the transition points, $\hat{\epsilon}_{\mathrm{t}} = 0.25\hat{\epsilon}_{\mathrm{c}}$ is the transition width, $\hat{\epsilon}_{\mathrm{c}}$ is the critical (tensile) principal strain, and $\hat{n}$ is the transition constant. In (S3.5), $\hat{\ell}$ and $\hat{m}$ are the stiffening parameters which regulate strain stiffening of the lamin network in our model. Note that we can simulate lamin A,C knockout by assuming $\hat{\ell} \approx 0$. The energy function $\hat{f}(\hat{\varepsilon}_i)$ in equation (S3.5) is chosen such that the principal stress $\hat{\sigma}_i^{(\mathrm{F})}$ vanishes below a critical value of tensile strain. Therefore, for small extensions $\hat{\varepsilon}_i < \hat{\epsilon}_1$, the strain stiffening term $\widehat{\sigma}_{ij}^{(\mathrm{F})}$ in equation (S3.1) vanishes (i.e., $\widehat{\sigma}_{ij} = \widehat{\sigma}_{ij}^{(\mathrm{I})}$) consistent with the experimental results shown in Figure S35B where single isolated nuclei do not exhibit strain stiffening at small extensions. Note that the initial isotropic term $\widehat{\sigma}_{ij}^{(\mathrm{I})}$, obtained from equation (S3.2), is negligible as the lamin network is assumed to be initially (under no tension) soft

$$\widehat{\mathsf{C}}_{ijkl}^{(\mathrm{I})} = \hat{K}^{(\mathrm{I})}\delta_{ij}\delta_{kl} + \hat{\mu}^{(\mathrm{I})}\left(\delta_{ik}\delta_{jk} + \delta_{il}\delta_{jk} - \frac{2}{3}\delta_{ij}\delta_{kl}\right) \tag{S3.6}$$

where $\hat{K}^{(\mathrm{I})}$ and $\hat{\mu}^{(\mathrm{I})}$ are the initial bulk and shear moduli of the lamin network, respectively. However, at large extensions, the total stiffness of the lamin network

$$\widehat{\mathsf{C}}_{ijkl} = \widehat{\mathsf{C}}_{ijkl}^{(\mathrm{I})} + \widehat{\mathsf{C}}_{ijkl}^{(\mathrm{F})} \tag{S3.7}$$

is dominated by the strain-stiffening term $\widehat{\mathsf{C}}_{ijkl}^{(\mathrm{F})}$ which can be determined as follows (using a piecewise linear approximation)

$$\widehat{\mathbb{C}}_{ijkl}^{(\mathrm{F})} = \frac{\mathrm{d}\hat{\sigma}_{ij}^{(\mathrm{F})}}{\mathrm{d}\hat{\varepsilon}_{kl}} \tag{S3.8}$$

Similar to (S2.16), the exact expression for $\widehat{\mathbb{C}}_{ijkl}^{(\mathrm{F})}$ can be determined from (S2.19-25) by replacing $\sigma_i^{(\mathrm{F})}$, $\varepsilon_i^{(\mathrm{Y})}$, $\mathbf{E}_i$, and $\boldsymbol{\varepsilon}^{(\mathrm{Y})}$ with $\hat{\sigma}_i^{(\mathrm{F})}$, $\hat{\varepsilon}_i$, $\hat{\mathbf{E}}_i$, and $\hat{\boldsymbol{\varepsilon}}$, respectively ($i = 1, 2, 3$).

3.2. Chromatin:

Recent biophysical experiments show that the stiffness of isolated nuclei depends on both nuclear envelope lamina network and nuclear interior[6]. Uniaxial stretching of single isolated nuclei in Figure S35 shows that chromatin governs nuclear response to small extensions. Furthermore, unlike the lamin network, chromatin does not exhibit strain stiffening at large extensions[6]. Therefore, the stiffness of chromatin in our model is defined as follows[†]

$$\bar{\mathbb{C}}_{ijkl} = \bar{K}\delta_{ij}\delta_{kl} + \bar{\mu}\left(\delta_{ik}\delta_{jk} + \delta_{il}\delta_{jk} - \frac{2}{3}\delta_{ij}\delta_{kl}\right) \tag{S3.9a}$$

with

$$\bar{K} = \frac{\bar{E}}{3(1-2\bar{v})} \quad , \quad \bar{\mu} = \frac{\bar{E}}{2(1+\bar{v})} \tag{S3.9b}$$

where $\bar{K}$, $\bar{\mu}$, $\bar{E}$, and $\bar{v}$ are respectively the bulk modulus, shear modulus, elastic modulus, and Poisson's ratio of chromatin in our model.

Note that chromatin stiffness, and subsequently nuclear stiffness, can change by chromatin condensation/decondensation. Using an optical tweezer, we have previously shown that chromatin decondensation (induced by enzymatic cleavage of histone tails using trypsin) in single isolated nuclei leads to nuclear softening[18]. On the other hand, micropatterning of NIH 3T3 mouse fibroblast cells on fibronectin-coated substrates with different substrate areas, we observe chromatin condensation in cells cultured on smaller substrate areas (but the same substrate geometry). The condensation of chromatin in these experiments is observed to be concomitant with decreases in actomyosin contractility which in turn leads to cytoplasmic to nuclear shuttling of HDAC3. To further assess the link between actomyosin contractility and HDAC translocations,

[†] All tensors, vectors, and scalars used in the chromatin model are denoted by "-".

micropatterned fibroblast cells were treated with Cytochalasin-D (inhibitor of actin polymerization)[19], Latrunculin-A (inhibitor of actin polymerization)[19], Blebbistatin (inhibitor of myosin motor II)[19], and Y-27632 (inhibitor of Rho-associated protein kinase II)[20]. In all cases, we observe cytoplasmic to nuclear translocation of HDAC3 and subsequently chromatin condensation upon treatment with the inhibitors of actomyosin contractility.

These changes in chromatin stiffness, and subsequently nuclear stiffness, due to chromatin condensation/decondensation is accounted for by adjusting the chromatin elastic modulus as $\bar{E}$ increases (decreases) with chromatin condensation (decondensation) in our model. In SI Section 4, we determine the nuclear level of HDAC3 as a function of the mean contractility $\frac{1}{3}\rho_{kk}$ and we show that the nuclear accumulation of HDAC3 increases with decreasing actomyosin contractility. Since nuclear accumulation of HDAC3 is observed to be correlated with chromatin condensation (chromatin stiffening), we assume that the chromatin elastic modulus $\bar{E}$ increases with HDAC3 nuclear level.

In addition to changes in nuclear stiffness, our experimental studies show that chromatin condensation/decondensation can lead to changes in nuclear volume. The chromatin decondensation of the isolated nuclei due to trypsin digestion is observed to be accompanied by swelling of the nuclei[18]. Furthermore, chromatin decondensation in TSA treated fibroblast cells on micropatterned substrates is accompanied by an increase in nuclear volume[19]. We also observe that inhibiting actomyosin contractility upon treating micropatterned fibroblasts with Cytochalasin-D, Latrunculin-A, Blebbistatin, and Y-27632 leads to decreases in nuclear volume[19,20]. These changes in nuclear volume are included in our model by adjusting the Poisson's ratio of chromatin $\bar{\nu}$ and the prestress parameter $\bar{\sigma}_0$

$$\bar{\sigma}_{ij} = \bar{\mathsf{C}}_{ijkl}\,\bar{\varepsilon}_{kl} - \bar{\sigma}_0\delta_{ij} = \frac{\bar{E}}{3(1-2\bar{\nu})}\delta_{ij}\bar{\varepsilon}_{kk} + \frac{\bar{E}}{(1+\bar{\nu})}\left(\bar{\varepsilon}_{ij} - \frac{1}{3}\delta_{ij}\bar{\varepsilon}_{kk}\right) - \bar{\sigma}_0\delta_{ij} \qquad \text{(S3.10)}$$

where $\bar{\boldsymbol{\sigma}}$ and $\bar{\boldsymbol{\varepsilon}}$ are the second order stress and strain tensors in the chromatin model, respectively. We assume an inverse relationship between $\bar{\nu}$ and HDAC3 nuclear level. As a result, fluid flows out of the nucleus and nuclear volume decreases with decreasing actomyosin contractility. Also, note that a positive value of $\bar{\sigma}_0$ in equation (S3.11) tends to expand the nucleus which can simulate the nuclear expansion of TSA treated micropatterned fibroblasts or nuclear expansion of isolated nuclei due to enzymatic cleavage of histone tails by trypsin.

3.3. Uniaxial stretching of single isolated nuclei:

As described above, we model the nucleus as an elastic thin layer filled with a solid material. The elastic thin layer represents the nuclear envelope and is modeled as a fibrous material which stiffens under tension. The solid material represents chromatin which is modeled as a linear elastic material as reported in[6]. Using uniaxial stretching simulations of isolated nuclei, we here study the nuclear mechanical response to tension. As shown in Figure S35A, the nucleus is fixed at its one end and is stretched at the other end. Recent experimental studies[6] show strain stiffening of isolated nuclei at large extensions. The strain stiffening was reported to be associated with lamin A,C as (i) depletion of lamin A,C decreased nuclear stiffness only at large extensions, (ii) no strain stiffening was observed upon lamin A,C knockdown, and (iii) chromatin digestion decreased nuclear stiffness only at small extensions. Figure S35B depicts the nuclear response to uniaxial tension from both experiment and simulation. For small extensions, isolated nuclei exhibit a linear force-displacement response as chromatin governs nuclear response to small extensions. However, for large extensions, isolated nuclei display a strain stiffening response which is dominated by the nuclear envelope. Although our model can capture the strain-stiffening behavior of isolated nuclei in[6], it should be noted that the main goal of the proposed model is to develop an actomyosin contractility dependent link between matrix stiffness, cell substrate geometry, and nuclear lamina stiffness. As reported in[9], increases in actomyosin contractility of mesenchymal stem cells with substrate stiffness generate higher nuclear tension which in turn lead to higher levels of lamin A,C and subsequently nuclear stiffening. In agreement with[9], we observed that higher actomyosin contractility in large and elongated cells (compared to small and isotropic cells) correlates with higher levels of lamin A,C in fibroblasts. The nuclear lamina stiffening observed in[9] and our experiments can be captured in our model as the nuclear envelope stiffens with increased tension in the nuclear envelope resulting from increases in myosin II contractility.

4. Contractility dependent nucleo-cytoplasmic shuttling of transcription and epigenetic factors

To investigate the relationship between actomyosin contractility and nucleo-cytoplasmic shuttling of transcription and epigenetic factors, we first study how geometric constraints affect actomyosin contractility in fibroblasts. We use various geometric constraints in our study to constrain (i) cell polarization, and/or (ii) cell spreading. The rectangular micropatterned substrate with a surface area of 1600 μm^2 and aspect ratio of 1:5 approximately represents the spreading area and aspect ratio of fibroblasts on stiff un-patterned substrates[21]. Therefore, fibroblasts on the rectangular micropatterned substrate are considered as normal cells and are compared with geometrically constrained cells.

4.1. Mathematical modeling:

First, we study the effect of cell polarization constraints on the level of actomyosin contractility. To this end, we culture fibroblasts on micropatterned substrates with the same surface area of 1600 μm^2 but unpolarized geometries including circular, square, and triangular geometries. Our simulations show that constraining fibroblasts on these unpolarized geometries reduces the average level of contractility $\frac{1}{3}\rho_{kk} = (\rho_{11} + \rho_{22} + \rho_{33})/3$. This is consistent with our experimental results where we observe lower levels of phosphorylated myosin light chain (p-MLC) which is a well-known marker for myosin II contractility. Our simulations also show that the circular, square, and triangular cells have lower cytoskeletal stiffness compared to the rectangular cell. This is in agreement with our experiments which show lower levels of F-actin as shown in Figure 5B.

Next, we study how spreading constraints affect the level of actomyosin contractility. To this end, we culture fibroblasts on triangular micropatterned substrates with surface areas ranging from 1600 to 500 μm^2. Similar to the polarization constraints, our simulations show that constraining fibroblasts on small substrate areas reduces the average level of contractility and cytoskeletal stiffness in agreement with our experiments (Figure 5B). However, we find that the reduction in the level of actomyosin contractility due to the spreading constraints is significantly more pronounced than the polarization constraints. This is shown in Figure 5B where we observe about a two-fold decrease in the F-actin level as substrate area decreases from 1600 to 500 μm^2.

Next, we show that the reduction in the level of actomyosin contractility due to the spreading constraints causes nucleo-cytoplasmic shuttling of transcription and epigenetic factors. Figure 5C shows that MKL nuclear level decreases with decreasing $\frac{1}{3}\rho_{kk}$. In fact, as $\frac{1}{3}\rho_{kk}$ decreases, more F-actin is depolymerized into G-actin in the cytoplasm. Since MKL binds to G-actin in the cytoplasm, MKL is expected to be more concentrated in the cytoplasm of smaller cells where there is more G-actin. As G-actin is polymerized into F-actin with increasing $\frac{1}{3}\rho_{kk}$, MKL unbinds from G-actin and shuttles to the nucleus leading to increases in MKL nuclear levels of larger cells. We also study shuttling of HDAC3 and we show that the significant reduction in the level of actomyosin contractility (due to the spreading constraints) causes higher nuclear accumulation of HDAC3 in smaller cells (Figure 5D) which in turn leads to chromatin condensation and reduction of nuclear volume.

4.2. Actin polymerization:

We assume that polymerization of G-actin into F-actin (and also depolymerization of F-actin into G-actin) in the cytoplasm can be described as follows[22]

$$\frac{\mathrm{d}N_{\mathrm{F}}^{(\mathrm{c})}}{\mathrm{dt}} = K_{\mathrm{G}\leftrightarrow\mathrm{F}}^{\mathrm{on}}\, N_{\mathrm{F}}^{(\mathrm{c})}\, N_{\mathrm{G}}^{(\mathrm{c})} - K_{\mathrm{G}\leftrightarrow\mathrm{F}}^{\mathrm{off}}\, N_{\mathrm{F}}^{(\mathrm{c})} \tag{S4.1}$$

$$\frac{\mathrm{d}N_{\mathrm{G}}^{(\mathrm{c})}}{\mathrm{dt}} = -K_{\mathrm{G}\leftrightarrow\mathrm{F}}^{\mathrm{on}}\, N_{\mathrm{F}}^{(\mathrm{c})}\, N_{\mathrm{G}}^{(\mathrm{c})} + K_{\mathrm{G}\leftrightarrow\mathrm{F}}^{\mathrm{off}}\, N_{\mathrm{F}}^{(\mathrm{c})} \tag{S4.2}$$

where $N_{\mathrm{F}}^{(\mathrm{c})}$, $N_{\mathrm{G}}^{(\mathrm{c})}$, $K_{\mathrm{G}\leftrightarrow\mathrm{F}}^{\mathrm{on}}$, and $K_{\mathrm{G}\leftrightarrow\mathrm{F}}^{\mathrm{off}}$ are the F-actin concentration, the G-actin concentration, the rate of actin polymerization, and the rate of actin depolymerization in the cytoplasm, respectively. In the steady state condition ($\frac{\mathrm{d}N_{\mathrm{F}}^{(\mathrm{c})}}{\mathrm{dt}} = \frac{\mathrm{d}N_{\mathrm{G}}^{(\mathrm{c})}}{\mathrm{dt}} = 0$), we have

$$N_{\mathrm{F}}^{(\mathrm{c})} = N_{\mathrm{Total}}^{(\mathrm{c})} - \frac{K_{\mathrm{G}\leftrightarrow\mathrm{F}}^{\mathrm{off}}}{K_{\mathrm{G}\leftrightarrow\mathrm{F}}^{\mathrm{on}}} \tag{S4.3}$$

where

$$N_{\mathrm{Total}}^{(\mathrm{c})} = N_{\mathrm{F}}^{(\mathrm{c})} + N_{\mathrm{G}}^{(\mathrm{c})} \tag{S4.4}$$

is the total concentration of actin in the cytoplasm. Our experiments show that polymerization of G-actin into F-actin increases with cell contractility. Therefore, we assume that the rate of actin polymerization $K_{\mathrm{G}\leftrightarrow\mathrm{F}}^{\mathrm{on}}$ increases with the average level of contractility $\sum\frac{1}{3}\rho_{kk} = \sum(\rho_{11} + \rho_{22} + \rho_{33})/3$ as follows

$$K_{\mathrm{G}\leftrightarrow\mathrm{F}}^{\mathrm{on}} = K_{\mathrm{G}\leftrightarrow\mathrm{F}}^{\mathrm{initial}} + K_{\mathrm{G}\leftrightarrow\mathrm{F}}^{\mathrm{contractility}}\left(\sum\frac{1}{3}\rho_{kk}\right) \tag{S4.5}$$

where $K_{\mathrm{G}\leftrightarrow\mathrm{F}}^{\mathrm{initial}}$ is the contractility independent rate of actin polymerization, and $K_{\mathrm{G}\leftrightarrow\mathrm{F}}^{\mathrm{contractility}}$ is the contractility dependent rate of actin polymerization in our model. Note that $\sum$ denotes the average over the cytoskeleton volume; first $(\rho_{11} + \rho_{22} + \rho_{33})/3$ is calculated for each point in the cytoskeleton and then $\sum\frac{1}{3}\rho_{kk}$ is determined as the average of all points. With $\sum\frac{1}{3}\rho_{kk}$ at hand from our mechanical simulations for different substrate geometries, we fit equation (S4.3) into our experimental data to approximate $K_{\mathrm{G}\leftrightarrow\mathrm{F}}^{\mathrm{on}}$, $K_{\mathrm{G}\leftrightarrow\mathrm{F}}^{\mathrm{off}}$, and $N_{\mathrm{Total}}^{(\mathrm{c})}$. To this end, we use experimental data of F-actin concentration ($N_{\mathrm{F}}^{(\mathrm{c})}$) for triangular cells with surface areas of 500, 750, 1000, 1250, and 1600 μm^2. After training the model on the triangular geometries, we then test the model predictions for the following geometries: circular substrate (500 μm^2), square substrate (1600 μm^2), and rectangular substrate (1600 μm^2). Finally, we plot all data in Figure 5B.

4.3. MKL translocation:

We simply model MKL transport as follows

$$\frac{\mathrm{d}N_{\mathrm{M}}^{(\mathrm{n})}}{\mathrm{d}t} = -K_{\mathrm{M}}^{(\mathrm{n})\to(\mathrm{c})}N_{\mathrm{M}}^{(\mathrm{n})} + K_{\mathrm{M}}^{(\mathrm{c})\to(\mathrm{n})}N_{\mathrm{M}}^{(\mathrm{c})} \tag{S4.6}$$

where $N_{\mathrm{M}}^{(\mathrm{n})}$, $N_{\mathrm{M}}^{(\mathrm{c})}$, $K_{\mathrm{M}}^{(\mathrm{n})\to(\mathrm{c})}$, and $K_{\mathrm{M}}^{(\mathrm{c})\to(\mathrm{n})}$ are the nuclear concentration of MKL, the cytoplasmic concentration of MKL, the rate of nucleus to cytoplasm transport of MKL, and the rate of cytoplasm to nucleus transport of MKL, respectively. Note that additional terms can be also added to equation (S4.6), since MKL binds to G-actin and unbinds from G-actin by decreasing and increasing contractility, respectively. However, we use the simplest form of MKL transport in equation (S4.6) to minimize the number of fitting parameters. In the steady state condition $\frac{\mathrm{d}N_{\mathrm{M}}^{(\mathrm{n})}}{\mathrm{d}t} = 0$, we have

$$\frac{N_{\mathrm{M}}^{(\mathrm{n})}}{N_{\mathrm{M}}^{(\mathrm{c})}} = \frac{K_{\mathrm{M}}^{(\mathrm{c})\to(\mathrm{n})}}{K_{\mathrm{M}}^{(\mathrm{n})\to(\mathrm{c})}} \tag{S4.7}$$

Since MKL unbinds from G-actin and shuttles to the nucleus with actin polymerization, we assume that the rate of cytoplasm to nucleus transport of MKL increases with the average level of contractility as follows

$$K_{\mathrm{M}}^{(\mathrm{c})\to(\mathrm{n})} = K_{\mathrm{M}}^{\mathrm{initial}} + K_{\mathrm{M}}^{\mathrm{contractility}} \left(\sum \frac{1}{3} \rho_{kk} \right) \tag{S4.8}$$

where $K_{\mathrm{M}}^{\mathrm{initial}}$ is the contractility independent rate of cytoplasm to nucleus transport of MKL, and $K_{\mathrm{M}}^{\mathrm{contractility}}$ is the contractility dependent rate of cytoplasm to nucleus transport of MKL. With $\sum \frac{1}{3} \rho_{kk}$ at hand from our mechanical simulations, we fit equation (S4.7) into our experimental data for the nuclear to cytoplasmic ratio of MKL to approximate $K_{\mathrm{M}}^{(\mathrm{c})\to(\mathrm{n})}$ and $K_{\mathrm{M}}^{(\mathrm{n})\to(\mathrm{c})}$.

4.4. HDAC translocation:

To model actomyosin dependent shuttling of HDAC, we assume the following transport equation

$$\frac{\mathrm{d}N_{\mathrm{H}}^{(\mathrm{c})}}{\mathrm{dt}} = K_{\mathrm{H}}^{(\mathrm{n})\to(\mathrm{c})} N_{\mathrm{H}}^{(\mathrm{n})} - K_{\mathrm{H}}^{(\mathrm{c})\to(\mathrm{n})} N_{\mathrm{H}}^{(\mathrm{c})} \tag{S4.9}$$

where $N_{\mathrm{H}}^{(\mathrm{n})}$, $N_{\mathrm{H}}^{(\mathrm{c})}$, $K_{\mathrm{H}}^{(\mathrm{n})\to(\mathrm{c})}$, and $K_{\mathrm{H}}^{(\mathrm{c})\to(\mathrm{n})}$ are the nuclear concentration of HDAC, the cytoplasmic concentration of HDAC, the rate of nucleus to cytoplasm transport of HDAC, and the rate of cytoplasm to nucleus transport of HDAC, respectively. In the steady state condition $\frac{\mathrm{d}N_{\mathrm{H}}^{(\mathrm{c})}}{\mathrm{dt}} = 0$, we have

$$\frac{N_{\mathrm{H}}^{(\mathrm{n})}}{N_{\mathrm{H}}^{\mathrm{Total}}} = \frac{K_{\mathrm{H}}^{(\mathrm{c})\to(\mathrm{n})}}{K_{\mathrm{H}}^{(\mathrm{c})\to(\mathrm{n})} + K_{\mathrm{H}}^{(\mathrm{n})\to(\mathrm{c})}} \tag{S4.10}$$

where

$$N_{\mathrm{H}}^{\mathrm{Total}} = N_{\mathrm{H}}^{(\mathrm{n})} + N_{\mathrm{H}}^{(\mathrm{c})} \tag{S4.11}$$

is the total concentration of HDAC. Since fibroblasts with higher levels of actomyosin contractility show lower nuclear accumulation of HDAC, we assume that the rate of nucleus to cytoplasm transport of HDAC increases with the average level of contractility in the following form

$$K_{\mathrm{H}}^{(\mathrm{n})\to(\mathrm{c})} = K_{\mathrm{H}}^{\mathrm{initial}} + K_{\mathrm{H}}^{\mathrm{contractility}} \left(\sum \frac{1}{3} \rho_{kk} \right)^2 \tag{S4.12}$$

where $K_{\mathrm{H}}^{\mathrm{initial}}$ is the contractility independent rate of nucleus to cytoplasm transport of HDAC, and $K_{\mathrm{H}}^{\mathrm{contractility}}$ is the contractility dependent rate of nucleus to cytoplasm transport of HDAC. Using $K_{\mathrm{H}}^{(\mathrm{n})\to(\mathrm{c})}$ in the form of equation (S4.12), we can fit (S4.10) into our experimental data for the nuclear to total ratio of HDAC to determine the fitting parameters of the model (training of the model).

We also simulate the translocation of HDAC upon treating fibroblasts with cytochalasin D (Figure 5E) and blebbistatin (Figure 5F). To simulate the disruption of the actomyosin network by these actomyosin inhibitors, we decrease the stiffness of the actin filament network $\mathrm{C}_{ij}^{(\mathrm{A})}$ (i.e., $\mathrm{C}_{ij}^{(\mathrm{A})} \approx 0$ when the actomyosin network is fully disrupted) in our simulations and we measure $\sum \frac{1}{3} \rho_{kk}$. The change in the average level of contractility $\sum \frac{1}{3} \rho_{kk}$ from the control case ($\mathrm{C}_{ij}^{(\mathrm{A})} \neq 0$) to the actomyosin disrupted case ($\mathrm{C}_{ij}^{(\mathrm{A})} \approx 0$) is measured and divided into several steps while we assume that the first ($\mathrm{C}_{ij}^{(\mathrm{A})} \neq 0$) and the last ($\mathrm{C}_{ij}^{(\mathrm{A})} \approx 0$) steps are respectively associated with the first and the last time increments in our experiments. With $\sum \frac{1}{3} \rho_{kk}$ at hand from our mechanical simulations at different steps (pseudo-time steps) and using the same parameters $K_{\mathrm{H}}^{\mathrm{initial}}$, $K_{\mathrm{H}}^{\mathrm{contractility}}$, and $K_{\mathrm{H}}^{(\mathrm{c})\to(\mathrm{n})}$ previously determined from the training of the model, equations (S4.10) yields the nuclear concentration of HDAC as shown in Figures 5E and 5F.

Finally, we simulate the translocation of HDAC in fibroblasts under compressive forces. With $\sum \frac{1}{3} \rho_{kk}$ at hand from our mechanical simulations (before and after compression) and using the same parameters $K_{\mathrm{H}}^{\mathrm{initial}}$, $K_{\mathrm{H}}^{\mathrm{contractility}}$, and $K_{\mathrm{H}}^{(\mathrm{c})\to(\mathrm{n})}$ previously determined from the training of the model, equations (S4.10) yields the nuclear concentration of HDAC as shown in Figure 5J.

5. Fourth order and second order stiffness tensors

All fourth order stiffness tensors introduced in the previous sections can be degraded to square matrices to be used in the finite element framework. For example, the fourth order stiffness tensor C_{ijkl} can be degraded to the second order stiffness tensor C_{ij} as follows

$$\mathsf{C}_{ij} = \begin{bmatrix} \mathsf{C}_{1111} & \mathsf{C}_{1122} & \mathsf{C}_{1133} & \mathsf{C}_{1112} & \mathsf{C}_{1113} & \mathsf{C}_{1123} \\ \mathsf{C}_{2211} & \mathsf{C}_{2222} & \mathsf{C}_{2233} & \mathsf{C}_{2212} & \mathsf{C}_{2213} & \mathsf{C}_{2223} \\ \mathsf{C}_{3311} & \mathsf{C}_{3322} & \mathsf{C}_{3333} & \mathsf{C}_{3312} & \mathsf{C}_{3313} & \mathsf{C}_{3323} \\ \mathsf{C}_{1211} & \mathsf{C}_{1222} & \mathsf{C}_{1233} & \mathsf{C}_{1212} & \mathsf{C}_{1213} & \mathsf{C}_{1223} \\ \mathsf{C}_{1311} & \mathsf{C}_{1322} & \mathsf{C}_{1333} & \mathsf{C}_{1312} & \mathsf{C}_{1313} & \mathsf{C}_{1323} \\ \mathsf{C}_{2311} & \mathsf{C}_{2322} & \mathsf{C}_{2333} & \mathsf{C}_{2312} & \mathsf{C}_{2313} & \mathsf{C}_{2323} \end{bmatrix} \tag{S5.1}$$

6. Stability criterion

Biological systems use feedback controls in many ways ranging from molecules and cells to organs [23]. The actomyosin model presented in SI Sections 1 and 2 includes a feedback loop between actomyosin contractility and tension in the actin filament network (see Figure S6). However, it is known from feedback control theory that large values of feedback gain parameters can lead to instability of the system [24]. Below, we study the stability of the feedback loop in our model.

6.1. One-dimensional cell model

Equation (S1.2) shows that for $\beta = \alpha$, the cell contractility ρ becomes infinity which is not physically possible. Considering $E^{(\mathrm{MT})} > 0$ (the elastic modulus of the microtubule network cannot be negative) and $\varepsilon^{(\mathrm{X})} \leq 0$ (the length of the cell reduces as it contracts and pulls on the extracellular matrix), the two coefficients of $\frac{E^{(\mathrm{MT})}\,\alpha-1}{\beta-\alpha}$ and $\frac{\beta}{\beta-\alpha}$ in equation (S1.2) should be positive to ensure that the cell contractility ρ is positive (actomyosin contractility pulls on, and not pushes, the extracellular matrix), which gives the following stability criterion

$$\beta > \alpha > \frac{1}{E^{(\mathrm{MT})}}$$

6.2. Three-dimensional cell model

Similar to the one-dimensional model, the parameters $K^{(\rho)}$, $\mu^{(\rho)}$, and $\bar{\rho}_0$ in our three-dimensional model should be all positive which yields the following stability criterion

$$\beta_{\mathrm{v}} > \alpha_{\mathrm{v}} > \frac{1}{3K^{(\mathrm{MT})}}$$

$$\beta_{\mathrm{d}} > \alpha_{\mathrm{d}} > \frac{1}{2\mu^{(\mathrm{MT})}}$$

The feedback parameters in our simulations have been chosen according to the above criterion to ensure that the feedback gain does not lead to instabilities.

7. Intermediate filaments

As shown in Figures 1A and 1C, the cytoskeletal model is composed of three elements: myosin motors, the actin filament network, and the microtubule network. However, in animal cells, these cytoskeletal components are accompanied by intermediate filaments which have been shown to play an important mechanical role in cell integrity particularly at large deformations[25–29]. The characteristic properties of intermediate filaments that enable them to undergo large deformations[30] have been elucidated by multi-scale modeling of these filaments[31–33].

In addition to their ability to withstand large mechanical deformations, intermediate filaments may also laterally reinforce microtubules under physiological compressive forces which in turn significantly increases the compressive forces that microtubules can withstand[1,34]. When cytoplasmic microtubules are compressively loaded by the internally generated actomyosin contractile forces, they buckle with short wavelengths[1]. However, in contrast to microtubules in living cells, isolated microtubules buckle with higher wavelengths[1] which indicates that cytoplasmic microtubules are more resistant to compression compared to isolated microtubules from *in vitro* measurements[28]. The higher resistance of cytoplasmic microtubules against compression has been attributed to the mechanical coupling of microtubules to their surrounding network of cytoskeletal intermediate filaments and actin microfilaments[1,28,34]. As discussed in references[1,34], the surrounding network of cytoskeletal filaments acts as a lateral constraint that, by reinforcing microtubules, enables them to sustain higher compressive forces and buckle with shorter wavelengths.

In addition to reinforcing cytoplasmic microtubules, intermediate filaments have been also shown to have a considerable contribution to cytoplasmic stiffness[35–41]. Keratins are types I and II intermediate filaments which are expressed in endothelial cells and have been shown to have a major contribution to cell stiffness[42]. Similarly, vimentin is a type III intermediate filament that is expressed in mesenchymal cells like fibroblasts[43] and it has been reported that vimentin-deficient fibroblasts have softer intracellular cytoskeletal networks compared to wild type cells[44,45]. Vimentin intermediate filaments are also known to form a juxtanuclear cage and it has been recently shown that loss of vimentin decreases perinuclear stiffness[40]. Similarly, we model intermediate filaments as a cage-like network around the nucleus which contributes to perinuclear stiffness as shown in Figure S36.

Our simulations show that the vimentin perinuclear cage contributes to cytoskeletal stiffness and more importantly protects the nucleus from excessive deformations under external forces (Figure S37). This is consistent with experimental observations in reference[40] where vimentin intermediate filaments are found to protect the nucleus by limiting nuclear deformation during 3D migration through small pores. As a result, loss of vimentin in fibroblasts migrating through small pores is shown to increase the number of nuclei with blebs and DNA damage[40]. Furthermore, applying large compressive strains to tissues, containing fibroblasts cultured within 3D collagen matrices, it was shown that necrosis in vimentin-deficient cells is significantly higher than their wild-type counterparts[40]. This may indicate that vimentin provides mechanical resistance against compression which is consistent with our simulations in Figure S37.

Although all the above studies indicate that cell with intermediate filament knocked out are softer compared to their wild-type counterparts, the effects of intermediate filament depletion on actomyosin contractility are still not clear[46]. As early as 1998, Eckes et al. cultured mouse embryonic fibroblasts with two densities of 25 and 50 cells/µl within three-dimensional type I collagen matrices and measured the collagen gel diameters at different times to test the ability of both vimentin-deficient and wild type cells to freely contract collagen matrices[39]. Using this collagen gel compaction assay, they found that vimentin-deficient fibroblasts were significantly less contractile than their wild type counterparts[39] consistent with a recent study where vimentin knockout mouse embryonic fibroblasts cultured on collagen-coated acrylamide gels with an elastic modulus of 2.4 kPa were shown to generate less contractile traction forces[45]. Mendez et al. also found that vimentin-null mouse embryonic fibroblasts are less contractile within three-dimensional type I collagen matrices when cell density is low (50 cells/µl)[37]. However, they showed that vimentin-null cells become more contractile than their wild type counterparts when cell density increases from 50 to 700 cells/µl[37]. Culturing osteosarcoma cells and human dermal fibroblasts on fibronectin-coated polyacrylamide gels with elastic moduli of 25 and 33 kPa, it was shown that vimentin depletion in both cell types induces phosphorylation of the microtubule-associated GEF-H1 which is a RhoA-specific guanine nucleotide exchange factor[47]. As a result, RhoA activity increases which in turn leads to higher contractility, more assembly of actin stress fibers, and higher cell-generated contractile traction forces in vimentin knockout cells compared to their wild type counterparts[47]. Similarly, vimentin knockout mouse embryonic fibroblasts cultured on stiff substrates were found to generate significantly higher traction forces compared to their wild type

counterparts while no remarkable changes were found in stress fiber organizations and focal adhesion sizes between vimentin knockout and wild type cells[48]. Furthermore, culturing vimentin null and wild type mouse embryonic fibroblasts on different micropatterned substrates, it was observed that the actin filaments network and focal adhesion complexes were not altered by the absence of vimentin[49]. In agreement with reference[48], it was reported that in the absence of vimentin, actomyosin-driven contractile forces are wholly transmitted to the substrate, while in the presence of vimentin part of these contractile forces are absorbed by the vimentin network indicating that the vimentin intermediate filaments network acts as a load-bearing structure[50].

In addition to the effects of intermediate filaments on cytoplasmic stiffness and actomyosin contractility, intermediate filaments may also change the physical properties of the nucleus including nuclear morphology and deformability. Applying local pulling forces on the nuclear membrane of living adherent fibroblasts with a micropipette, Neelam et al. found that the vimentin intermediate filament network maintains nuclear morphology against localized forces[51]. After transfecting NIH 3T3 fibroblasts with siRNA that decreases vimentin expression, they observed that the nucleus translated and stretched more under the local pulling force compared to the control cells[51]. This indicates that the intermediate filament network resists nuclear motion and deformation[51]. In agreement to this study, disruption of the keratin intermediate filament network in micropatterned keratinocytes through the loss of plectin was shown to increase nuclear deformation[52]. Plectin is a cyto-linker that not only links intermediate filaments to the nuclear membrane but also crosslinks intermediate filaments together and links them to actin filaments[52]. It was reported that plectin knockout cells exhibited reduced keratin filament densities around the nucleus and subsequently showed higher nuclear deformations under actomyosin-driven forces[52]. Thus, it was concluded that pectin plays an important role in the regulation of nuclear morphology and protects the nucleus from deformation[52]. This is consistent with experimental observations by Versaevel et al where disruption of intermediate filaments upon acrylamide or calyculin A treatment (in primary human umbilical vein endothelial cells cultured on 1600 μm^2 elongated micropatterned substrates with a width to length ratio of 0.26) was observed to increase nuclear deformation and subsequently nuclear elongation[53].

In contrast, experimental observations by Sarria et al., as early as 1994, may suggest another possible mechanism for the role of intermediate filaments on nuclear morphology. They found that human SW-13 clone cells that do not synthesize vimentin had nuclei with large folds or

invaginations, while their wild type counterparts exhibited regular and smooth nuclear shapes[54]. This may indicate that the nuclear envelopes of vimentin-deficient cells experience lower tension compared to their wild type counterparts. It has been recently reported that in lobopodia-based migration of fibroblasts within 3D cell-derived matrices (DCMs), vimentin intermediate filaments are involved in the transition of actomyosin generated tension to the nucleus through nesprin-3[55] which is a member of the LINC (linker of nucleoskeleton and cytoskeleton) complex that links the nuclear envelope to intermediate filaments through plectin[56]. Therefore, disruption of intermediate filaments may reduce the transmission of tension to the nucleus which can, in turn, lead to increases in nuclear height, nuclear roundness, and invagination of the nucleus. This is consistent with a recent study where fibroblasts without vimentin have rounder, more folded and less smooth nuclei compared to control cells[40]. Taken together, while intermediate filaments have been shown to contribute to cytoskeletal stiffness, the review of experimental work presented in this section indicates that further studies are required to elucidate the mechanisms through which intermediate filaments may affect actomyosin contractility and nuclear properties.

8. Discrete modeling of microtubules

To study how cell geometric constraints can induce microtubule associated nuclear invaginations, we model microtubules as discrete elastic filaments in Figures 3A, 3B, 3E and Figure S14. All microtubules are modeled as linear elastic structures emanating from the microtubule organizing center (MTOC). Figure S38 demonstrates the initial configuration of microtubules. All microtubules are tied together at one end (minus end) and subsequently have the same displacement at that end (MTOC displacement), while microtubule plus ends extend to the cell membrane[57]. Microtubules are modeled as truss elements[58] in our finite element simulations and are embedded within the cytoskeleton; the translational degrees of freedom of the embedded microtubule nodes are constrained to the values of the corresponding degrees of freedom of the cytoskeleton (host element) representing the mechanical links between microtubules and their surrounding network of cytoskeletal filaments[59].

The MTOC has the same initial distance from the nucleus in both rectangular and circular substrate geometries. Microtubules can make contact with each other and the MTOC is allowed to make contact with the nucleus, however, the MTOC does not induce any contact pressure on the nucleus before contact. Microtubules are also allowed to make contact with the cell membrane. In the tangential direction, we assume that there is no friction between the cell membrane and microtubules (frictionless contact), while in the normal direction, there is no constraint on the magnitude of contact pressure. The same contact conditions are also assumed for the contact between the MTOC and the nuclear envelope. Our simulations show that the MTOC in the rectangular cell is pushed toward the cell boundary by the nucleus (Figure S38), while in the circular cell (Figure 3B) and the rectangular cell treated with cytochalasin D (Figure 3E), the MTOC pushes against the nucleus and locally indents the nucleus. Note that as described in SI Section 7, microtubules in living cells show higher resistance against actomyosin-driven compressive forces and also buckle with shorter wavelengths since they are laterally reinforced by their surrounding network of cytoskeletal intermediate filaments and actin microfilaments[1].

9. Reversible chromatin condensation

In addition to tensile and shear forces, cells in the body also experience compressive forces[60] which can potentially affect cellular behavior[61]. To study how cells respond to compressive forces, individual fibroblasts on the rectangular micropatterned substrate are subjected to a vertical compressive force of about 2.5 μN for 1h (see reference[62] for more details). Our experimental results show that fibroblasts under the compressive force exhibit depolymerized apical stress fibers (Figure S32A) and lower levels of F-actin (Figure S32B) and p-MLC (Figure S32C).

These results indicate that applying compressive forces on fibroblasts can lead to disruption of actomyosin contractility. Similar to our results in Figures 5D-5F, we find that the decrease in actomyosin contractility of compressed fibroblasts is positively correlated with higher nuclear accumulation of HDAC (Figure 5J) and chromatin condensation (Figure S33). To test whether these changes are reversible, we remove the compressive force and allow the cells to recover for 1h[62]. Figure S33 shows that fibroblasts revert to their original states after removal of the compressive forces. These experiments show the reversible nature of these processes under our experimental conditions which allows us to theoretically model the nucleus as an elastic material. Interestingly, it has been recently shown that these changes in chromatin structures and nuclear morphology can be reversible or irreversible depending on the time of exposure to mechanical microenvironments[63]. Human mesenchymal stem cells (hMSCs) were cultured on hydrogels that can rapidly undergo in situ softening after being exposed to very low doses of light. In agreement with the model predictions in Figure S19, it was first shown that both nuclear sphericity and chromatin condensation level decrease when hMSCs are cultured on stiff substrates[63]. It was then shown that these changes in nuclear morphology and chromatin structure are reversible upon substrate softening if the time of exposure to stiff substrates is short, while these changes can become irreversible when hMSCs are exposed to stiff substrates for a long time period (10 days)[63]. This irreversible behavior of the nucleus observed after 10 days cannot be captured by the presented model and will be the subject of our future work.

References

1. Brangwynne, C. P. *et al.* Microtubules can bear enhanced compressive loads in living cells because of lateral reinforcement. *The Journal of Cell Biology* **173**, 733–741 (2006).
2. Icard-Arcizet, D., Cardoso, O., Richert, A. & Hénon, S. Cell stiffening in response to external stress is correlated to actin recruitment. *Biophys. J.* **94**, 2906–2913 (2008).
3. Hall, M. S. *et al.* Fibrous nonlinear elasticity enables positive mechanical feedback between cells and ECMs. *Proceedings of the National Academy of Sciences* **113**, 14043–14048 (2016).
4. Shenoy, V. B., Wang, H. & Wang, X. A chemo-mechanical free-energy-based approach to model durotaxis and extracellular stiffness-dependent contraction and polarization of cells. *Interface Focus* **6**, 20150067 (2016).
5. Turgay, Y. *et al.* The molecular architecture of lamins in somatic cells. *Nature* **543**, 261–264 (2017).
6. Stephens, A. D., Banigan, E. J., Adam, S. A., Goldman, R. D. & Marko, J. F. Chromatin and lamin A determine two different mechanical response regimes of the cell nucleus. *Molecular Biology of the Cell* **28**, 1984–1996 (2017).
7. Swift, J. *et al.* Nuclear Lamin-A Scales with Tissue Stiffness and Enhances Matrix-Directed Differentiation. *Science* **341**, 1240104–1240104 (2013).
8. Kolodney, M. S. & Elson, E. L. Contraction due to microtubule disruption is associated with increased phosphorylation of myosin regulatory light chain. *Proceedings of the National Academy of Sciences* **92**, 10252–10256 (1995).
9. Buxboim, A. *et al.* Coordinated increase of nuclear tension and lamin-A with matrix stiffness outcompetes lamin-B receptor that favors soft tissue phenotypes. *MBoC* **28**, 3333–3348 (2017).
10. Kim, J.-K. *et al.* Nuclear lamin A/C harnesses the perinuclear apical actin cables to protect nuclear morphology. *Nature Communications* **8**, 2123 (2017).
11. Ishijima, A., Doi, T., Sakurada, K. & Yanagida, T. Sub-piconewton force fluctuations of actomyosin in vitro. *Nature* **352**, 301–306 (1991).
12. Pollard, T. D. Structure and polymerization of Acanthamoeba myosin-II filaments. *J. Cell Biol.* **95**, 816–825 (1982).
13. de Souza Neto, E. A., Peri, D. & Owen, D. R. J. *Computational Methods for Plasticity*. (John Wiley & Sons, Ltd, 2008). doi:10.1002/9780470694626

14. Talwar, S., Jain, N. & Shivashankar, G. V. The regulation of gene expression during onset of differentiation by nuclear mechanical heterogeneity. *Biomaterials* **35**, 2411–2419 (2014).
15. Lee, J. S. H. *et al.* Nuclear Lamin A/C Deficiency Induces Defects in Cell Mechanics, Polarization, and Migration. *Biophysical Journal* **93**, 2542–2552 (2007).
16. Shimamoto, Y., Tamura, S., Masumoto, H. & Maeshima, K. Nucleosome–nucleosome interactions via histone tails and linker DNA regulate nuclear rigidity. *Molecular Biology of the Cell* **28**, 1580–1589 (2017).
17. Panorchan, P., Schafer, B. W., Wirtz, D. & Tseng, Y. Nuclear Envelope Breakdown Requires Overcoming the Mechanical Integrity of the Nuclear Lamina. *Journal of Biological Chemistry* **279**, 43462–43467 (2004).
18. Mazumder, A., Roopa, T., Basu, A., Mahadevan, L. & Shivashankar, G. V. Dynamics of Chromatin Decondensation Reveals the Structural Integrity of a Mechanically Prestressed Nucleus. *Biophysical Journal* **95**, 3028–3035 (2008).
19. Jain, N., Iyer, K. V., Kumar, A. & Shivashankar, G. V. Cell geometric constraints induce modular gene-expression patterns via redistribution of HDAC3 regulated by actomyosin contractility. *Proceedings of the National Academy of Sciences* **110**, 11349–11354 (2013).
20. Damodaran, K. *et al.* Compressive force induces reversible chromatin condensation and cell geometry dependent transcriptional response. *Molecular Biology of the Cell* mbc.E18-04-0256 (2018). doi:10.1091/mbc.E18-04-0256
21. Mitra, A. *et al.* Cell geometry dictates TNFα-induced genome response. *Proceedings of the National Academy of Sciences* **114**, E3882–E3891 (2017).
22. Iyer, K. V., Pulford, S., Mogilner, A. & Shivashankar, G. V. Mechanical Activation of Cells Induces Chromatin Remodeling Preceding MKL Nuclear Transport. *Biophysical Journal* **103**, 1416–1428 (2012).
23. Aström, K. J. & Murray, R. M. *Feedback Systems: An Introduction for Scientists and Engineers*. (Princeton University Press, 2008).
24. Albertos, P. & Mareels, I. *Feedback and Control for Everyone*. (Springer-Verlag, 2010).
25. Bertaud, J., Qin, Z. & Buehler, M. J. Intermediate filament-deficient cells are mechanically softer at large deformation: A multi-scale simulation study. *Acta Biomaterialia* **6**, 2457–2466 (2010).

26. Ackbarow, T. & Buehler, M. J. Superelasticity, energy dissipation and strain hardening of vimentin coiled-coil intermediate filaments: atomistic and continuum studies. *J Mater Sci* **42**, 8771–8787 (2007).

27. Janmey, P. A., Euteneuer, U., Traub, P. & Schliwa, M. Viscoelastic properties of vimentin compared with other filamentous biopolymer networks. *The Journal of Cell Biology* **113**, 155–160 (1991).

28. Herrmann, H., Bär, H., Kreplak, L., Strelkov, S. V. & Aebi, U. Intermediate filaments: from cell architecture to nanomechanics. *Nature Reviews Molecular Cell Biology* **8**, 562–573 (2007).

29. Qin, Z., Kreplak, L. & Buehler, M. J. Nanomechanical properties of vimentin intermediate filament dimers. *Nanotechnology* **20**, 425101 (2009).

30. Kreplak, L., Bär, H., Leterrier, J. F., Herrmann, H. & Aebi, U. Exploring the Mechanical Behavior of Single Intermediate Filaments. *Journal of Molecular Biology* **354**, 569–577 (2005).

31. Qin, Z., Buehler, M. J. & Kreplak, L. A multi-scale approach to understand the mechanobiology of intermediate filaments. *Journal of Biomechanics* **43**, 15–22 (2010).

32. Qin, Z., Kreplak, L. & Buehler, M. J. Hierarchical Structure Controls Nanomechanical Properties of Vimentin Intermediate Filaments. *PLOS ONE* **4**, e7294 (2009).

33. Ackbarow, T., Sen, D., Thaulow, C. & Buehler, M. J. Alpha-Helical Protein Networks Are Self-Protective and Flaw-Tolerant. *PLOS ONE* **4**, e6015 (2009).

34. Brodland, G. W. & Gordon, R. Intermediate Filaments May Prevent Buckling of Compressively Loaded Microtubules. *J Biomech Eng* **112**, 319–321 (1990).

35. Wang, N. & Stamenović, D. Contribution of intermediate filaments to cell stiffness, stiffening, and growth. *American Journal of Physiology-Cell Physiology* **279**, C188–C194 (2000).

36. Wang, N. & Stamenovic, D. Mechanics of vimentin intermediate filaments. *J Muscle Res Cell Motil* **23**, 535–540 (2002).

37. Mendez, M. G., Restle, D. & Janmey, P. A. Vimentin Enhances Cell Elastic Behavior and Protects against Compressive Stress. *Biophysical Journal* **107**, 314–323 (2014).

38. Lowery, J., Kuczmarski, E. R., Herrmann, H. & Goldman, R. D. Intermediate Filaments Play a Pivotal Role in Regulating Cell Architecture and Function. *J. Biol. Chem.* **290**, 17145–17153 (2015).

39. Eckes, B. *et al.* Impaired mechanical stability, migration and contractile capacity in vimentin-deficient fibroblasts. *Journal of Cell Science* **111**, 1897–1907 (1998).

40. Patteson, A. E. *et al.* Vimentin protects the structural integrity of the nucleus and suppresses nuclear damage caused by large deformations. *bioRxiv* 566174 (2019). doi:10.1101/566174

41. Patteson, A. E. *et al.* Loss of vimentin intermediate filaments decreases peri-nuclear stiffness and enhances cell motility through confined spaces. *bioRxiv* 371047 (2018). doi:10.1101/371047

42. Ramms, L. *et al.* Keratins as the main component for the mechanical integrity of keratinocytes. *PNAS* **110**, 18513–18518 (2013).

43. Ivaska, J., Pallari, H.-M., Nevo, J. & Eriksson, J. E. Novel functions of vimentin in cell adhesion, migration, and signaling. *Experimental Cell Research* **313**, 2050–2062 (2007).

44. Guo, M. *et al.* The Role of Vimentin Intermediate Filaments in Cortical and Cytoplasmic Mechanics. *Biophysical Journal* **105**, 1562–1568 (2013).

45. Vahabikashi, A. *et al.* Probe Sensitivity to Cortical versus Intracellular Cytoskeletal Network Stiffness. *Biophysical Journal* **116**, 518–529 (2019).

46. Gladilin, E., Gonzalez, P. & Eils, R. Dissecting the contribution of actin and vimentin intermediate filaments to mechanical phenotype of suspended cells using high-throughput deformability measurements and computational modeling. *Journal of Biomechanics* **47**, 2598–2605 (2014).

47. Jiu, Y. *et al.* Vimentin intermediate filaments control actin stress fiber assembly through GEF-H1 and RhoA. *J Cell Sci* **130**, 892–902 (2017).

48. van Loosdregt, I. A. E. W. *et al.* The Mechanical Contribution of Vimentin to Cellular Stress Generation. *J Biomech Eng* **140**, 061006-061006–10 (2018).

49. Shabbir, S. H., Cleland, M. M., Goldman, R. D. & Mrksich, M. Geometric control of vimentin intermediate filaments. *Biomaterials* **35**, 1359–1366 (2014).

50. Costigliola, N. *et al.* Vimentin fibers orient traction stress. *PNAS* **114**, 5195–5200 (2017).

51. Neelam, S. *et al.* Direct force probe reveals the mechanics of nuclear homeostasis in the mammalian cell. *PNAS* **112**, 5720–5725 (2015).

52. Almeida, F. V. *et al.* The cytolinker plectin regulates nuclear mechanotransduction in keratinocytes. *J Cell Sci* **128**, 4475–4486 (2015).

53. Versaevel, M., Grevesse, T. & Gabriele, S. Spatial coordination between cell and nuclear shape within micropatterned endothelial cells. *Nature Communications* **3**, (2012).

54. Sarria, A. J., Lieber, J. G., Nordeen, S. K. & Evans, R. M. The presence or absence of a vimentin-type intermediate filament network affects the shape of the nucleus in human SW-13 cells. *Journal of Cell Science* **107**, 1593–1607 (1994).

55. Petrie, R. J., Koo, H. & Yamada, K. M. Generation of compartmentalized pressure by a nuclear piston governs cell motility in a 3D matrix. *Science* **345**, 1062–1065 (2014).

56. Wilhelmsen, K. *et al.* Nesprin-3, a novel outer nuclear membrane protein, associates with the cytoskeletal linker protein plectin. *The Journal of Cell Biology* **171**, 799–810 (2005).

57. Bouchet, B. P. & Akhmanova, A. Microtubules in 3D cell motility. *J Cell Sci* **130**, 39–50 (2017).

58. Kwon, Y. W. & Bang, H. *The Finite Element Method Using MATLAB*. (CRC Press, 2000).

59. Huber, F., Boire, A., López, M. P. & Koenderink, G. H. Cytoskeletal crosstalk: when three different personalities team up. *Current Opinion in Cell Biology* **32**, 39–47 (2015).

60. Wells, R. G. Tissue mechanics and fibrosis. *Biochimica et Biophysica Acta (BBA) - Molecular Basis of Disease* **1832**, 884–890 (2013).

61. Kanazawa, T. *et al.* Biological Responses of Three-Dimensional Cultured Fibroblasts by Sustained Compressive Loading Include Apoptosis and Survival Activity. *PLOS ONE* **9**, e104676 (2014).

62. Damodaran, K. *et al.* Compressive force induces reversible chromatin condensation and cell geometry–dependent transcriptional response. *MBoC* **29**, 3039–3051 (2018).

63. Killaars, A. R. *et al.* Extended Exposure to Stiff Microenvironments Leads to Persistent Chromatin Remodeling in Human Mesenchymal Stem Cells. *Advanced Science* **6**, 1801483 (2019).

64. Bao, M., Xie, J., Piruska, A. & Huck, W. T. S. 3D microniches reveal the importance of cell size and shape. *Nature Communications* **8**, 1962 (2017).

65. Oakes, P. W., Banerjee, S., Marchetti, M. C. & Gardel, M. L. Geometry Regulates Traction Stresses in Adherent Cells. *Biophysical Journal* **107**, 825–833 (2014).

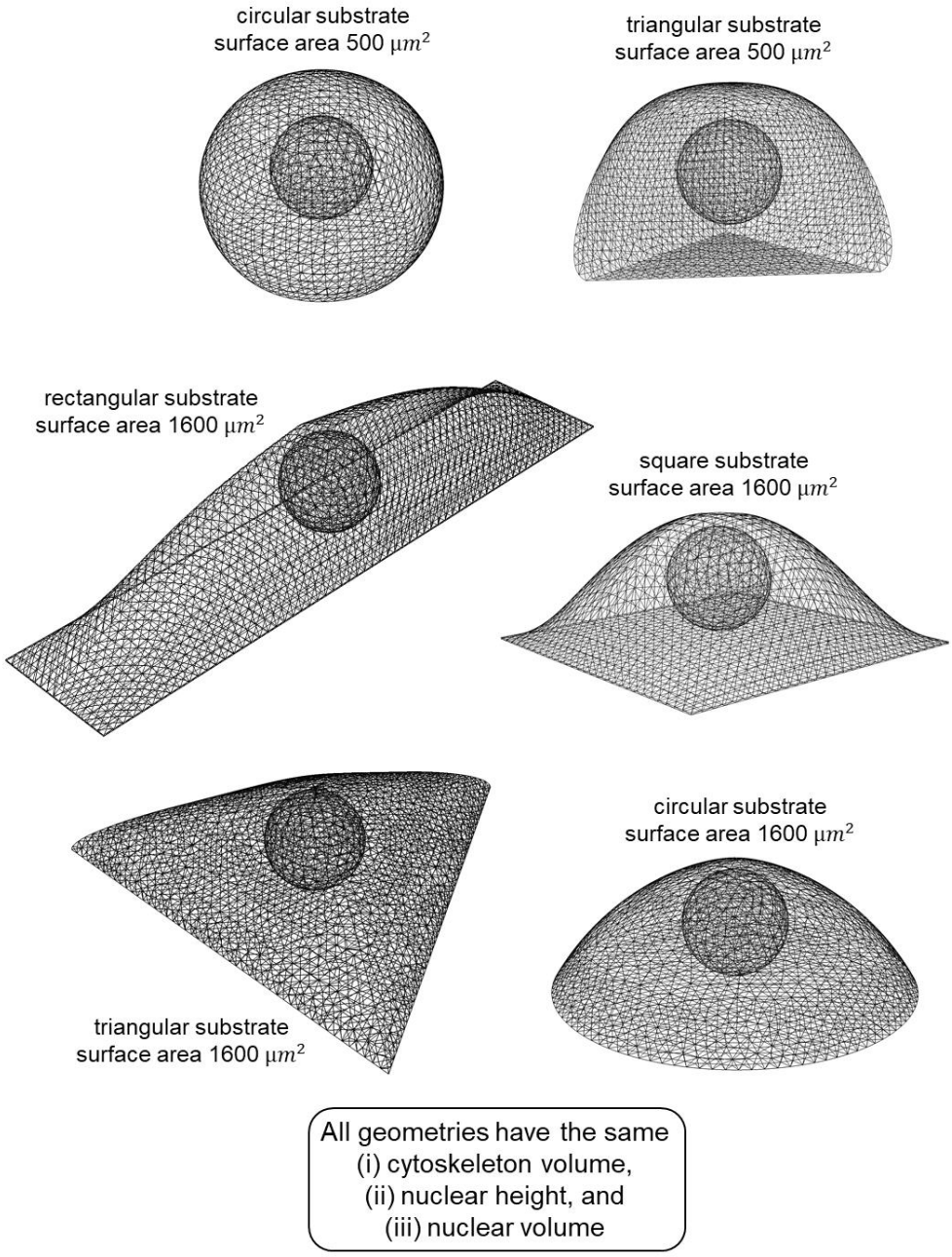

Figure S1. All simulations are carried out with the same initial condition. All cells have the same initial volume. In our model, this indicates that all cells have the same initial number of phosphorylated myosin motors (the same initial contractility). The model then predicts how the cell contractility changes for each substrate geometry and how these actomyosin contractility mediated changes in the cytoskeleton induce alterations in the properties of the nucleus.

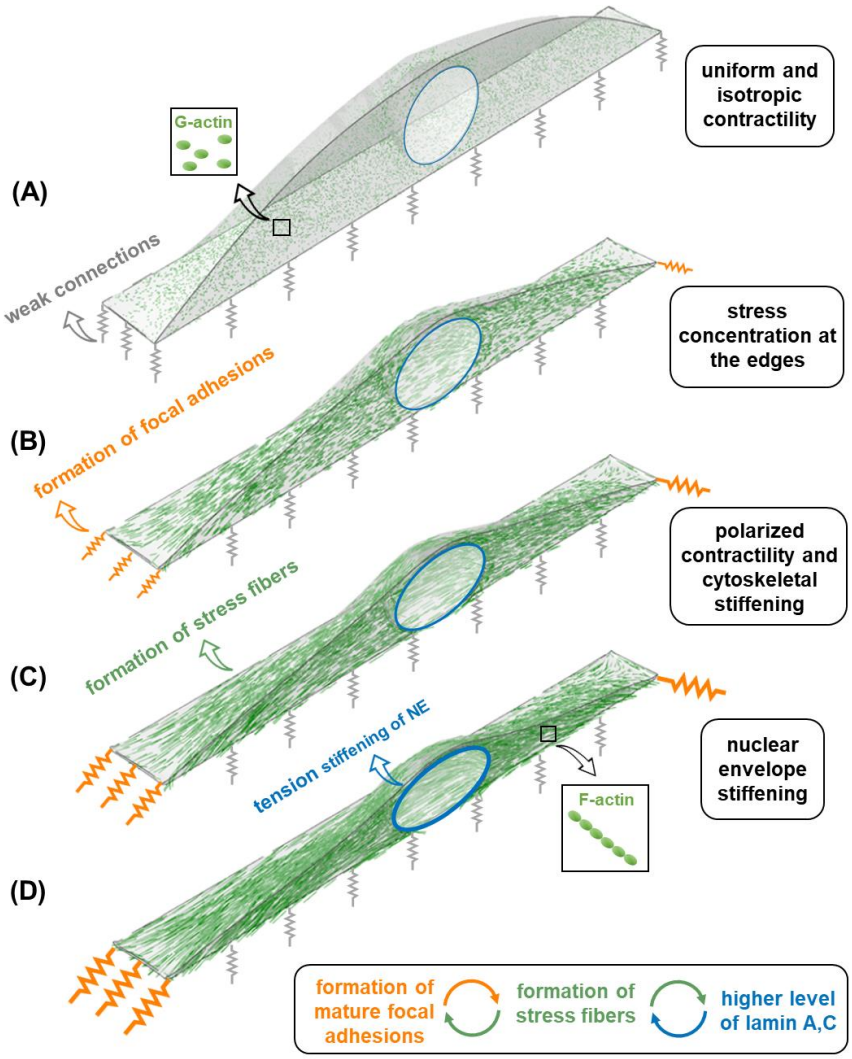

Figure S2. The dynamic reciprocities between the focal adhesions, the cytoskeleton, and the nucleus. (A) The cell contractility is initially isotropic (the same in all directions). (B) The isotropic contractility generates an anisotropic stress field at the cell boundaries where the adhesion layer experiences higher tension at the two ends along the long axis of the cell. As a result, the stiffness of the adhesion layer (the connection to the substrate) increases at the two ends, representing the stress-dependent formation of mature focal adhesions observed in our experiments. (C) The formation of focal adhesions at the two ends generates resistance against cell contraction along the long axis of the cell. Subsequently, tension is generated in the cytoskeleton along the long axis of the cell. In response to the tension in the cytoskeleton, the stiffness of the actin filament network increases along the long axis of the cell, representing the formation of stress fibers observed in our experiments. (D) These changes in the cytoskeleton impose compressive forces on the nucleus leading to a flattened and elongated nuclear morphology. As the nucleus deforms from a round to a flattened and elongated geometry, tension is generated in the nuclear envelope. In response to the tension in the nuclear envelope, the stiffness of the nuclear envelope increases, representing the increased level of lamin A,C observed in our experiments.

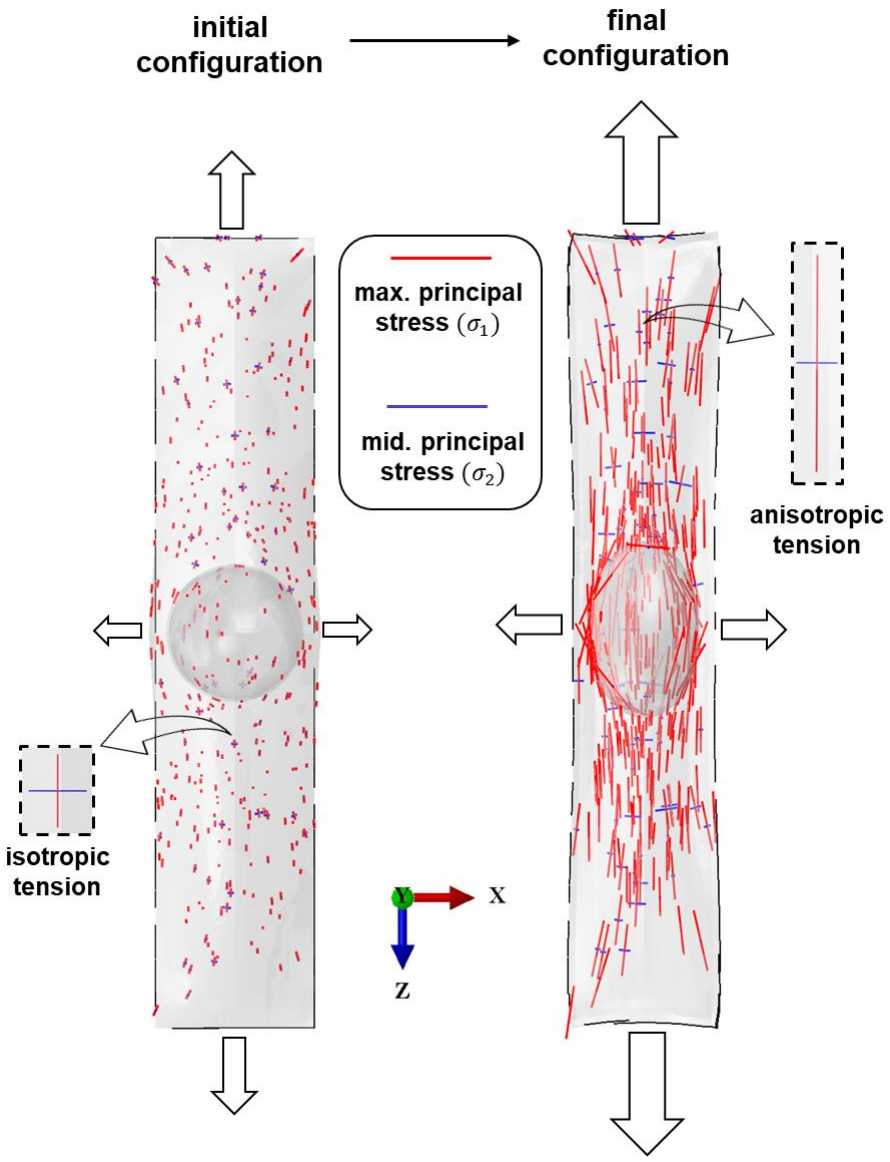

Figure S3. Elongated substrate geometries induce anisotropic tension in the cytoskeleton. As described in Fig. S5, the cell contractility is initially isotropic (independent of direction). However, this isotropic contractility generates an anisotropic stress field at the cell boundaries which in turn leads to anisotropy in the cell contractility and the cytoskeletal stress field.

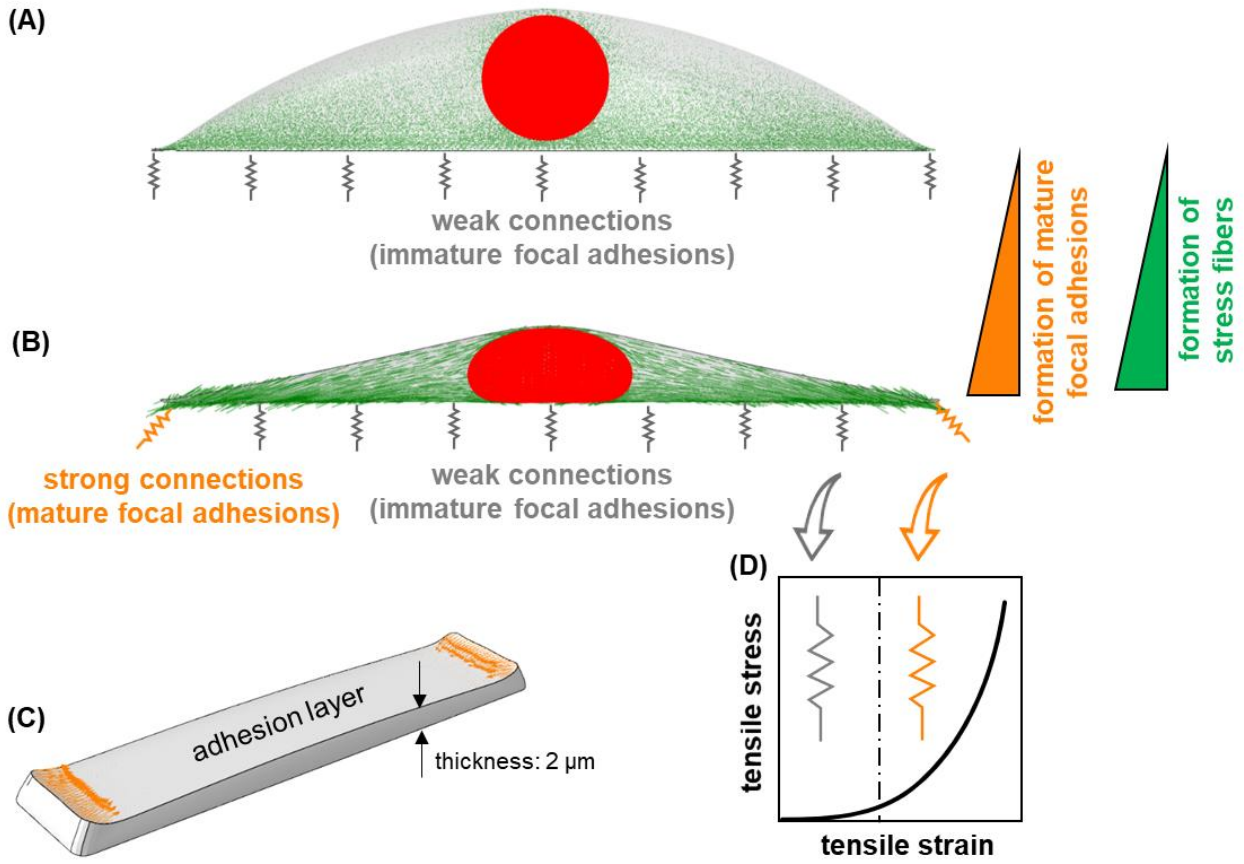

Figure S4. Tension-dependent formation of focal adhesions. Three-dimensional reconstruction of confocal images of fibroblasts in Fig. 2B shows that stress fibers in large rectangular cells are connected to the mature focal adhesions at the two ends along the long axis of the cell. Our simulations in (A) and (B) show how tension is generated in the cytoskeleton as the mature focal adhesions are formed and the contractile cell is connected to the substrate at these mature focal adhesions. To capture the formation of these focal adhesions, we use a thin elastic layer as shown in (C). The adhesion layer is initially soft but significantly stiffens in the directions of the tensile principal stresses when the tensile principal stresses are higher than a critical value of tensile stress (D). For a large rectangular substrate geometry, our simulations show that the adhesion layer experiences the highest amount of tension at the two ends along the long axis of the cell. Subsequently, the adhesion layer stiffens at the two ends and forms strong connections between the cell and the rigid substrate.

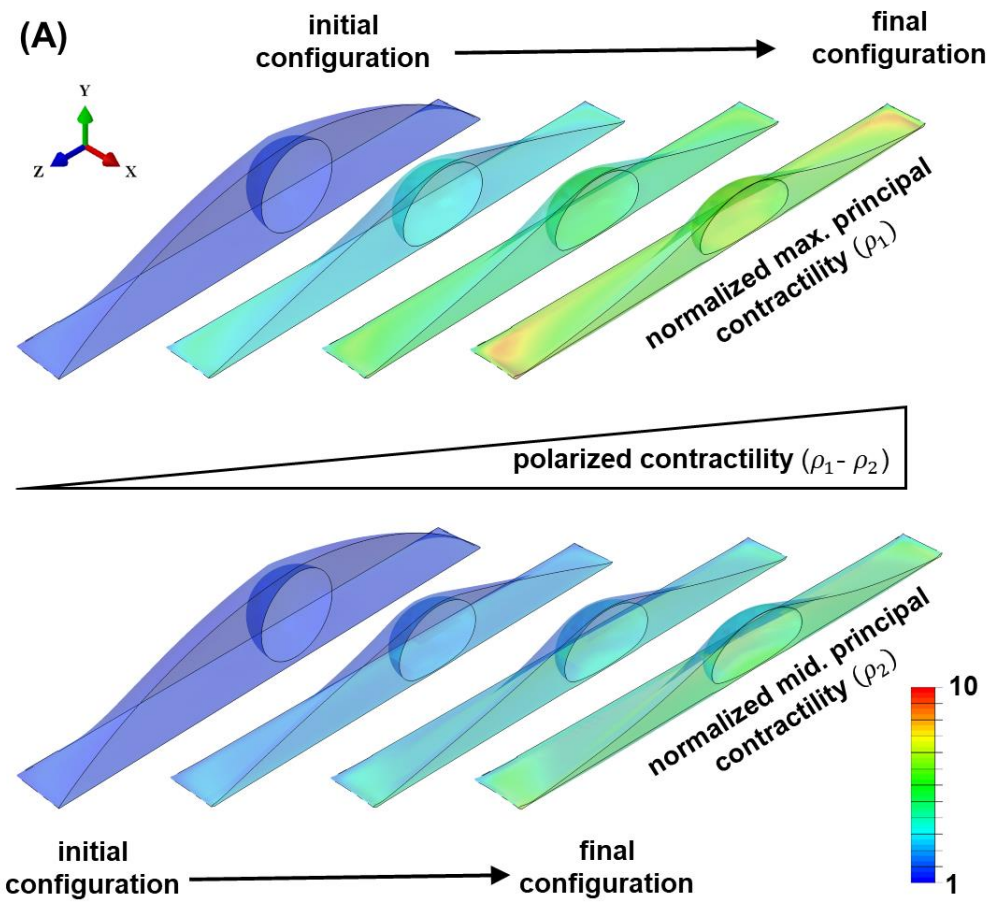
(A)
initial configuration
final configuration
Y
Z
X
normalized max. principal contractility (ρ_1)
polarized contractility (ρ_1- ρ_2)
normalized mid. principal contractility (ρ_2)
10
1
initial configuration
final configuration

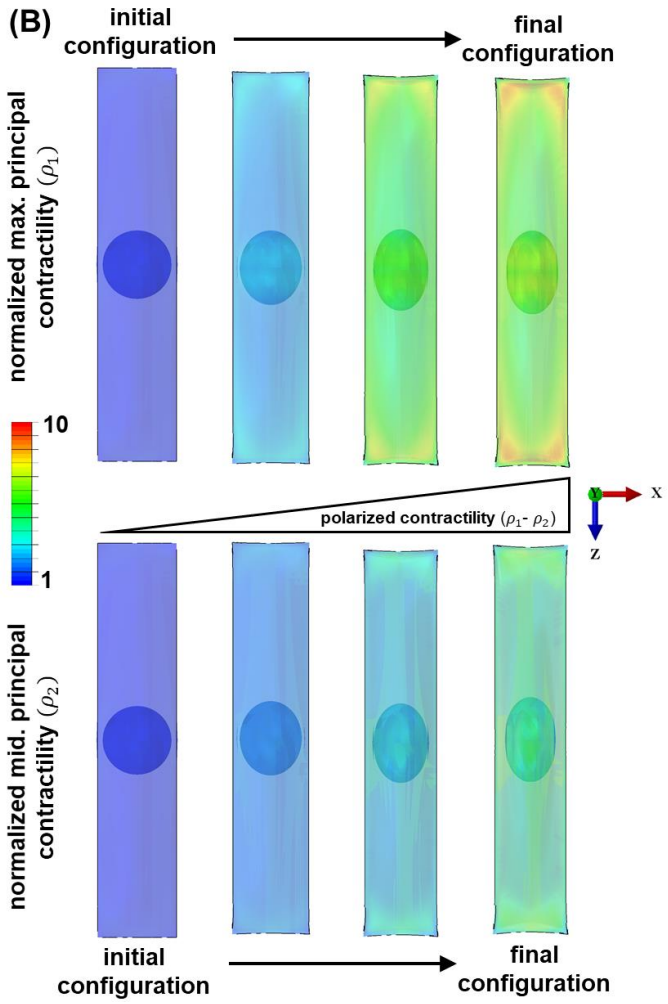

Figure S5. Elongated substrate geometries induce anisotropic contractility. As shown in the isometric (A) and the top (B) views, the cell contractility is initially independent of direction (isotropic contractility) and spatial location (uniform contractility) as it is seeded on its substrate. The isotropic contractility can be seen in the initial configuration where the principal contractility components ρ_1 (primarily along the long axis of the cell: the z-direction) and ρ_2 (primarily along the short axis of the cell: the x-direction) are the same everywhere in the cytoplasm (ρ_1, ρ_2, and ρ_3 are the eigenvalues of the contractility tensor ρ_{ij}). However, for an elongated substrate geometry (e.g., rectangular geometry), this initial isotropic contractility of the cell generates a polarized anisotropic stress field at the cell boundaries which in turn leads to anisotropic contractility of the cell. As shown in the final configuration, the volume averaged of ρ_1 is higher than the volume averaged of ρ_2 which indicates that the cell contractility along the long axis of the cell is higher than the cell contractility along the short axis (polarized contractility). Furthermore, starting with an initial uniform contractility, the cell contractility becomes non-uniform as our model predicts higher contractility (both $\rho_1$and ρ_2) close to the two ends (along the long axis of the cell) where the cell experiences higher tension due to the resistance of the substrate at the mature focal adhesion sites.

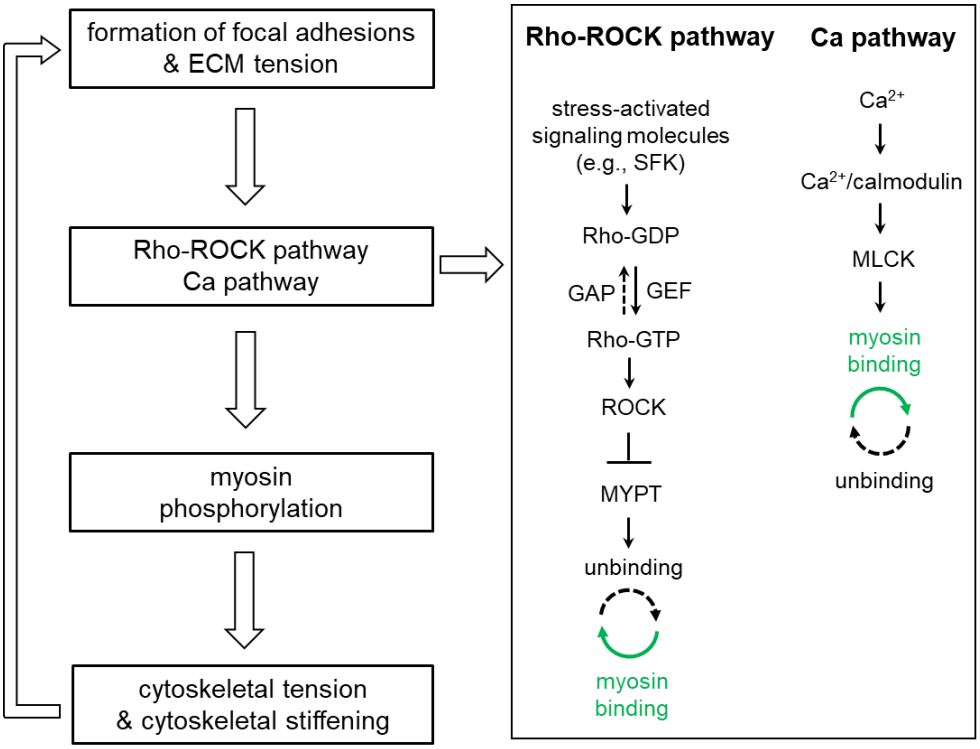

Figure S6. Stress-dependent feedback mechanism. Under homeostatic conditions, the contractile cell pulls on the extracellular matrix (ECM) and subsequently generates tension in the ECM. The cell generated external tension (ECM tension) triggers mechanotransductive feedback mechanisms that are controlled by stress-activated signaling pathways such as the Ca^{2+} and the Rho-Rock pathways. As the main outcome of these stress-activated signaling pathways, myosin motors are phosphorylated which leads to an increase in the density of force dipoles in the direction of the external tension. Higher concentration of phosphorylated myosin motors promotes cell force generation along the direction of the external tension which subsequently leads to an increase in the cytoskeletal tension. The increase in the cytoskeletal tension leads to cell stiffening in an orientation-dependent manner as the cell responds to the increase in the cytoskeletal tension by recruitment and bundling of F-actin into aligned filaments along the direction of the tension. Finally, increases in cell force generation and cell stiffness promote cell contraction which closes the feedback loop in our cell model.

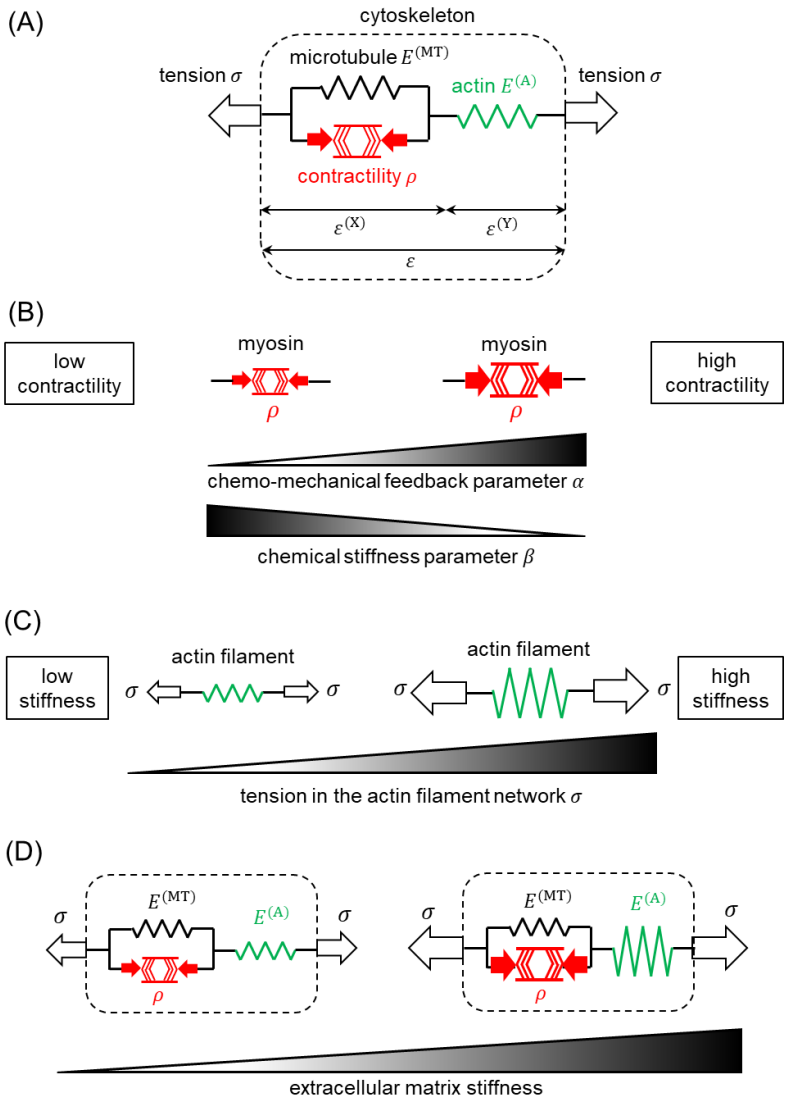

Figure S7. One-dimensional cytoskeletal model. (A) The cytoskeletal model is composed of three elements including (i) the myosin molecular motors, (ii) the microtubule network, and (iii) the actin filament network. (B) A large value of the chemo-mechanical feedback parameter α strengthens the stress-dependent feedback mechanism of the cell as the cell promotes myosin motor phosphorylation in response to the stiffness of its surrounding. A large value of the chemical stiffness parameter β weakens the stress-dependent feedback mechanism of the cell as it makes myosin motor binding more difficult (see SI Section 1). (C) The stiffness of the actin filament network increases with tension. (D) The tension in the actin filament network σ increases with matrix stiffness in our model. Subsequently, the cell responds to the increase in σ by increasing the density of phosphorylated myosin molecular motors which results in an increase in the cell contractility ρ with increasing matrix stiffness. The cell also responds to the increased tension by recruitment of actin filaments and subsequently increasing its own stiffness.

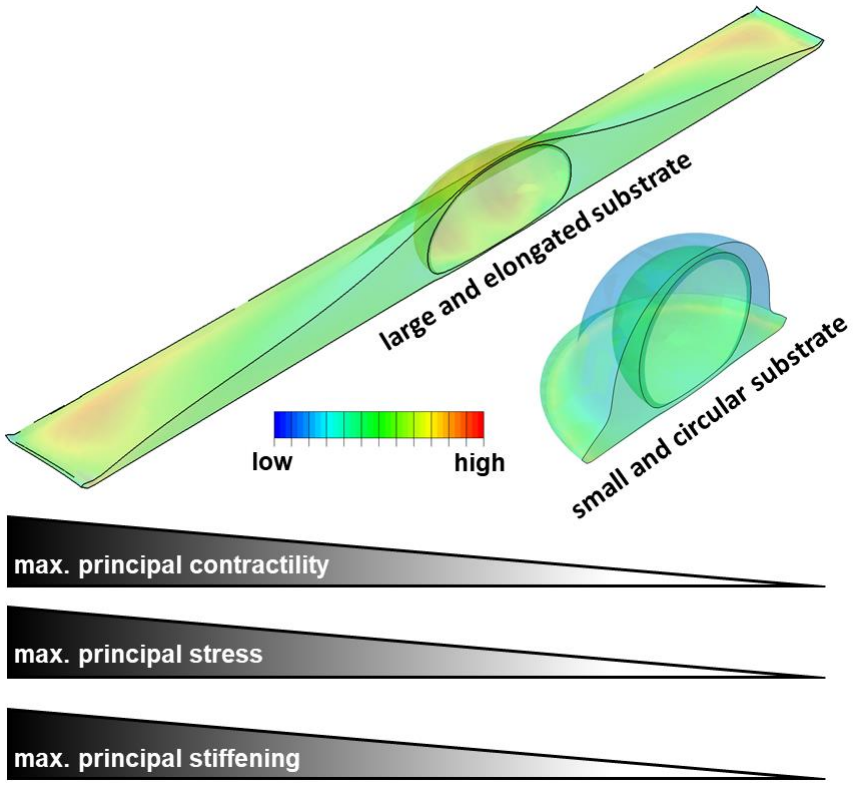

Figure S8. Cell geometric constraints regulate cell contractility, tension in the actin filament network and cell stiffening. Cells on the rectangular substrate (1:5 aspect ratio, 1600 μm^2 substrate surface area) exhibit significantly higher contractility, cytoskeletal tension, and cytoskeletal stiffness compared to the cells on the circular substrate (500 μm^2 substrate surface area). In our three-dimensional coarse-grained model, the averaged density of the phosphorylated myosin motors per unit volume is represented by a symmetric tensor ρ_{ij}. As described in more details in SI Section 2.1, the cell contractility ρ_{ij} in our model is mathematically defined as the volume averaged of force dipoles generated by the phosphorylated myosin motors. For both substrate geometries, the cell contractility ρ_{ij} in our model is initially isotropic and uniform. Therefore, at each point, we initially have $\rho_{11} = \rho_{22} = \rho_{33} = \rho_1 = \rho_2 = \rho_3$ and $\rho_{12} = \rho_{13} = \rho_{23} = 0$ where ρ_{ij} and ρ_i ($i = 1,2,3$ and $j = 1,2,3$) are the components and eigenvalues of the 3-by-3 contractility tensor $\boldsymbol{\rho}$, respectively. Using the same initial conditions for both substrate geometries, the model predicts higher contractility for the rectangular substrate geometry as illustrated by the maximum principal contractility $\rho_{\max} = \max(\rho_1, \rho_2, \rho_3)$. This increase in the cell contractility in the rectangular cell leads to higher tension in the cytoskeleton (represented here by the maximum principal stress $\sigma_{\max} = \max(\sigma_1, \sigma_2, \sigma_3)$ where σ_1, σ_2, and σ_3 are the eigenvalues of the 3-by-3 stress tensor $\boldsymbol{\sigma}$) and higher stiffness of the actin filament network (represented here by $\mathrm{d}\sigma_{\max} / \mathrm{d}\varepsilon_{\max}^{(\mathrm{Y})}$ with $\varepsilon_{\max}^{(\mathrm{Y})} = \max(\varepsilon_1^{(\mathrm{Y})}, \varepsilon_2^{(\mathrm{Y})}, \varepsilon_3^{(\mathrm{Y})})$ where $\varepsilon_1^{(\mathrm{Y})}$, $\varepsilon_2^{(\mathrm{Y})}$, and $\varepsilon_3^{(\mathrm{Y})}$ are the eigenvalues of the 3-by-3 strain tensor $\boldsymbol{\varepsilon}^{(Y)}$, see Figure S7).

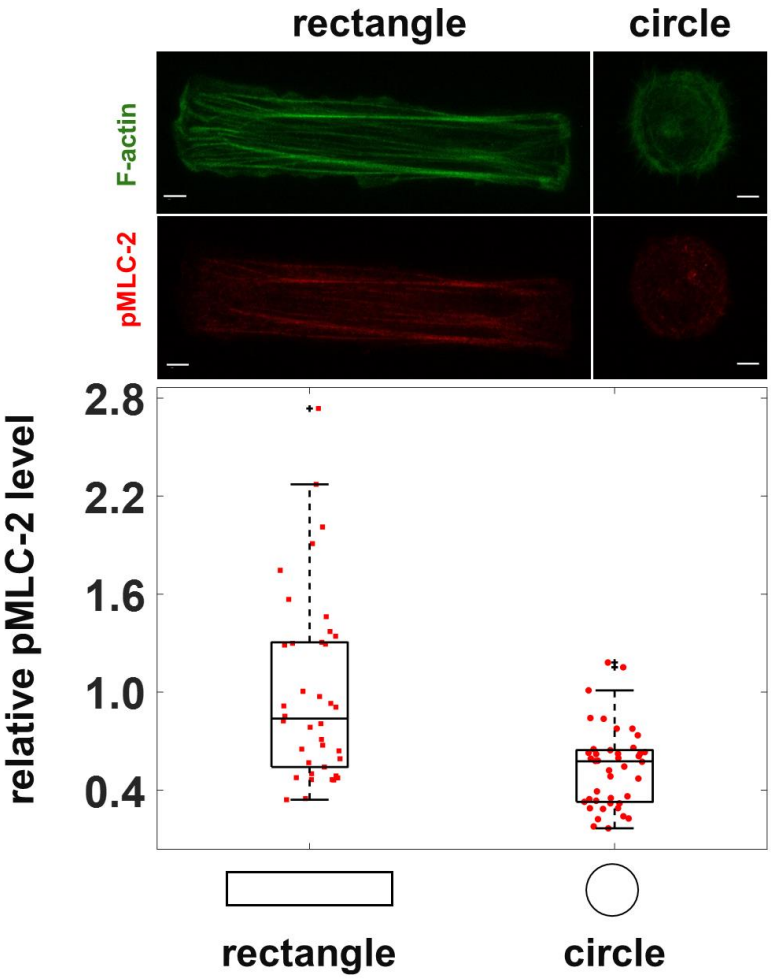

Figure S9. Constraining cells on small and circular substrates leads to disruption of actomyosin contractility. Fibroblasts are cultured on two extreme geometries of fibronectin-coated micropatterns: (i) a rectangle with an aspect ratio of 1:5 and a substrate surface area of 1600 μm^2 (large and elongated geometry), and (ii) a circle with a substrate surface area of 500 μm^2 (small and symmetric geometry). Top: maximum intensity projection of confocal image stacks of rectangular and circular fibroblasts with phalloidin staining of F-actin (green) and immunofluorescence staining of phosphorylated myosin light chain 2 at serine 19 (red). Bottom: relative levels of phosphorylated myosin light chain 2 at serine 19 based on immunofluorescence staining. Scale bar: 5 µm

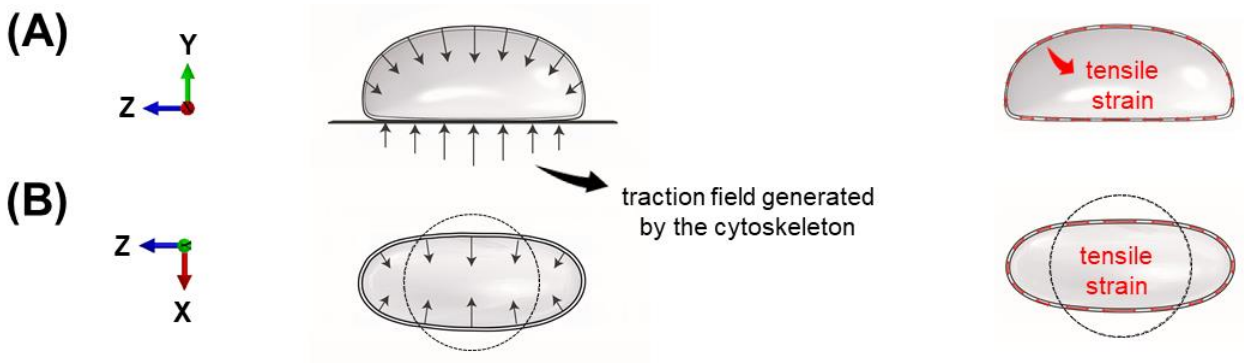

Figure S10. Compressive forces in large and elongated substrate geometries generate tension in the nuclear envelope. Fibroblasts are cultured on rectangular substrates with an aspect ratio of 1:5 and a substrate area of 1600 μm^2. Actomyosin-driven apical (A) and lateral (B) compressive forces regulate nuclear morphology and generate tension in the nuclear envelope lamina network.

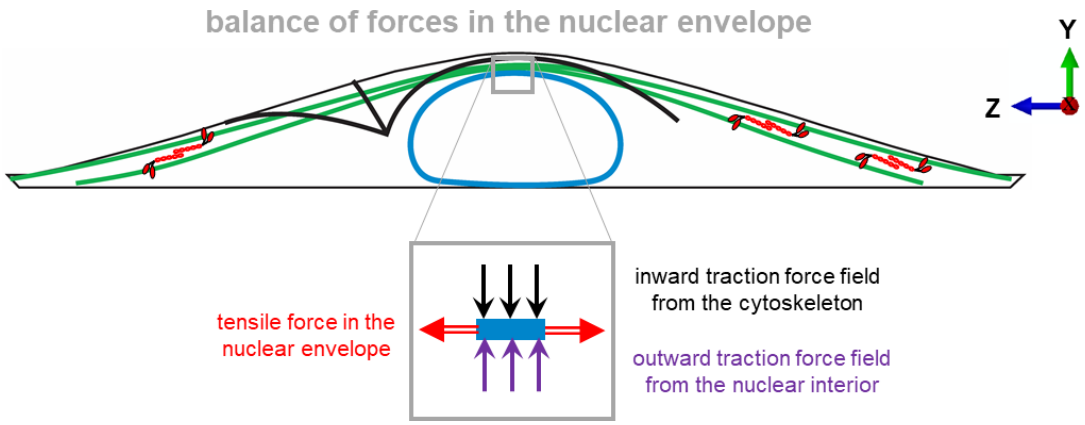

Figure S11. Mechanical force balance in the nuclear envelope. The nuclear envelope experiences inward traction force field generated by prenuclear stress fibers. The nuclear envelope also experiences outward mechanical forces from the nuclear interior including (i) the resistance forces due to chromatin deformations, and (ii) the internal pressure due to chromatin decondensation and fluid content. In the steady-state configuration, the inward and outward forces are balanced by the mechanical resistance of the nuclear envelope.

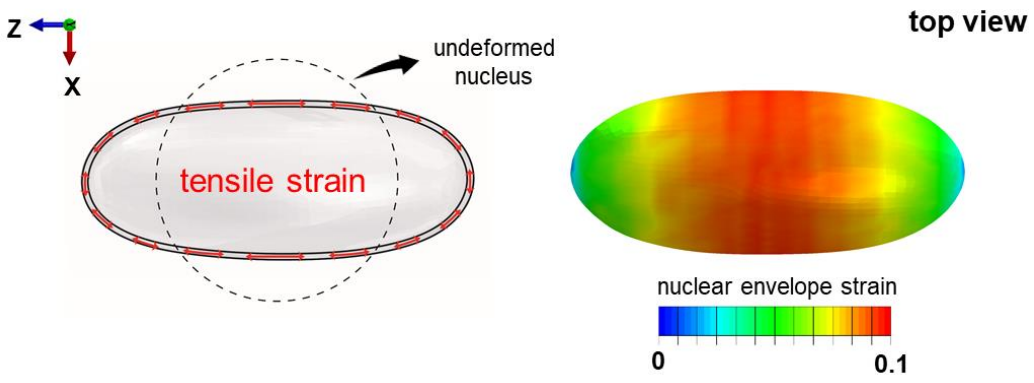

Figure S12. The maximum tensile strain in the nuclear envelope occurs at the lateral side. Left: the nuclear envelope in the rectangular cell is stretched (red arrows) as the nucleus deforms from a round to a flattened and elongated geometry. Right: Maximum tensile strain in the nuclear envelope.

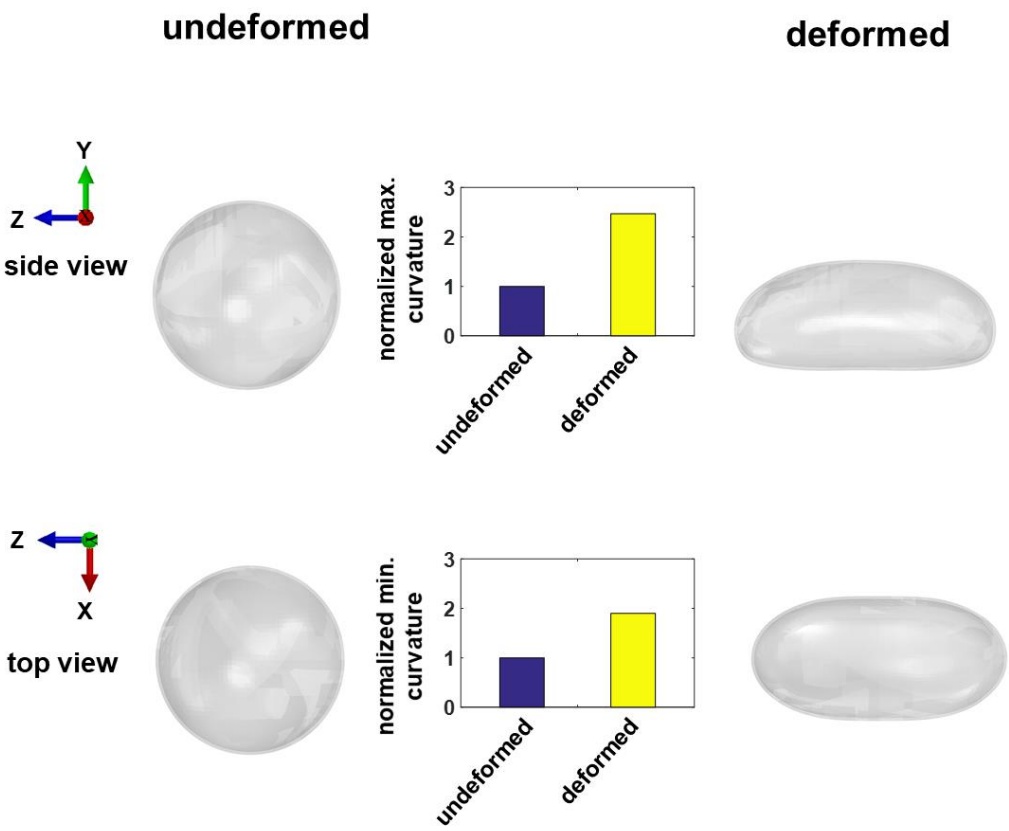

Figure S13. Nuclear curvature increases with actomyosin contractility. Both maximum and minimum curvatures increase with actomyosin contractility as the nucleus becomes flattened and elongated.

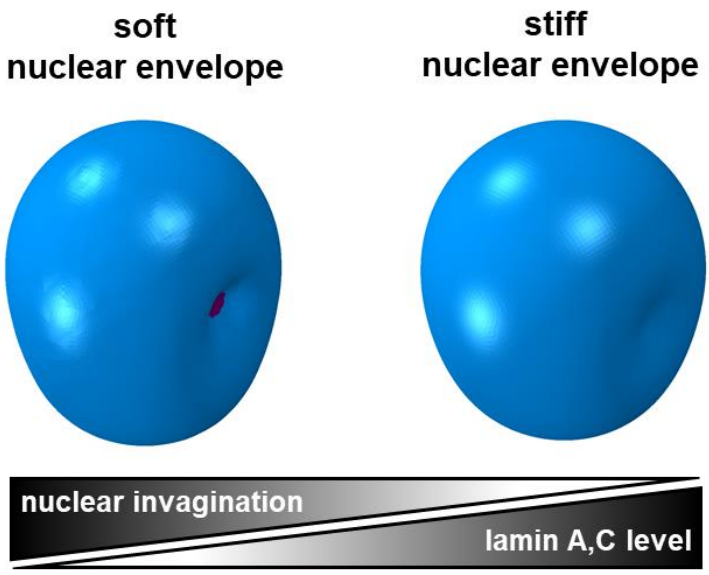

Figure S14. Nuclei with lower levels of lamin A,C are more indented by the MTOC (model predictions). The MTOC indentation of the nucleus in the circular cell decreases with increasing nuclear lamina stiffness (simulation results).

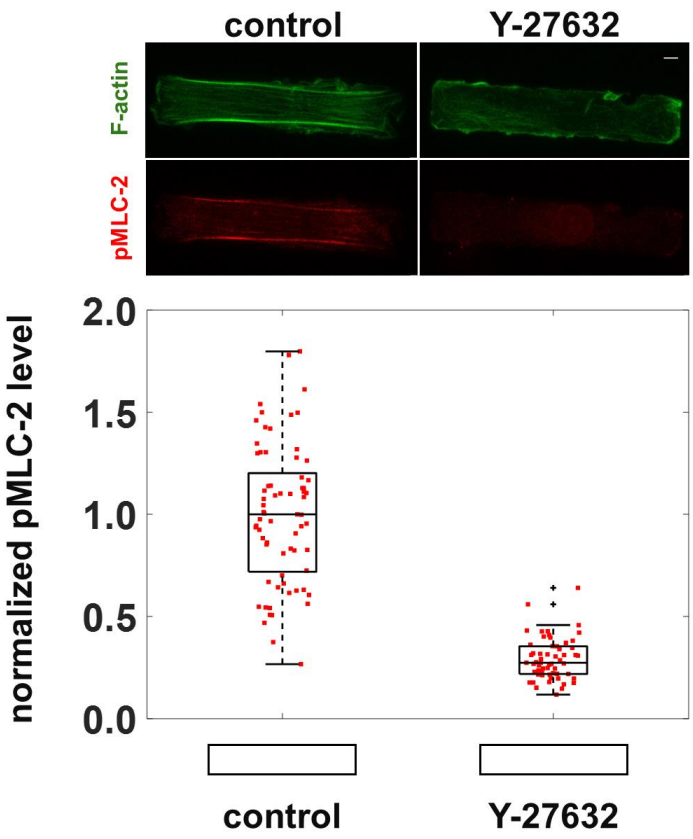

Figure S15. Disruption of actomyosin contractility upon treatment of fibroblasts with Y-27632. Fibroblasts are cultured on rectangular substrates with an aspect ratio of 1:5 and a substrate area of 1600 μm^2. Top: maximum intensity projection of confocal image stacks of control and Y-27632 treated fibroblasts with phalloidin staining of F-actin (green) and immunofluorescence staining of phosphorylated myosin light chain 2 at serine 19 (red). Bottom: relative levels of phosphorylated myosin light chain 2 at serine 19 based on immunofluorescence staining. The subsequent effects of disruption of actomyosin contractility on the properties of the nucleus are presented in Figures S16, S26, and S27. Scale bar: 5 µm

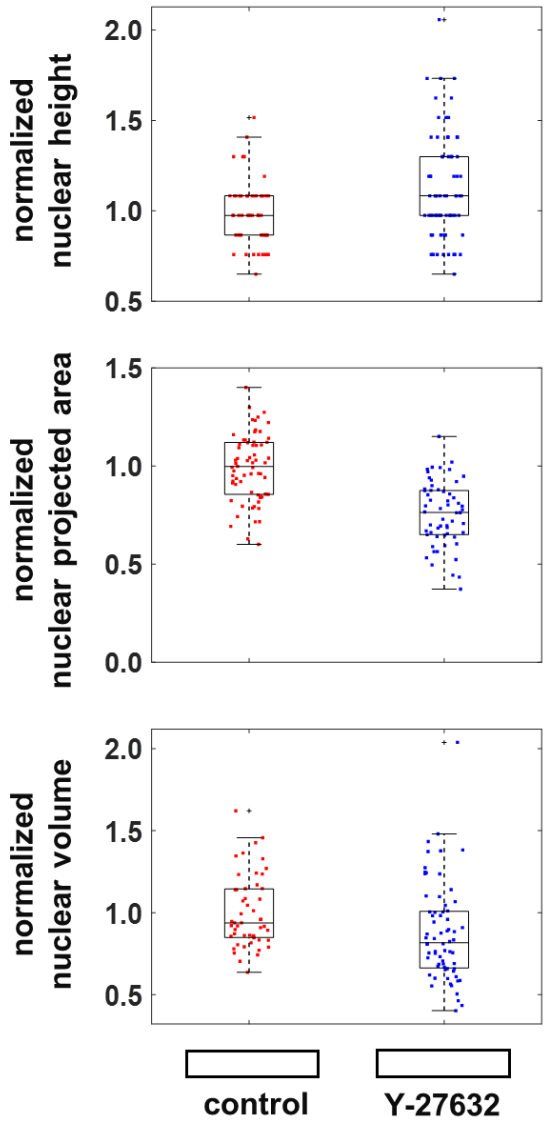

Figure S16. Disruption of actomyosin contractility leads to an increase in nuclear height and decreases in nuclear projected area and nuclear volume. Fibroblasts are cultured on rectangular substrates with an aspect ratio of 1:5 and a substrate area of 1600 μm^2. Disruption of actomyosin contractility upon treatment of fibroblasts with Y-27632 causes depolymerization of apical stress fibers. As a result, inward actomyosin-driven compressive forces on the nucleus decrease and nuclear height increases. Since actomyosin-driven compressive forces on the nucleus decrease with Y-27632 treatment, cells treated with Y-27632 are expected to have higher nuclear volume. However, the compaction of chromatin observed in Supplementary Figure 25 causes fluid to flow out of the nucleus which in turn leads to the shrinkage of the nuclear volume as observed in our experiments.

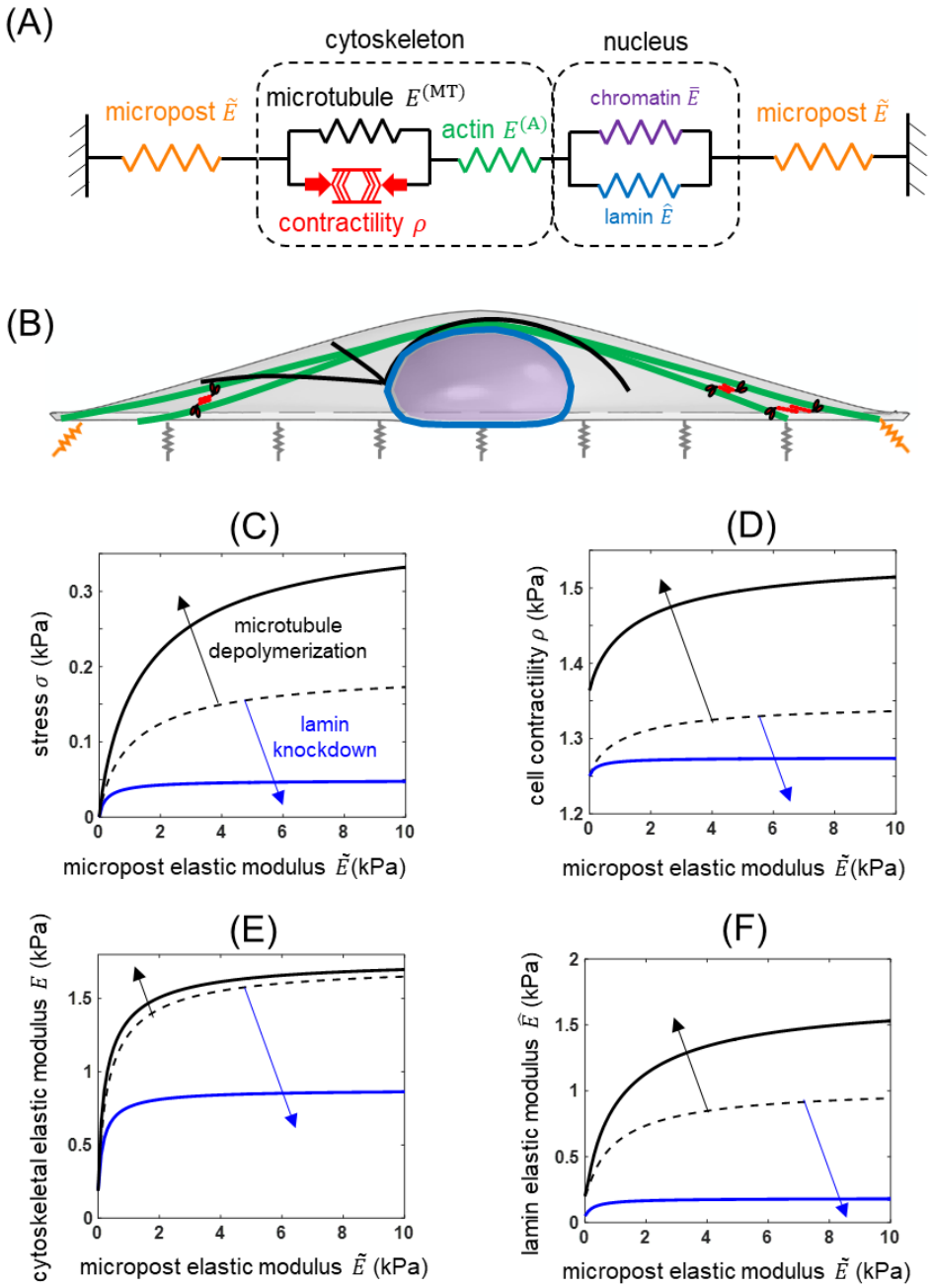

Figure S17. Lamin A,C increases with matrix stiffness and depolymerization of microtubules. A one-dimensional model for a cell adherent to microposts (A) shows that cytoskeletal tension (C), cell contractility (D), cytoskeletal stiffness (E), and lamin A,C level (F) increase with matrix stiffness and depolymerization of microtubules. On the other hand, lamin A,C knockdown leads to decreases in actomyosin contractility (C-E).

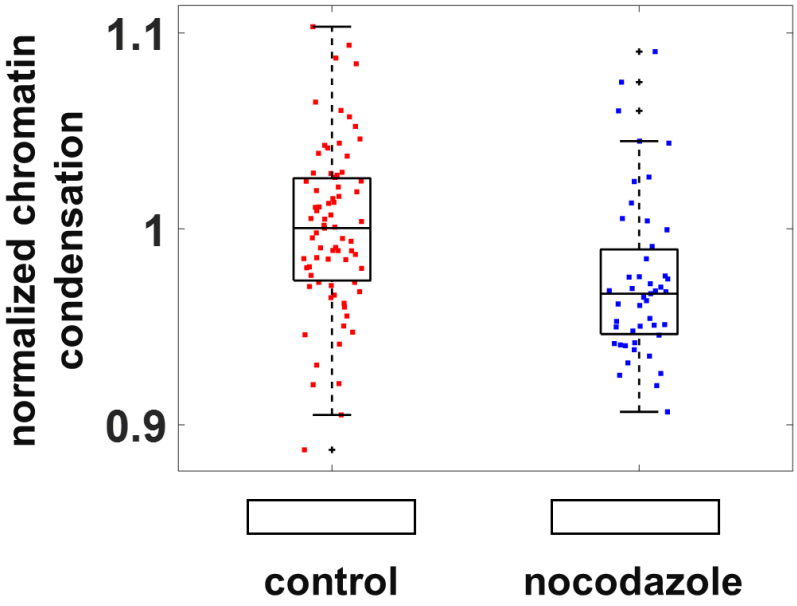

Figure S18. Depolymerization of microtubules does not significantly change chromatin stiffness. Fibroblasts are cultured on a rectangular substrate with a surface area of 1600 μm^2 and an aspect ratio of 1:5 (large and elongated geometry). Chromatin is slightly decondensed upon treatment of fibroblasts with nocodazole based on DAPI staining.

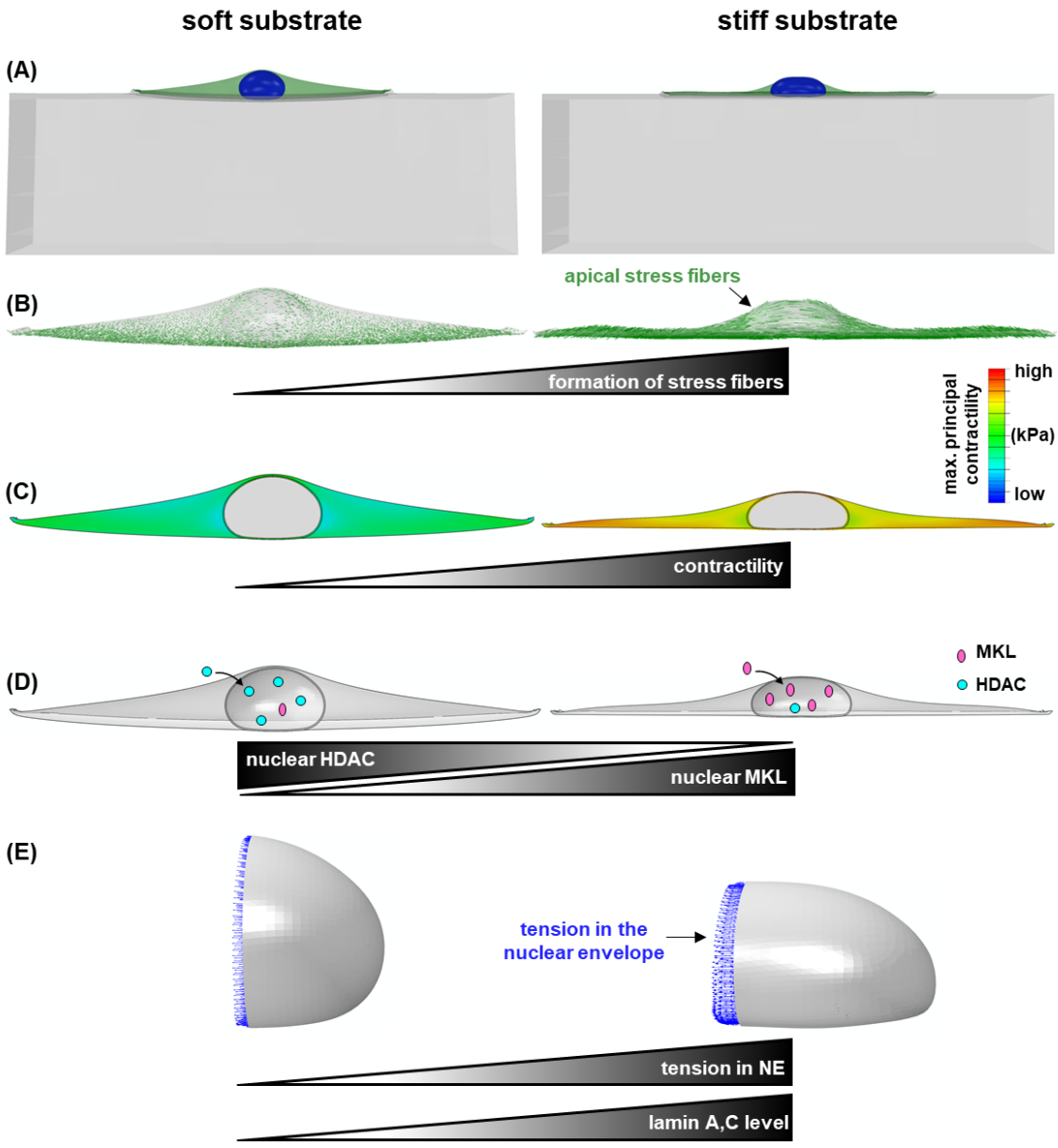

Figure S19. Substrate stiffness induces alterations in the properties of the nucleus (model predictions). (A) The nucleus becomes flattened (lower height) and elongated (higher aspect ratio) with increasing substrate stiffness. (B) Stress fibers are formed, and cytoskeleton stiffness increases with substrate stiffness. (C) Phosphorylation of myosin molecular motors increases with substrate stiffness. (D) Changes in the level of actomyosin contractility lead to translocation of MKL and HDAC. (E) Tensile stresses in the nuclear envelope increase with matrix stiffness correlated with the increased level of lamin A,C and stiffening of the nuclear envelope. Note that, although cells are known to be less spread on soft substrates, in these simulations we keep the substrate area constant for both soft and stiff substrates to study only the effect of substrate stiffness.

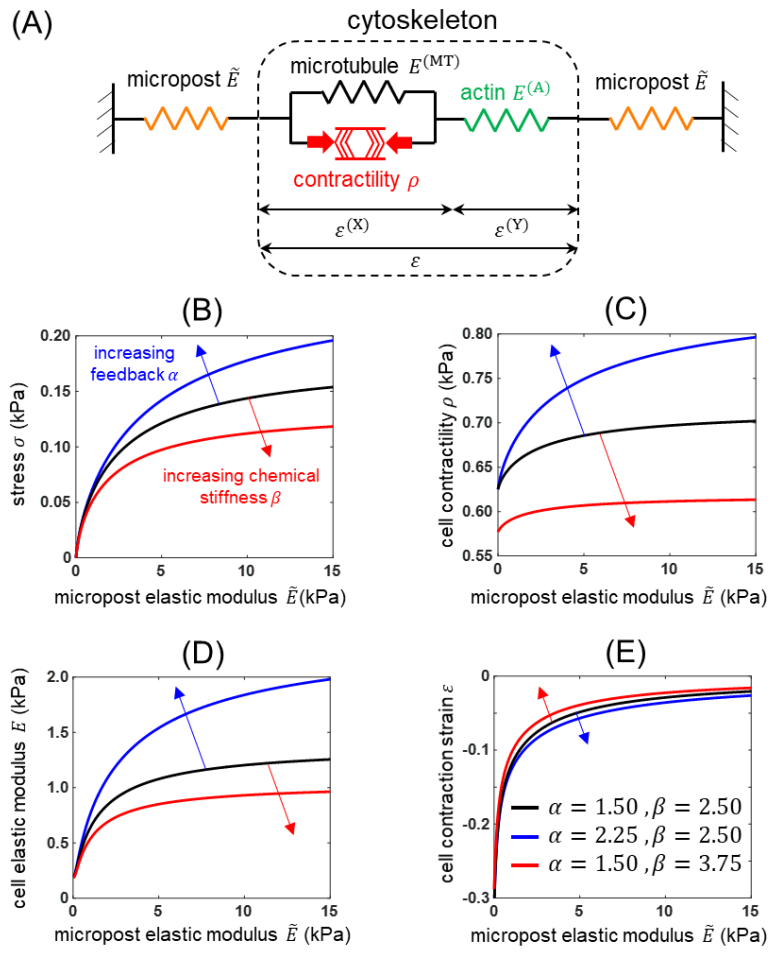

Figure S20. Cell force generation, cell contractility, and cell stiffness increase with micropost stiffness. (A) A one-dimensional model for a cell adherent to microposts. (B) When the cell is connected to the microposts, the cell contractility generates a tensile stress σ which increases with micropost stiffness $\tilde{E}$. (C) The cell responds to this increase in the tensile stress σ by increasing the density of phosphorylated myosin motors which leads to an increase in the cell contractility ρ with $\tilde{E}$. (D) The cell also responds to the stiffening of its surrounding (increase in $\tilde{E}$) by recruitment of actin filaments. In our model, $E^{(A)}$ represents the stiffness of the actin filament network which increases in tension (and not in compression) to capture the tension dependent actin recruitment and its subsequent stiffening of the cytoskeleton (see equation (S1.1)). As the tension in the actin filament network, σ, increases with $\tilde{E}$, the tensile strain $\varepsilon^{(Y)}$ increases which results in an increase in the stiffness of the actin filament network, $E^{(A)}$, and subsequently the cytoskeletal stiffness E according to equation (S1.6) (E) The total contractile strain $|\varepsilon|$ decreases with increasing micropost stiffness. In (B-E), a large value of the chemo-mechanical feedback parameter α results in a greater overall density of phosphorylated myosin motors which in turn increases the contractility ρ, the tensile stress in the actin filament network σ, the cell contractile strain $|\varepsilon|$, and the cytoskeletal stiffness E. Unlike α, a large value of the chemical stiffness β makes motor recruitment more difficult which leads to decreases in ρ, σ, $|\varepsilon|$, and E.

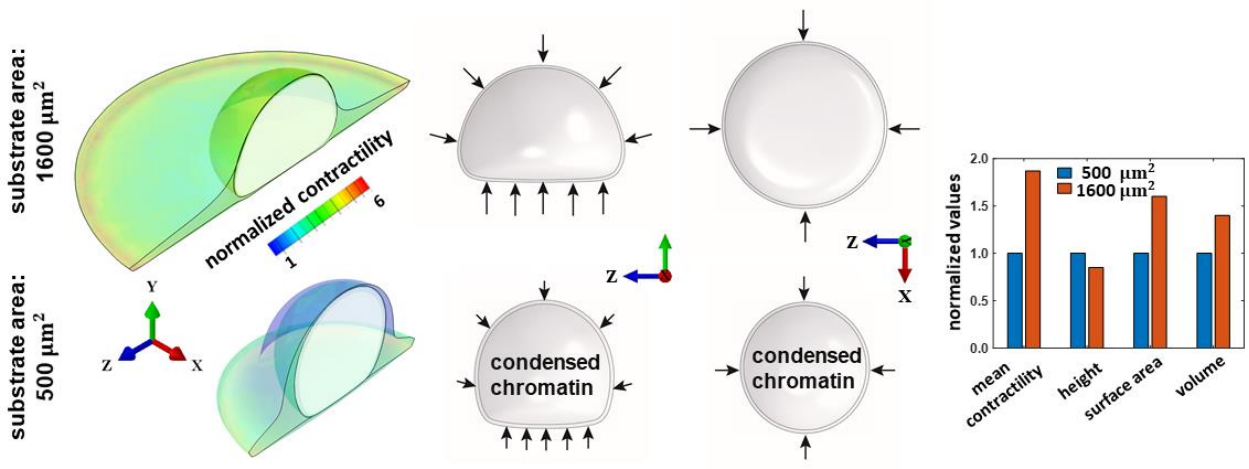

Figure S21. Fibroblasts constrained on small substrates have lower nuclear volume. Fibroblasts with the same initial volume are modelled on circular micropatterned substrates with surface areas of 500 and 1600 μm^2. Our simulations show that cells on the larger substrate area have higher cytoskeletal tension and actomyosin contractility. As a result, higher actomyosin-driven compressive forces are applied to the nucleus and nuclear height decreases. Since our experiments show that cells constrained on smaller substrate areas have decreased nuclear volume and increased chromatin condensation[19], we hypothesize that the reduction of actomyosin contractility in constrained cells causes cytoplasmic-to-nuclear translocation of histone deacetylase 3 (HDAC3) which in turn can lead to lower acetylation level and subsequently chromatin compaction. We then systematically determine HDAC3 level as a function of contractility (as described in SI Section 4.4) and we assume that the chromatin Poisson's ratio $\bar{\nu}$ (regulator of nuclear volume) and the chromatin elastic modulus $\bar{E}$ (regulator of chromatin stiffness) respectively decreases and increases with HDAC3 nuclear level in our model. Our simulations show that the experimentally observed lower nuclear volume of fibroblasts on the smaller area can be explained by considering the fluid content in the nucleus. Concomitant with the lower level of actomyosin contractility, our simulations predict higher nuclear accumulation of HDAC3 in the cell on the smaller area which leads to a decrease in $\bar{\nu}$. Subsequently, nuclear volume decreases which indicates that in the smaller cell higher amount of fluid flows out of the nucleus. Note that the assumption that $\bar{\nu}$ decreases with nuclear accumulation of HDAC3 simply enables us to capture the experimentally observed nuclear volume reduction in fibroblasts constrained on small substrate areas. However, a more complex model based on the pressure difference across the nuclear envelope will be the subject of future work.

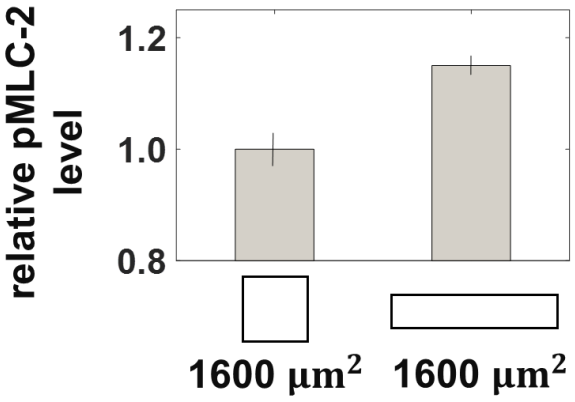

Figure S22. Fibroblasts on rectangular substrate geometries are more contractile than square substrate geometries. Fibroblasts are cultured on fibronectin-coated micropatterned substrates with the same substrate surface area (1600 μm^2) but various aspect ratios (1:1, and 1:5). Rectangular cells exhibit higher levels of phosphorylated myosin light chain.

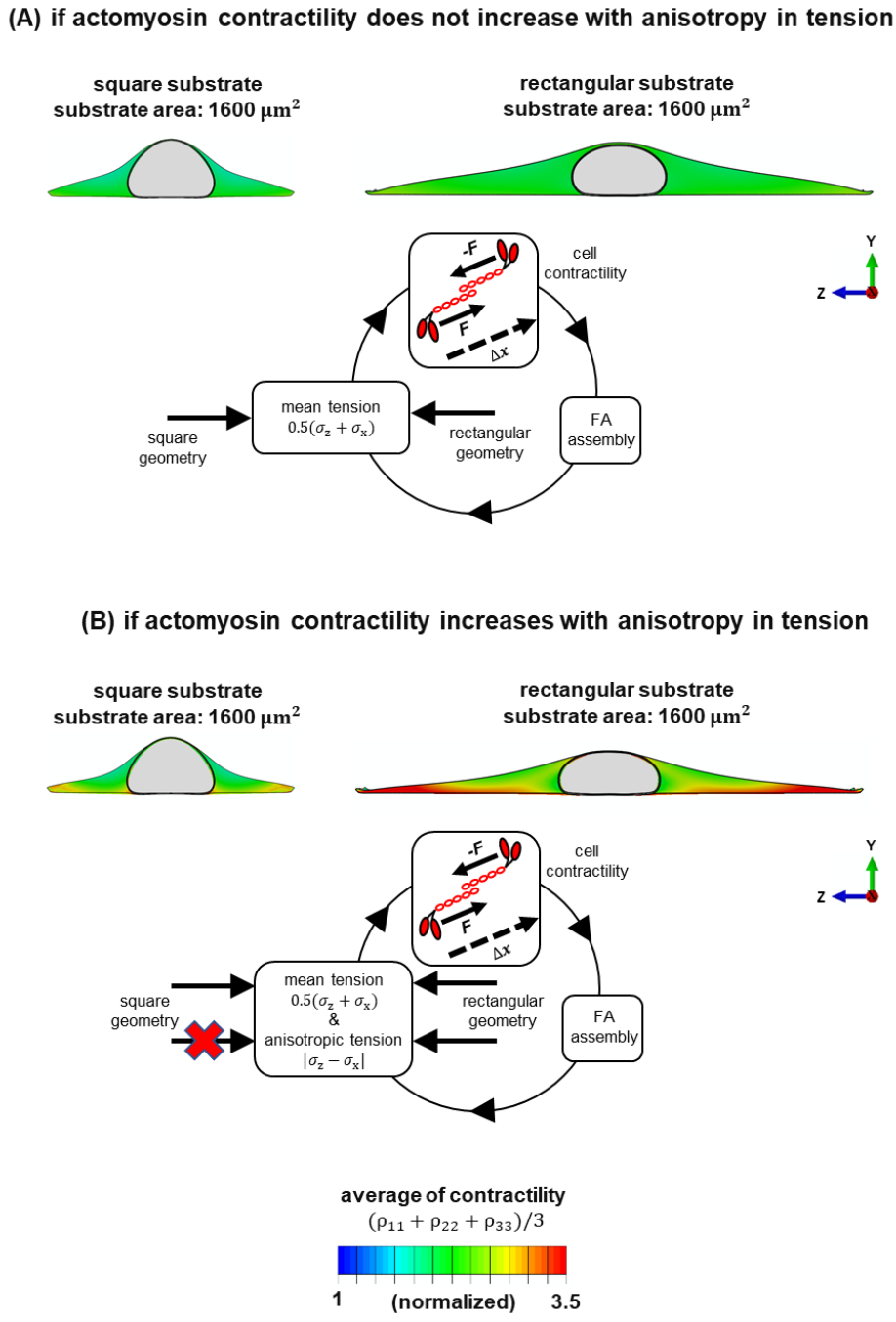

Figure S23. Actomyosin contractility increases with cell elongation. (A) The model only accounts for a positive feedback loop between the average of tension in the cytoskeleton and the average of contractility. The feedback between the average of cytoskeletal tension and the average of contractility enables us to capture the facts that actomyosin contractility increases with substrate area (Fig. 4I) and substrate stiffness (Fig. S19). However, the feedback between the averages of tension and contractility is not enough to capture the experimentally observed changes in actomyosin contractility (Fig. 5B) and nuclear morphology (Figs. 4E and 4F) with substrate aspect

ratio. Our simulations show that although the average level of contractility in the rectangular cell is slightly higher than the square cell, however, this is not enough to capture (i) our experimental observation in Fig. 5B where the level of actomyosin contractility in rectangular cells is more than 20 percent higher, and (ii) the experimentally observed flattened and elongated morphology of the nucleus in Figs. 4E and 4F, respectively. (B) In addition to the feedback loop between the average of tension and the average of contractility, the model also accounts for a feedback loop between the average of contractility and the anisotropy in tension. Therefore, cell contractility increases as the difference between the max. and mid. principal stresses ($\sigma_z - \sigma_x$) increases. Since the rectangular cell experiences an anisotropic cytoskeletal tension ($\sigma_z - \sigma_x$), the average level of contractility in the rectangular cell increases with including the feedback loop between the average of contractility and the anisotropy in tension. Subsequently, the nucleus becomes flattened and elongated as we experimentally observed in Figs. 4E and 4F, respectively.

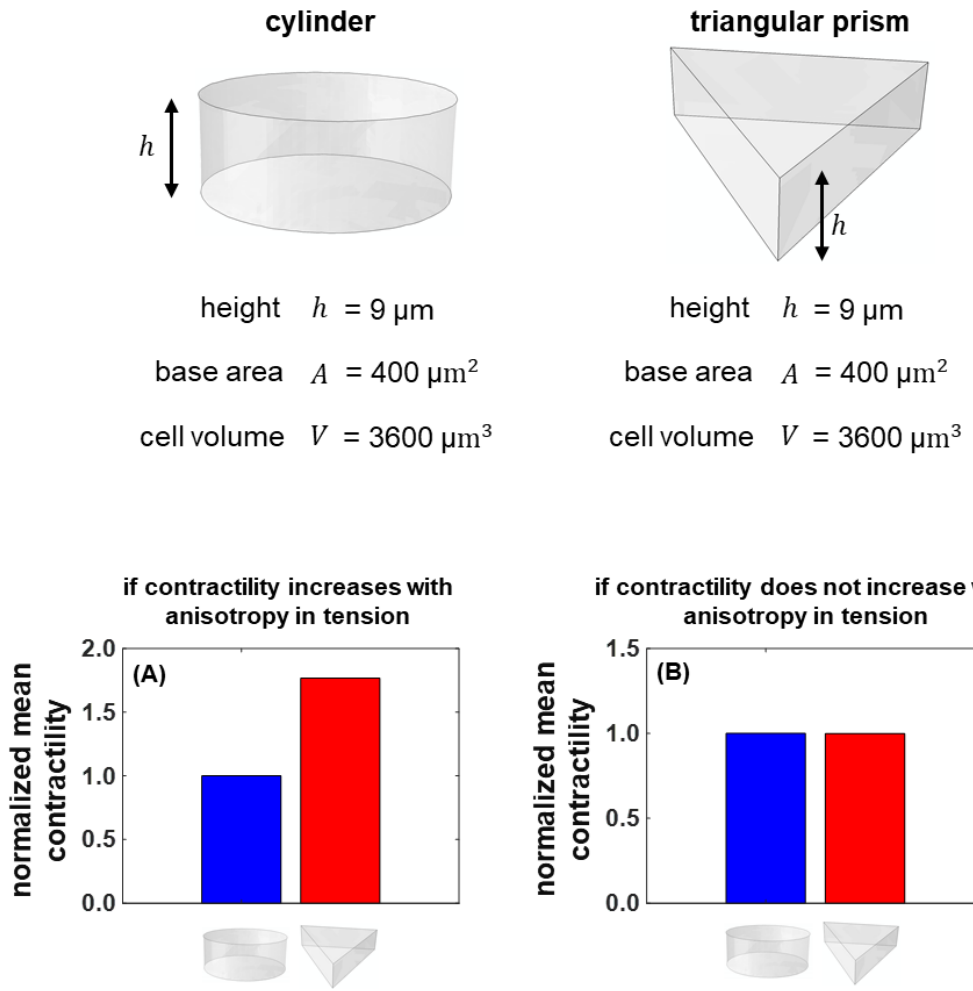

Figure S24. Actomyosin contractility increases with tension anisotropy in 3D microniches. Cells are fully encapsulated within 3D microniches with the same volume, area, and height but different geometries. Our simulations show that cells have significantly higher actomyosin contractility in the triangular prism than in the cylinder (A) which is in agreement with experimental observations in reference[64]. Note that the higher actomyosin contractility in the triangular prism microniches cannot be captured if the mean contractility $\rho_{\mathrm{mean}} = (\rho_{11} + \rho_{22} + \rho_{33})/3$ does not increase with anisotropy in tension.

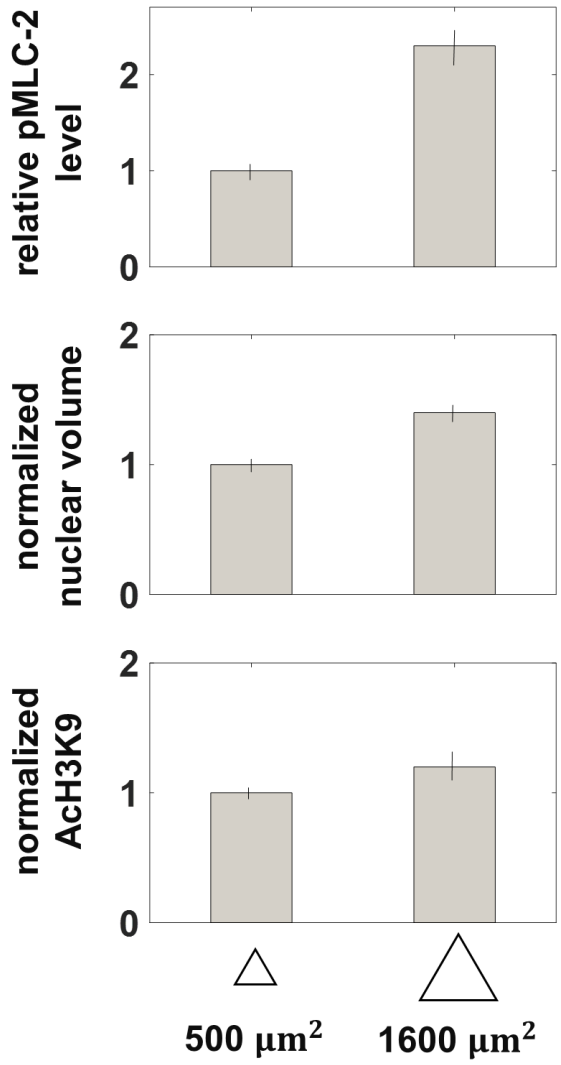

Figure S25. Fibroblasts constrained on small substrates have lower nuclear volume and higher acetylation levels while their nuclei experience lower actomyosin dependent compressive forces. Fibroblasts are cultured on triangular micropatterned substrates with surface areas of 500 and 1600 μm^2. Relative levels of phosphorylated myosin light chain 2, nuclear volume, and relative levels of histone H3 acetylated at lysine 9 decrease when fibroblasts are constrained on small substrate areas.

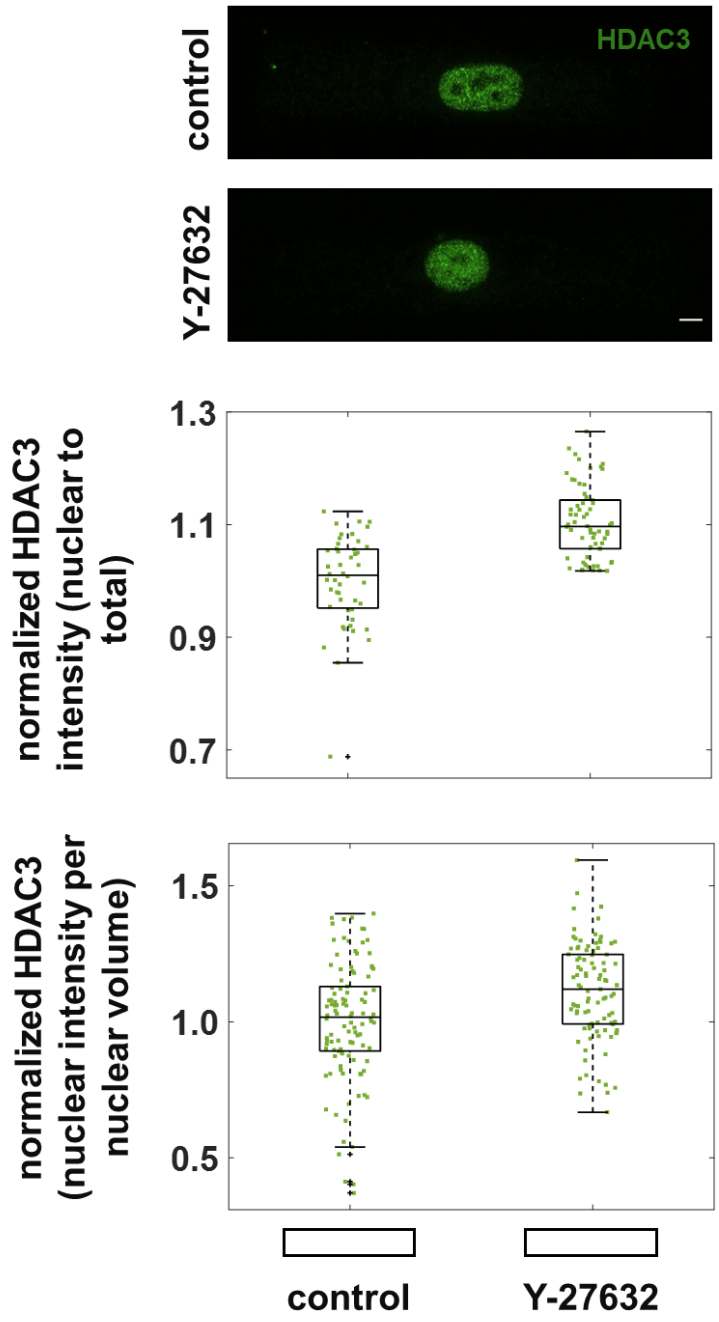

Figure S26. Disruption of actomyosin contractility leads to translocation of HDAC3 from the cytoplasm to the nucleus. Fibroblasts are cultured on rectangular substrates with an aspect ratio of 1:5 and a substrate area of 1600 μm^2. Top: maximum intensity projection of confocal image stacks from the nuclei of control and Y-27632 treated fibroblasts with immunofluorescence staining of HDAC3. Bottom: HDAC intensity based on immunofluorescence staining. Scale bar: 5 μm

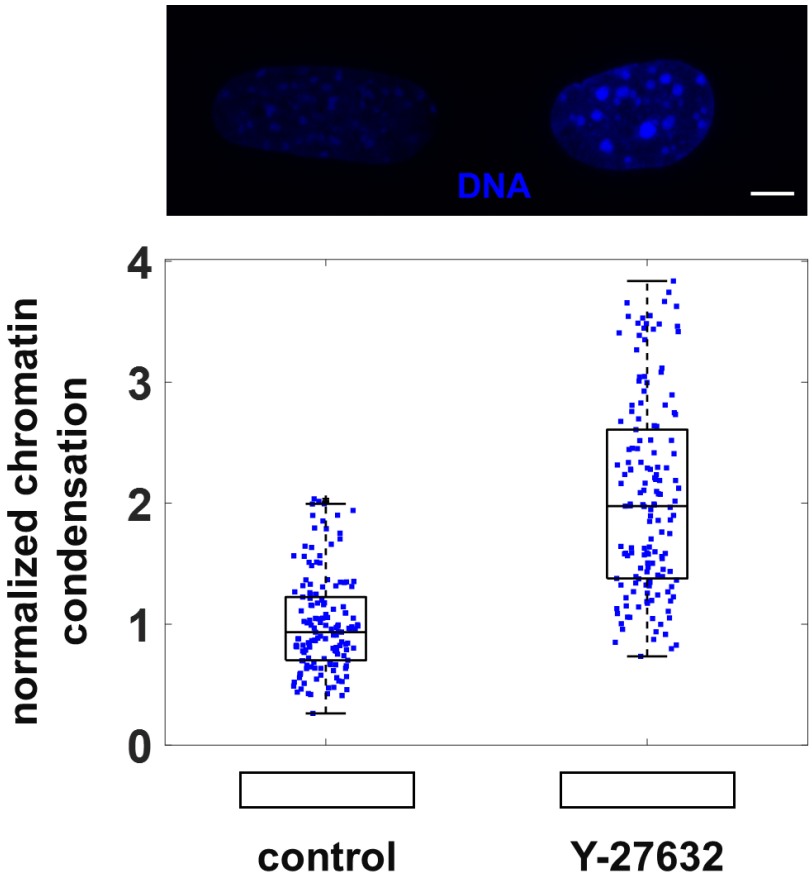

Figure S27. Disruption of actomyosin contractility leads to chromatin condensation. Fibroblasts are cultured on rectangular substrates with an aspect ratio of 1:5 and a substrate area of 1600 μm^2. Top: maximum intensity projection of confocal image stacks from the nuclei of control and Y-27632 treated fibroblasts where DNA is stained with DAPI. Bottom: condensation of chromatin in the nuclei of control and Y-27632 treated fibroblasts based on DAPI staining. Scale bar: 5 μm

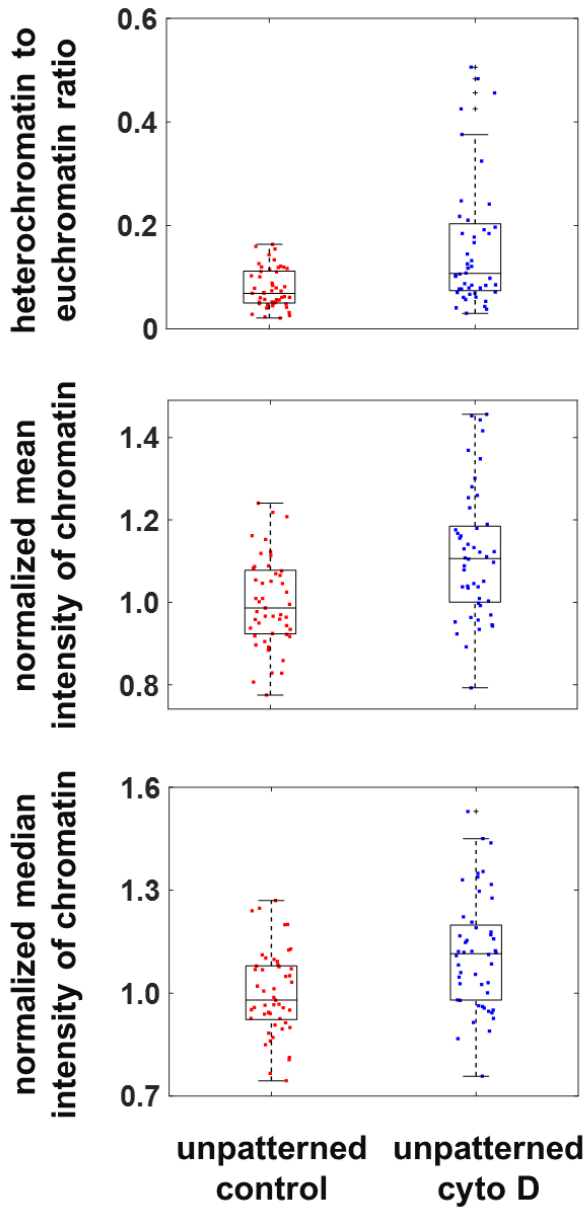

Figure S28. Disruption of actomyosin contractility upon cytochalasin D treatment leads to chromatin condensation in un-patterned fibroblasts. Fibroblasts are cultured on unpatterned substrates. The number of heterochromatin pixels divided by the number of euchromatin pixels (top). Chromatin condensation based on the mean (middle) and median (bottom) intensity projection of confocal images from the nuclei of control and cytochalasin D treated fibroblasts.

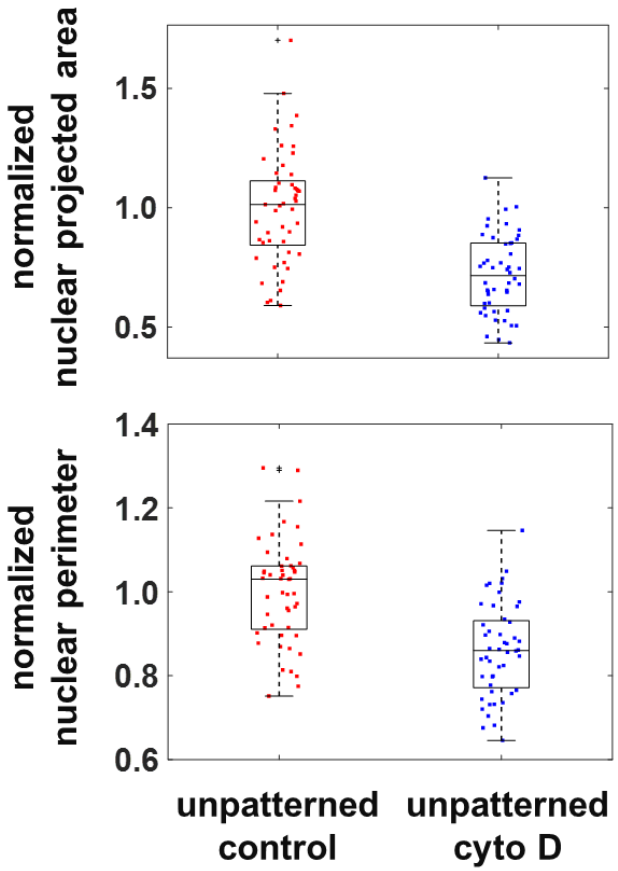

Supplementary Figure 29. Disruption of actomyosin contractility leads to decreases in nuclear projected area and nuclear perimeter in un-patterned fibroblasts. Fibroblasts are cultured on unpatterned substrates. Disruption of actomyosin contractility upon treatment of fibroblasts with cytochalasin D causes reduction of nuclear projected area and nuclear perimeter associated with the condensation of chromatin observed in Figure S27.

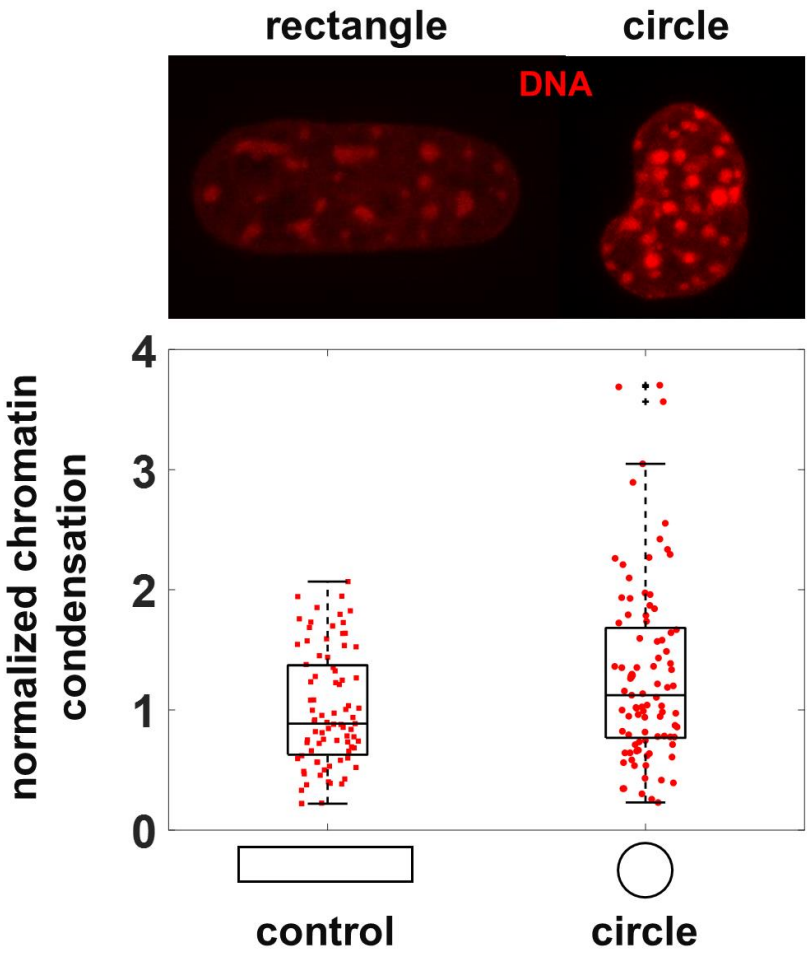

Figure S30. Constraining cells on small and circular substrates leads to chromatin condensation. Fibroblasts are cultured on two extreme geometries of fibronectin-coated micropatterns: (i) a rectangle with an aspect ratio of 1:5 and a substrate surface area of 1600 μm^2 (large and elongated geometry), and (ii) a circle with a substrate surface area of 500 μm^2 (small and symmetric geometry). Top: maximum intensity projection of confocal image stacks from the nuclei of rectangular and circular fibroblasts where DNA is stained with DAPI. Bottom: condensation of chromatin in the nuclei of rectangular and circular fibroblasts based on DAPI staining. Scale bar: 5 μm

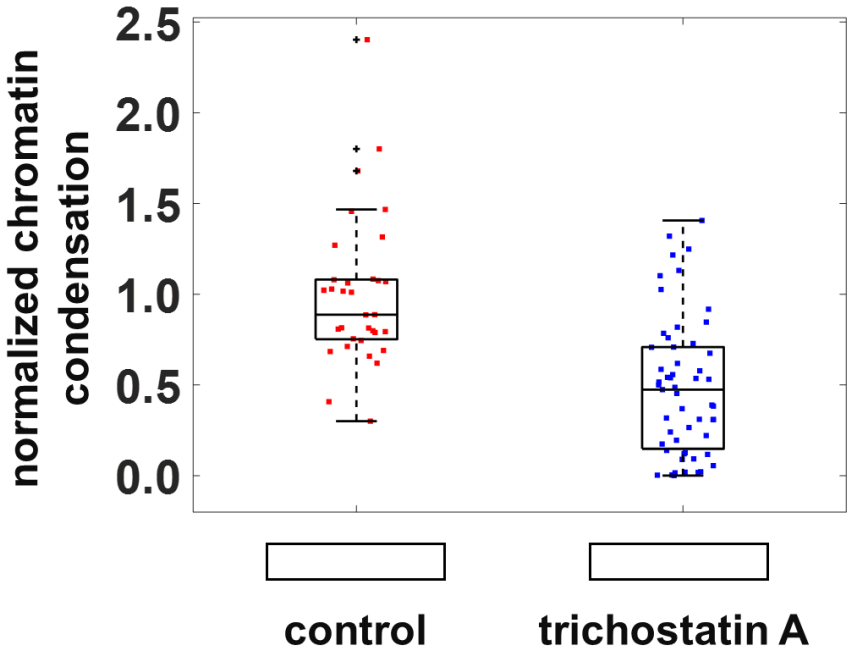

Figure S31. Inhibiting HDACs causes chromatin decondensation. Fibroblasts are cultured on a rectangular substrate with a surface area of 1600 μm^2 and an aspect ratio of 1:5 (large and elongated geometry). Inhibiting HDACs upon trichostatin A (TSA) treatment leads to decondensation of chromatin based on DAPI staining.

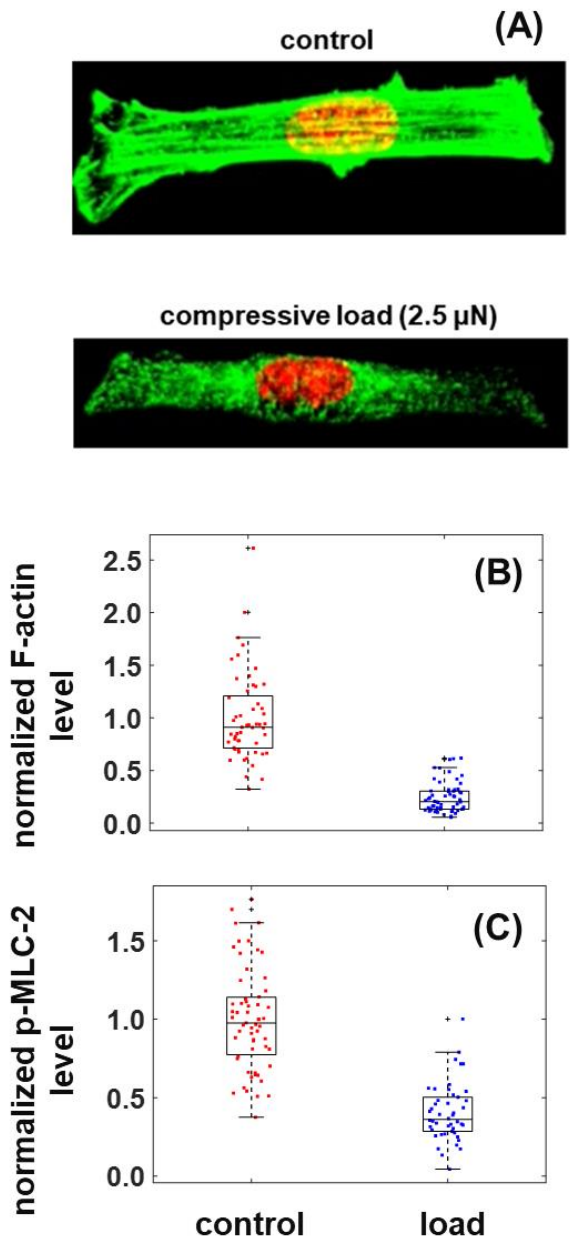

Figure S32. Compressive forces cause disruption of actomyosin contractility. Fibroblasts are cultured on a rectangular substrate with a surface area of 1600 μm^2 and an aspect ratio of 1:5. (A) Depolymerization of apical stress fibers. (B) Relative F-actin intensity levels. (C) Relative levels of phosphorylated myosin light chain 2 at serine 19 based on immunofluorescence staining.

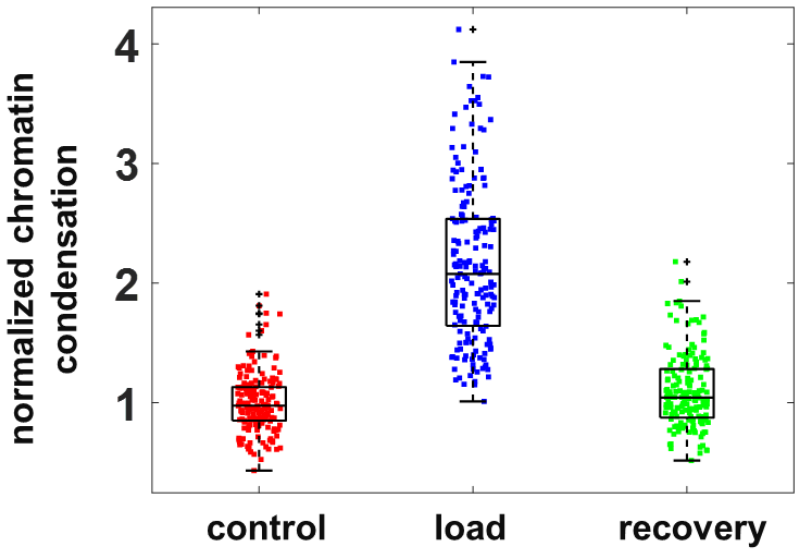

Figure S33. Compressive forces induce reversible chromatin condensation. Fibroblasts are cultured on rectangular substrates with an aspect ratio of 1:5 and a substrate area of 1600 μm^2. DAPI staining of DNA shows that compressive forces cause chromatin condensation in fibroblasts while they revert to their original conditions after removal of the compressive forces.

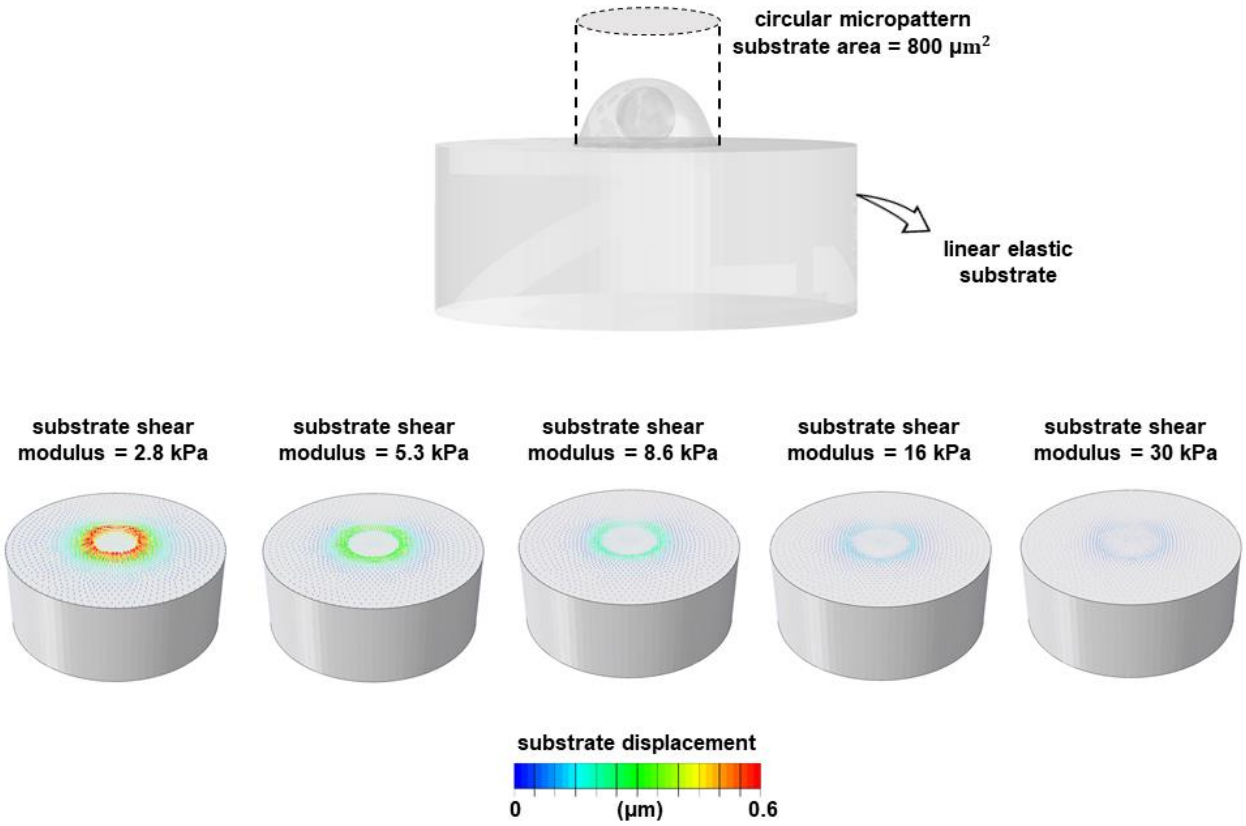

Figure S34. Training the model. Knowing the approximate range of the model parameters from our previous studies[4], we first determine the cytoskeleton parameters. To this end, we first make at least three initial guesses for each cytoskeleton parameter. Combining all initial guesses for cytoskeleton parameters, we make more than 30 parameter sets. Note that all these parameter sets satisfy the stability criterion described in SI Section 6. Using the least squares method described below, the best parameter set is determined such that the resulting displacement fields from the model give the best match to the experimentally measured displacement fields in reference[65]. To this end, for each substrate stiffness, we calculate the residual which is the difference between the experimental and theoretical maximum displacements, and we then calculate the sum of squared residuals (R) for each parameter set. Finally, we pick the set of parameters that gives the minimum R. Using the determined cytoskeleton parameters, we then use our experimental results for fibroblasts on different micropatterned substrates to determine the best set of parameters for the nucleus such that the nuclear geometries (including nuclear height and aspect ratio) from our model for different substrates give the best match to our experiments (similar to the procedure described for the cytoskeleton). The list of available micropatterned substrates from our experiments for training the model can be found in reference[19]. We finally ensure that the model predictions with the determined cytoskeleton and nucleus parameters are in good agreement with the experimental results for NIH 3T3 fibroblasts on different substrate geometries in reference[65]. After training the model, we then test the model predictions new experiments shown in the main text.

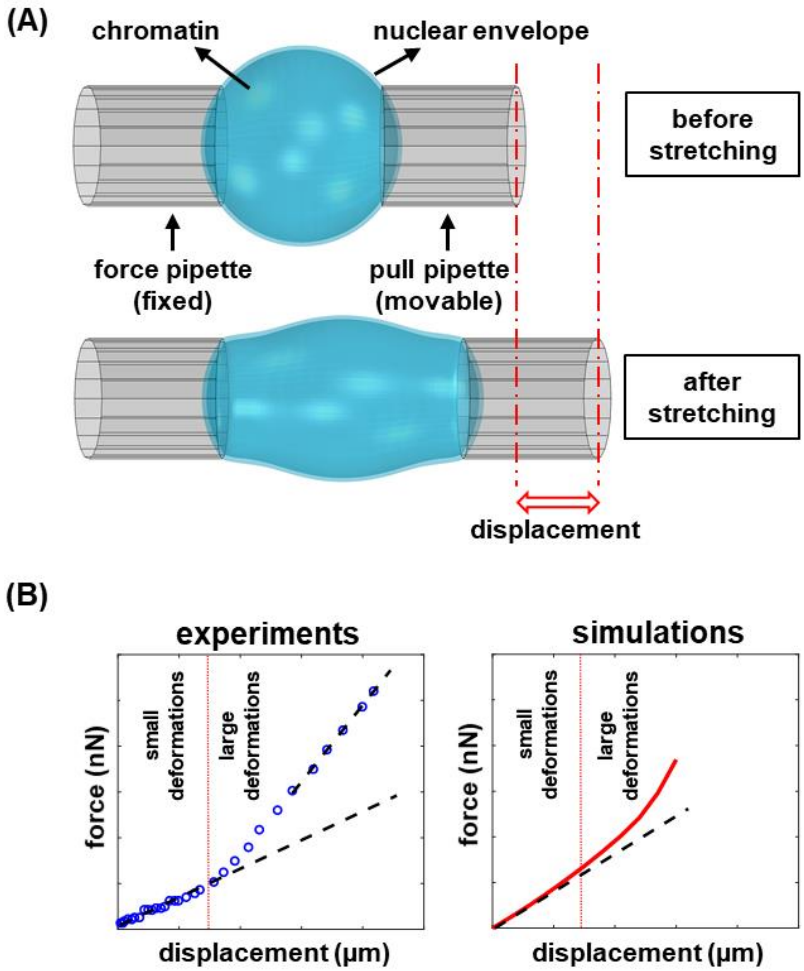

Figure S35. Uniaxial stretching of an isolated nucleus. The nucleus is modeled as an elastic thin layer filled with a solid material. The elastic thin layer represents the nuclear envelope lamina network and is treated as a fibrous material which is soft and isotropic at small strains while it stiffens at large tensile strains. The solid material represents chromatin and is modeled as a linear elastic material. The nucleus is fixed at the left end and is uniaxially stretched at the right end. For small extensions, the nucleus shows a linear force-displacement response as chromatin governs nuclear response to small extensions. For large extensions, the nucleus exhibits a strain stiffening response which is dominated by the nuclear envelope[6].

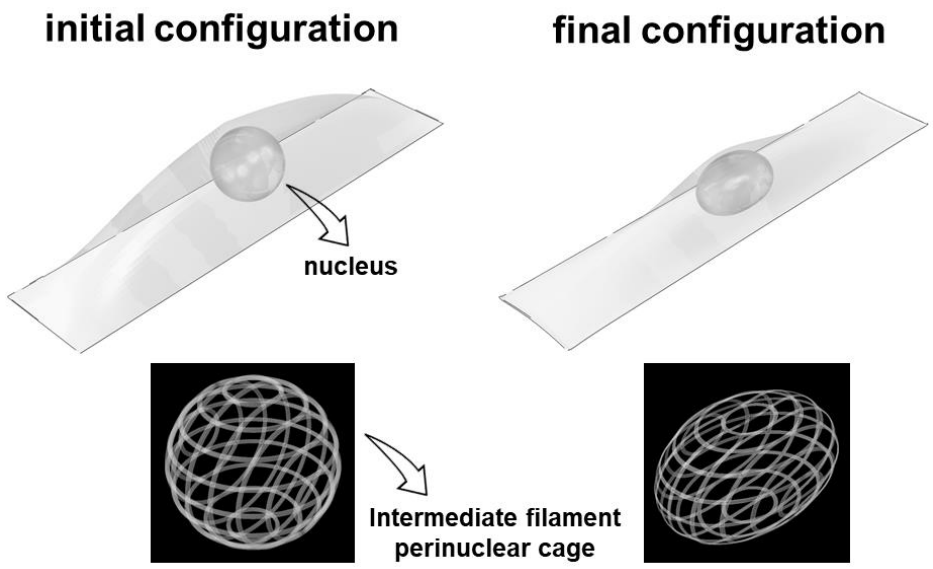

Figure S36. Intermediate filaments form a juxtanuclear cage. In our simulations, intermediate filaments are modeled as a deformable cage-like network around the nucleus.

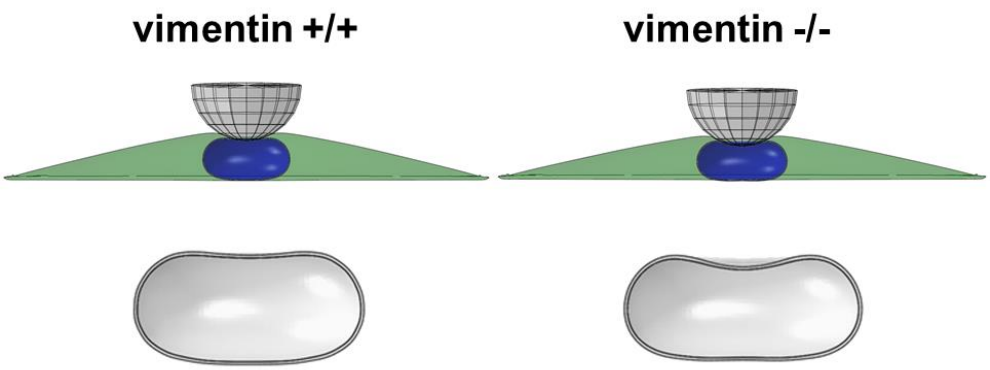

Figure S37. Intermediate filaments contribute to cytoskeletal stiffness and protect the nucleus against external forces. Simulation results for wild type (vimentin +/+) and vimentin-null (vimentin -/-) cells. Vimentin intermediate filaments form a perinuclear cage which contributes to cytoskeletal stiffness and protects the nucleus from excessive deformations under external forces.

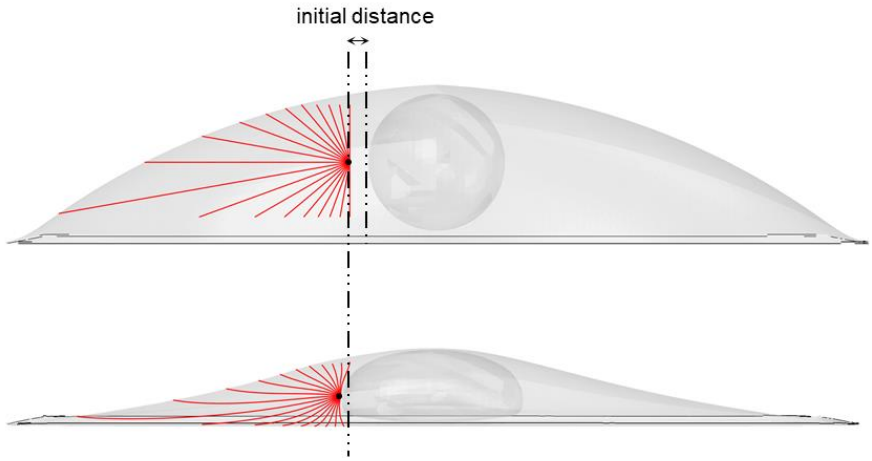

Figure S38. The MTOC cannot indent the nucleus in the rectangular substrate geometry. The MTOC is pushed toward the cell boundary by the nucleus in the rectangular substrate geometry.

Supplementary Table 1. Cell model parameters used in Figure S20

$\boldsymbol{\rho_0}$	initial contractility	0.5 kPa
$\boldsymbol{E^{(MT)}}$	microtubule elastic modulus	2.0 kPa
$\boldsymbol{E^{(I)}}$	actin network initial elastic modulus	0.2 kPa
$\boldsymbol{\ell}$	actin stiffening parameter	100 kPa
$\boldsymbol{m}$	actin stiffening parameter	3

Supplementary Table 2. Cell model parameters used in Figure S17

$\boldsymbol{\rho_0}$	initial contractility	1.0 kPa
$\boldsymbol{\alpha}$	chemo-mechanical feedback parameter	1.5 kPa^{-1}
$\boldsymbol{\beta}$	chemical stiffness parameter	2.5 kPa^{-1}
$\boldsymbol{E^{(MT)}}$	microtubule elastic modulus	2.0 kPa
$\boldsymbol{E^{(I)}}$	actin network initial elastic modulus	0.2 kPa
$\boldsymbol{\ell}$	actin stiffening parameter	100 kPa
$\boldsymbol{m}$	actin stiffening parameter	3
$\boldsymbol{\bar{E}}$	chromatin elastic modulus	0.15 kPa
$\boldsymbol{\hat{E}^{(I)}}$	lamin initial elastic modulus	0.05 kPa
$\boldsymbol{\hat{\ell}}$	lamin stiffening parameter	5 kPa
$\boldsymbol{\hat{m}}$	lamin stiffening parameter	2

Captions for movies

Movie 1: Cytoskeletal tension and nuclear morphology in fibroblasts cultured on a fibronectin coated rectangle with an aspect ratio of 1:5 and a substrate surface area of 1600 μm^2 (large and elongated substrate geometry).

Movie 2: Cytoskeletal tension and nuclear morphology in fibroblasts cultured on a fibronectin coated circle with a substrate surface area of 500 μm^2 (small and circular substrate geometry).

Movie 3: Microtubules in large and elongated cells buckle without being able to significantly indent the nucleus as the MTOC is pushed toward the cell boundary by the nucleus.

Movie 4: Cells on small and circular substrates exhibit crescent-shaped nuclear morphologies as the MTOC pushes against the nucleus and forms a local indentation in the nucleus.